Insightful Investigations:
Exploring Material Properties through Characterization Techniques

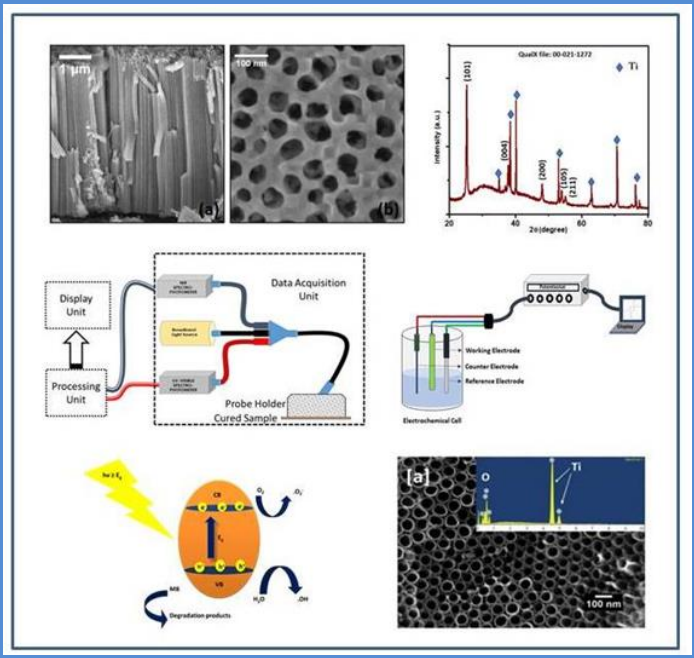

Department of Physics
Union Christian College, Aluva-2

Insightful Investigations: Exploring Material Properties through Characterization Techniques

Editors:
Dr Shinoj V K
Department of Physics, Union Christian College Aluva 683102.
Dr Saritha K Nair
Department of Physics, Mar Athanasius College (Autonomous), Kothamangalam 686666.

Publishers:
Union Christian College Aluva 683102

ISBN: 978-81-960457-1-5

Cover Design: Dr Shinoj V K

Printing: SN Press, Aluva.

Price: Rs 200/-

Proceedings of

WMCT

National Workshop on Material Characterization Techniques

March 22-23, 2023

Union Christian College, Aluva-2

under
Scientific Social Responsibility (SSR)
activity head of DST-SERB Project

Editors

Shinoj V K
Department of Physics, Union Christian College, Aluva - 2

Saritha K Nair
Department of Physics, Mar Athanasius College (Autonomous)
Kothamangalam

Forword

A national Workshop on Materials characterization Techniques (WMCT) was conducted by the Department of Physics, Union Christian College, Aluva under the SSR policy of Department of Science and Technology, Government of India on 22nd and 23rd March 2023 with the college as the venue. The workshop was aimed at giving an in depth understanding of various experimental tools and analysis procedures used in characterizing materials at nano and micro scales, to faculty of various colleges, research scholars in the field and post graduate students. The main speaker was Prof. Reji Philip, RRI, Bangalore who handled sessions on Linear optical characterization techniques for materials. There were Plenary sessions on UV-Vis spectrophotometry-Instrumentation and data analysis, X-ray diffraction - Instrumentation and data analysis and Photothermal lens. A poster presentation session by various faculty and research scholars was also conducted. The proceedings of the selected papers from the presentations are hereby being released.

The papers encompass topics related to preparation of materials at quantum dot, nano, micro and bulk dimensional levels using various fabrication techniques comprising green synthesis, chemical methods, electrochemical anodization, solvothermal and hydrothermal methods. Their analyses employing structural, morphological, spectroscopic, voltammetric and optoelectronic characterizations as well as utilizing theoretical approaches like DFT computation and Rietveld refinements also form part of the discussion. Moreover, detailed information on the successful employment of these materials in Catalysis, Antimicrobial measures, Dye sensitized solar cells, supercapacitors, LEDs and photoluminescent applications are included. Brief discussions on spectroscopic techniques for testing food material adulteration and synthesis of dye-based phantom- tissue samples are also covered.

The organizing committee and the convenors of the workshop wish to place on record their thanks to all the participants, the plenary speakers, the research scholars and PG students, who worked proactively to make WMCT a grand success. Finally, a big thanks to DST for supporting the workshop through its financial Policy.

Prof. Rachel Reena Philip
Convenor, WMCT-23

Table of Contents

Performance of solar cells in correlation to dye loading and adsorption capability

Gisa Grace Ninan[1*], Manoj Balachandran[1]
[1]*CHRIST (deemed to be University), Bangaluru – 560029*
* *gisa.grace@christuniversity.in*

Abstract. Present study reports the fabrication of a natural dye-sensitized solar cell (NDSSC) using dyes prepared from *Hibiscus rosasinensis* (Hibiscus flower petals) and *Allium cepa* (onion peel). The optimization of "photo anode dipping time" and the effect of "mixing of these dyes" are investigated and presented. The best dipping time and dye combination is decided from the output parameters obtained for the device. For better comparison other components of solar cell namely Photo-anode (Titanium dioxide (TiO_2)), Electrolyte (Iodolyte HI-30) and Counter electrode (Platisol T/sp) are kept the same.

Keywords: NDSSC, Natural dyes, Photo anode.

1 Introduction

Recent studies have shown that the depletion of fossil fuels are in fast rate so that it is time for us to look into renewable energy sources. There are many renewable energy sources such as wind mills, tidal sources, geothermal, solar energy etc. Out of these, solar energy is widely harvested all over the world as it is available free of cost and in abundance. The solar energy is harvested and is converted into electricity using solar cells. The solar cells are made from different materials and mainly fall into four generations. The DSSC and other organic high efficiency solar cells come under the third-generation category. Among organic, DSSCs attain a large emphasis due to its easy fabrication technique, better efficiency, low cost and flexibility of coating over any surface [1]. The highlight of DSSC's is that, here the device working is mainly based on sensitized wide band gap semiconductors like TiO_2. Thus, the device performance basically depends on the absorption range of the sensitizers used and its ability to anchor on to TiO_2 surface. Even though there are many synthetic dyes made out of transition metals, natural dyes are more preferred from the point of environmental aspects. The main components of a DSSC are photo anode, sensitizers, electrolyte and counter electrode [2]. In the present

study we mainly focus on the sensitizer part which includes the optimization of dipping time and effect of mixing of dyes. The dyes used for these studies are prepared from Hibiscus and Onion peel [3, 4]. This is important as the output current we collect depends on the amount of dye absorbed. The more dye absorbed converts more light to carriers which in turn increases the efficiency of the device [4].

2 Materials and Methods

The Hibiscus and Onion Dye is prepared as shown in Figure 1. The extracted dye is stored at low temperature. The photo anode is prepared on ITO and is dipped in sensitizers synthesized from both hibiscus and onion peel separately and in combination. The dipping time is increased from 15 hours to 24 hours and 48 hours. The samples are named according to dipping time as H15, H24, H48, O15,O24 and O48 respectively for hibiscus and onion. Since we mainly focus on device performance, the dipping time is optimized based on the highest device efficiency obtained.

Fig. 1. The preparation of both dyes from their respective sources.

The mixing of dyes are done in terms of concentration taken from each dye.The ratio of mixing is varied as Hibiscus (ml):Onion(ml), in the ratios 1:1, 1:4 and 4:1. The sample names are M(1:1), M(1:4) and M(4:1) respectively. The present study highlights an overall idea about the adsorption capability and effective dye loading time for natural dyes.

3 Results and Discussions

The NDSSCs are prepared by varying the dye dipping time and dye concentration as mentioned before. The counter electrode is fabricated using Platinum and Iodine is taken as the electrolyte. The electrolyte is added between the photo anode and counter electrode and is clipped from both sides using binder clips. A comparative study is done and the J-V characteristics of the solar device are obtained from solar simulator under standard conditions (Figure 2). Even though various studies are reported on natural dyes, the variation in device performance with dipping time for each natural dye has not been checked. Most of the literature reports suggest 24 hours as the standard dipping time and that has been done for synthetic dye where more dipping time is not found to be very effective. But our study shows that in the case of natural dyes it is different and that dipping time indeed has a direct correlation with efficiency of the DSSC. Moreover, though mixing of various dyes has been tried to see its effect on efficiency, no reports are seen till date on the combination of dyes prepared from Hibiscus and Onion peels.

Here, the cell parameters are determined for devices fabricated separately with hibiscus and Onion peel dyes and also after mixing the dyes. The output parameters like open circuit voltage Voc and short circuit current Jsc obtained from the devices are tabulated in Table 1,2 and 3 along with the calculated fill factor FF and the cell efficiency. It is observed that there is a slight increase in Voc as well as efficiency with the increase in dipping time.

Table 1. The output parameters obtained on varying the dipping time for Onion dye

Name Of sample	Voc (V)	JSC mA/cm^2	FF %	Efficiency %
O15	0.54	5.71	54.51	1.67
O24	0.62	6.33	47.40	1.87
O48	0.62	6.20	55.12	2.10

Table 2. The output parameters obtained on varying the dipping time for Hibiscus dye

Name Of sample	Voc (V)	JSC mA/cm^2	FF %	Efficiency %
H15	0.48	6.19	59.01	1.76
H24	0.55	6.39	56.60	1.98
H48	0.58	6.45	52.50	2.10

The overall efficiency is maximum for 48 hours and then remains almost constant with further increase in dipping time. So, considering the time of dipping for better efficiency, 48 hours is considered to be the best. The corresponding cell efficiency is slightly better than the maximum efficiency of 2% so far reported in literature using the Onion peel and Hibiscus dye as sensitizers [5,6,7].

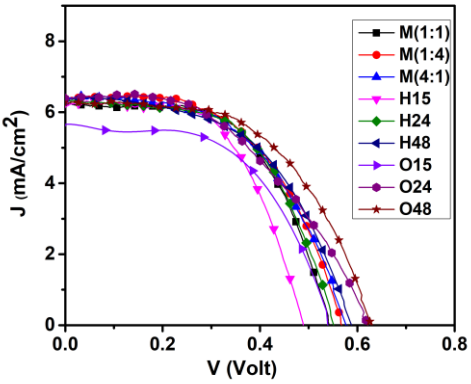

Fig. 2. The J-V characteristics obtained for all the devices prepared.

From the absorption graph (Fig. 3) the absorption range of Hibiscus dye is from 250 nm to 400 nm and that of Onion peel dye is from 400 nm to 800 nm. So as a trial, mixing of these dyes is done to utilize the complete absorption range.

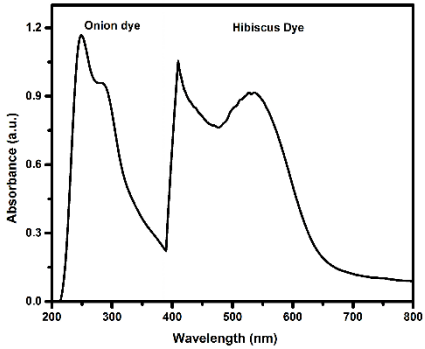

Fig. 3. The combined absorption graph of Onion and Hibiscus Dye

The output parameters obtained by mixing of dye is given in Table 3. But mixing is not found to be yielding a better efficiency, suggesting that it is not the best method for improving the device efficiency.

Table 3. The output parameters obtained after mixing Onion and Hibiscus dye at various ratios

Name Of sample	Voc (v)	JSC ma/cm^2	FF %	Efficiency%
M(1:1)	0.53	6.27	58.11	1.95
M(1:4)	0.56	6.43	54.10	1.90
M(4:1)	0.57	6.37	53.60	1.94

4 Conclusion

The photo anode is prepared and dipped in sensitizers synthesized from both Hibiscus and Onion peel. The dipping times are set as 15 hours, 24 hours and 48 hours. A comparative study is done and the J-V characteristics of the solar device fabricated are obtained from solar simulator. The present study highlights an overall idea about the adsorption capability and effective dye loading time for natural dyes. The results obtained validates 48 hours as the best dipping time and the enhanced efficiency is ~ 2.1%. We couldn't find any

notable improvement with the mixing of dyes. The efficiency remained constant irrespective of mixing concentration.

Acknowledgments

Authors would like to acknowledge CHRIST (deemed to be university) for providing all the facilities. We also acknowledge Dr. M.J Elizabeth retired Prof Catholicate college, Pathanamthitta for providing us the source material in bulk quantity.

References

1. Narasimman, Kalaiselvan, et al.: "Performance analyses of dye-sensitized solar cell with various type of electrodes and natural dyes using FTO glass." AIP Conference proceedings, 2520 (2022).
2. Bera, S., et al. :"Research into dye-sensitized solar cells: a review highlighting progress in India." Journal of Physics: Energy, 3.3, 032013 (2021).
3. Willoughby, A. A., et al. : "Fabrication and Characterization of a Dye-Sensitized Solar Cell using Natural Dye Extract of Rosella (Hibiscus sabdariffa L.) as Photosensitizer." Journal of the Nigerian Society of Physical Sciences, 287-291 (2021).
4. Inbarajan, K., S. Sowmya, and B. Janarthanan: "Direct and soxhlet extraction of dyes from the peels of Allium cepa and its effective application in dye–Sensitized solar cells as sensitizer." Optical Materials 129, 112487 (2022).
5. Rajab, Fahd M: "Effect of solvent, dye-loading time, and dye choice on the performance of dye-sensitized solar cells." Journal of Nanomaterials, 15-15 (2016).
6. Mansa, Rachel Fran: "Hibiscus flower extract as a natural dye sensitiser for a dye-sensitised solar cell." *Journal of Physical Science* 25.2, 85 (2014).
7. Inbarajan, K. S. Sowmya, and B. Janarthanan: "Direct and soxhlet extraction of dyes from the peels of Allium cepa and its effective application in dye-Sensitized solar cells as sensitizer." *Optical Materials* 129, 112487 (2022).

Differential Scanning Calorimetry as a Technique for Detecting Adulteration of Natural Honey

Saritha K Nair[1*]

[1]*Mar Athanasius College (Autonomous) Kothamangalam, Kerala-686666*
**saritha_physics@macollege.in*

Abstract. Honey adulteration has appeared in the world market from way back. Since sugar syrups are readily available, they are used extensively in honey adulteration resulting in lower quality commercial products. In this work, an effort is made to understand the feasibility of the Differential Scanning Calorimetry (DSC) technique as a tool for honey adulteration detection. A study is made to obtain an observable, gradual change in any of the DSC parameters with the addition of sugar syrup to honey so as to make use of the change in that parameter as a measure of the adulteration.

Keywords: Food adulteration detection, Thermal analysis, Differential Scanning Calorimetry, Food quality, Honey adulteration detection.

1 Introduction

The food adulteration is a common practice nowadays. Food adulteration refers to the act of introducing external chemical substances into a food item that are similar in nature to naturally occurring substances in the food item. In nearly all instances, the adulterant possesses a chemical composition that closely resembles that of the food item in which it is incorporated.

Honey is an important food product that is getting adulterated. The primary chemical constituents of honey, accounting for approximately 95% of its composition, are sugars and water. The minor components of honey include proteins, flavors, aromas, pigments, and a variety of volatile compounds. The substances most often incorporated into honey are sugar syrups as they are readily available. The added syrups lower the quality of the honey. Since the sugars have the same chemical composition, as the sugars in honey, there may not be many changes in the chemical parameters of pure honey and honey adulterated with sugar syrup. Since the chemical parameters are almost the same, we are using thermal analysis. In thermal analysis, the most widely used

technique is DSC - Differential Scanning Calorimetry (DSC). This technique is used to study the thermal transitions of a substance [1-5].

The use of DSC gives us the following advantages: the measurements are made very rapidly and the amount of sample required is very little. The baseline deviation of the thermoanalytical DSC curve arising from the change in heat capacity characterizes the glass transition temperature (T_g) of the substance. When the substance is cooled below this specific temperature, it acquires a rigid and fragile characteristic similar to glass, while it is elastic when heated above that temperature. The glass transition happens to amorphous substances only. It is important to emphasize that although certain substances consist of both crystalline and amorphous components, only the amorphous portion undergoes a glass transition, while the crystalline portion solely experiences melting.

We used the DSC technique to detect the effect of adulteration on the thermal behaviour of locally available honey. If there is any observable, gradual changes in any of the DSC parameters with the addition of sugar syrup to honey, it is a good indication of the possibility of using this method to find out whether the honey is pure or is adulterated with cane sugar syrup.

2 Methodology

2.1 Sample preparation

A locally available honey of Agmark Grade A is used for the experiments. Syrup samples were prepared using locally available cane sugar. The sugar was dissolved in water till saturation and then heated without boiling to get clear syrup without precipitation of any sugar crystals. The small impurities were filtered out. The samples other than pure honey and sugar syrup are prepared in volume percentages. In addition to pure honey and pure sugar syrup, samples with 10, 20, 40 and 60 percentages of sugar syrup in honey by volume were used in the experiment.

2.2 Thermal analysis of samples

The thermal analyses of the samples were carried out using the Differential Scanning Calorimeter instrument by TA Instruments. The sample was sealed

in an aluminium crucible. An empty crucible was measured as reference at the same time with the sample crucible. We employed calorimetric heat flow to gather data regarding the overall heat changes generated by carbohydrates when subjected to heating. Runs were conducted from -70ºC to 200ºC for honey and from the data obtained from that sample, the maximum temperature was limited to 100ºC for the other samples. The melting behavior is not noted here due to concerns about the sample spilling out of the crucible and potentially disrupting the reference pan. Additionally, the higher temperatures present practical challenges as they can result in the heat flux sensor being contaminated by caramel from the sugars found in honey. For the samples other than pure honey, runs were conducted from -120ºC to 80-90ºC to obtain required thermal behaviour of the samples. This temperature range was selected to avoid burning of sugars and to prevent the samples from coming out of the crucible.

A heating rate of 10ºC/minute was chosen. This particular heating rate enhances the calorimetric response (without compromising accuracy) and reduces the analysis time, thereby reducing the risk of sample degradation. The cooling rate selected was 3ºC/minute. The DSC runs were carried out to determine the calorimetric heat flow and subsequently the glass transition temperatures of different samples. This glass transition temperature is characterized by a baseline deviation in the DSC curve.

In our process of detecting honey adulteration using DSC, we follow a two-step approach. Initially, we utilize DSC to determine the thermal behavior, specifically the glass transition temperature, of pure honey and pure sugar syrup. Subsequently, we employ DSC to identify any alterations in the thermoanalytical DSC curve, thereby detecting changes in the glass transition temperature values resulting from the addition of syrup to the honey, indicating adulteration.

3 Results and Discussions

The percentage of sugar syrup in the samples is indicated on the legend in the heat flow graph, see Figure 1. The midpoint of baseline deviation of the DSC curve gives the glass transition temperature T_g of that sample. A graph is plotted with percentage of added sugar syrup along the x-axis and the glass transition temperature along the y-axis.

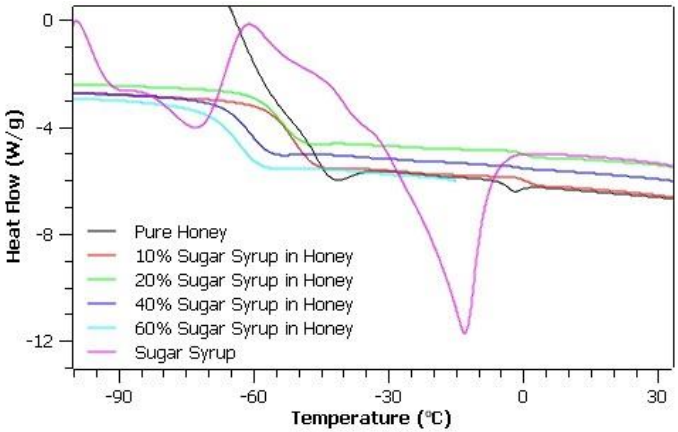

Fig. 1. DSC heat flow curves obtained for samples of pure honey and honey adulterated with sugar syrup.

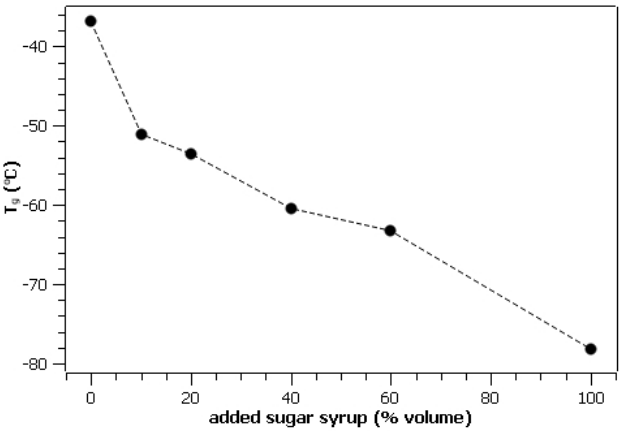

Fig. 2. The glass transition temperature of the samples versus added sugar syrup percentage in each sample.

Although honey is not a purely homogenous material, it has glass transition temperature in the range -44 to -36ºC as per the literature [4]. This may change according to which variety of honey we are using. The glass transition temperature observed for honey in this experiment was -36.81ºC and that for sugar syrup was -78.17ºC.

It is observed that the experiment adulterations made with sugar syrup resulted in a significant decrease in glass transition temperature of the mixture, see Figure 2. This observation indicated the potential of utilizing the glass transition temperature derived from DSC measurements as a means to differentiate between pure honey and honey that has been adulterated with sugar syrup. The presence of a temperature difference in this context could be attributed to the introduction of water from the added syrup into the honey, which acts as a plasticizer on the T_g, as supported by existing literature [3-4].

4 Conclusion

The glass transition temperature, which is highly influenced by the amorphous phases of the sample, will be responsive to changes in the chemical composition and structure resulting from the inclusion of external substances. Accordingly, adulteration of the honey using sugar syrup should result in significant changes in glass transition temperature values. It is experimentally observed that there is a significant decrease in the glass transition temperature with increase in percentage of sugar syrup. This observation shows the possibility of using glass transition temperature obtained from DSC measurements to distinguish between pure honey and honey adulterated with sugar syrup. Glass transition temperature obtained from differential scanning calorimetry measurements is hence a useful parameter for characterizing honeys and for detecting adulteration of honey with sugar syrup. This technique is hence useful in detecting adulteration in commercial samples of honey for very low adulteration percentages.

Acknowledgments

The author would like to acknowledge the support from Indian Institute of Science, Bengaluru under Young Science Fellowship Programme.

References

1. Dranca, F., Ropciuc, S., Pauliuc, D., Oroian, M.: Honey adulteration detection based on composition and differential scanning calorimetry (DSC) parameters. LWT - Food Science and Technology 168, 113910 (2022).
2. Tomczyk, M., Czerniecka-Kubicka, A., Miłek, M., Sidor, E., Dżugan, M.: Tracking of Thermal, Physicochemical, and Biological Parameters of a Long-Term Stored Honey Artificially Adulterated with Sugar Syrups. Molecules 28, 1736 (2023).
3. Cordella, C., Faucon, JP., Cabrol-Bass, D., Sbirrazzuoli, N.: Application of DSC as a tool for honey floral species characterization and adulteration detection. Journal of Thermal Analysis and Calorimetry 71, 279-290 (2003).
4. Cordella, C., Antinelli, JF., Aurieres, C., Faucon, JP., Cabrol-Bass, D., Sbirrazzuoli, N.: Use of Differential Scanning Calorimetry (DSC) as a New Technique for Detection of Adulteration in Honeys. 1. Study of Adulteration Effect on Honey Thermal Behavior. Journal of Agricultural and Food Chemistry 50(1), 203-208 (2002).
5. Cordella, C., Moussa, I., Martel, AC., Sbirrazzuoli, N., Lizzani-Cuvelier, L.: Recent Developments in Food Characterization and Adulteration Detection: Technique-Oriented Perspectives. Journal of Agricultural and Food Chemistry 50(7), 1751-1764 (2002).

Synthesis and Characterization of Dye-Based Phantom Tissue Samples with Tailored Visible-NIR Optical Properties

D. Raveenadeth[1], Shinto Babu[1], Saritha K Nair[2] and V. K. Shinoj[1*]

[1]*Optics and Spectroscopy Laboratory, Department of Physics, Union Christian College, Aluva*

[2]*Mar Athanasius College (Autonomous) Kothamangalam, Kerala-686666*

**shinojvk@uccollege.edu.in*

Abstract. Extraction of diagnosable information from tissue-pathologies, using *in-vivo* spectroscopic techniques, by analyzing diffuse reflectance, absorption and fluorescence is widely recognized for its potential. Primary challenge in utilizing this potential is the fabrication and optical characterization of phantom tissues, mimicking the optical properties of dermatological samples. Wide range of applications for phantom tissues, ranges from preliminary clinical studies to development of database for the standardization and calibration of *in-vivo* spectroscopic instruments. We addressed the fundamental challenge by fabricating thin, solid, tissue-simulating polydimethylsiloxane (PDMS) phantoms with tailored absorption properties and endogenous fluorescent properties, using bio-compatible dyes such as methylene blue, indocyanine green and sodium fluorescein. We also validated and evaluated the performance of the phantom tissues using diffuse reflectance and fluorescence studies to substantiate its use in clinical studies.

Keywords: Phantom, Diffuse Reflectance Spectroscopy, Probe, Fluorescence, Biomedical Optics.

1 Introduction

Clinical dermatological research and development for non-invasive, *in-vivo* diagnostic tool, requires standardization and calibration of biomedical imaging systems [1-3]. This is usually achieved by phantom tissue samples, mimicking the optical properties such as absorption, scattering and cellular autofluorescence of human skin [4-8]. When light is transported within skin, by means of broadband light source and probe arrangement, scattering, absorption and auto fluorescence [9-12] occurs due to the inhomogeneous distribution of chromophores, blood and pigments [13]. Scattering is caused

by various components ranging from cell nucleus to cellular-walls. The absorption exhibited is the combined effect of the tissue components such as blood chromophores (specifically different forms of haemoglobin and bilirubin), melanin, water, hair follicles, sweat glands and collagen fibers. Autofluorescence in tissue is caused by fluorescent-biochemical species (fluorophores) [14]. The therapeutic window (600-1300 nm) provides diagnosable information about abnormalities which will be reflected in the optical parameters [15].

Phantom tissues with tunable and tailored scattering, absorption and fluorescent properties are a requisite in the development of biomedical image based diagnostic tools. Conventional silicone-based phantom preparation, yielding repeatable result-giving methods, advanced with the effort of Ayers et. al. [8], which uses nigrosine as absorbing agent and TiO_2 as scattering agent. Its optical properties are distributed in a wide, flat band of wavelengths in visible region with a characteristic absorption peak of PDMS at 910 nm [8]. Attempts had been expended to synthesize multi-layer phantoms to mimic optical properties of dermis, epidermis and subcutaneous fat using India Ink, Coffee Powder and Nigrosine - all of them being absorbing agents with flat absorption spectra [16]. Optical properties at discrete wavelengths of this flat spectra were studied in detail, later in the course of time, by Greening et al. [7,17], Saager et al. [6] and Kennedy et al. [5]. There had been innovations in using dyes in the synthesis of tissue-mimicking phantoms within absorption bands from 650-800 nm using zinc phthalocyanine by Monte et al. [4]. It can be observed that these works had been focusing on introducing optical properties in a range of wavelengths by means of absorbing and scattering agents whose properties are observed in a band. More importantly, the specific nature of reflectance spectra of human skin with characteristic absorption exhibited by chromophores and the trends of increase in reflectance in the visible region, has not been properly addressed in the fabrication of tissue mimicking samples. The autofluorescence exhibited by skin, despite containing diagnosable potential, had also been left unanswered even in the saturated stage of tissue fabrication process.

Multi-layered phantoms with different choices for scattering, with flat absorption bands have been reported to date. This paper, envisions to address the improvements in the fabrication process by introducing tailored and characteristic absorption and fluorescence in existing silicone-based solid

tissue samples, by using bio-compatible dyes in visible and near infra-red (NIR) region.

2 Methodology

The fabrication of tissues in this study is inspired from Ayer's method [8], which uses polydimethylsiloxane (PDMS) as base matrix. PDMS is a widely used, transparent, viscous, silicone-based polymer which can be solidified by cross-linking using an appropriate curing agent under chemical and thermal treatment. Although being chemically hydrophobic, PDMS exhibit an impeccable resemblance in refractive index, compared to average refractive index of human skin, making it an ideal and desirable choice for the phantom tissue fabrication [18,19]. The widely used choice of scattering agent TiO_2 is employed in the present study [8,16,20,21]. Besides being a common ingredient in cosmetic products, the distribution and size of TiO_2 are similar to cellular structures in skin that scatter light.

Different dyes such as Acridine Yellow, Congo Red, Methylene Blue, Indocyanine Green, Sodium Fluorescein, India Ink (Nigrosin) and Coffee powder were tested for absorption studies at different concentrations, for mimicking the absorption properties of tissue samples, exhibited in the UV-Visible-NIR wavelength region. Finally, one absorbing agent each from UV-Visible and NIR region, for their characteristic absorption in the said region, was chosen, namely Methylene Blue and Indocyanine Green (ICG). Methylene Blue, a commonly available organic dye and medicine for methemoglobinemia, shows absorption in visible region [22]. ICG is a fluorogenic dye, often used as indicator in medical diagnostics, which exhibits a good absorption and subsequent emission in the NIR region. ICG also shows absorption near the isobestic point of Hemoglobin and Oxyhemoglobin [23]. In addition to the above, Sodium Fluorescein, a widely used diagnostic tool in ophthalmology, is added to exhibit endogenous fluorescence [24].

2.1 Sample preparation

Synthesis of solid tissue samples to mimic optical properties consisted of four major ingredients - PDMS, Methylene Blue, ICG, and Sodium Fluorescein. PDMS, a commonly used base matrix, is mixed in 10:1 ratio with suitable curing agent (Sylgard 184 Silicone Elastomer, 761028, Sigma Aldrich).

Absorption properties in the visible and NIR regions are controlled by two absorbing agents – Methylene Blue solution and ICG (I2633, Sigma Aldrich). Sodium Fluorescein provides fluorescence property to the tissue in the visible region.

Sylgard 184, a 2 g clip size packet, containing PDMS to curing agent in the ratio 10:1, is mixed thoroughly and sonicated for 15 minutes. Bubbles formed are popped out. Solutions in methanol of Methylene Blue, ICG and Sodium Fluorescein are prepared. These are mixed together in concentration described in Table 1 and 2. This is mixed with rutile TiO_2 and is made into a paste. 200 µL solution of PDMS with curing agent is added to this paste and is mixed mechanically for 15 minutes. This is coated on a generic glass slide mould of custom width and length and having borders made of microscope cover slides with approximate thickness of 0.15 mm. This arrangement is placed in a hot-air oven at 150 degree Celsius for 30 minutes. The cured sample will have uniform optical properties, which can be confirmed by taking DRS from different locations of the sample. We mention the synthesis of six samples S1-S6 by this process, the details of which are given in Table 2.

2.2 Characterization Techniques

Diffused Reflectance Spectroscopy

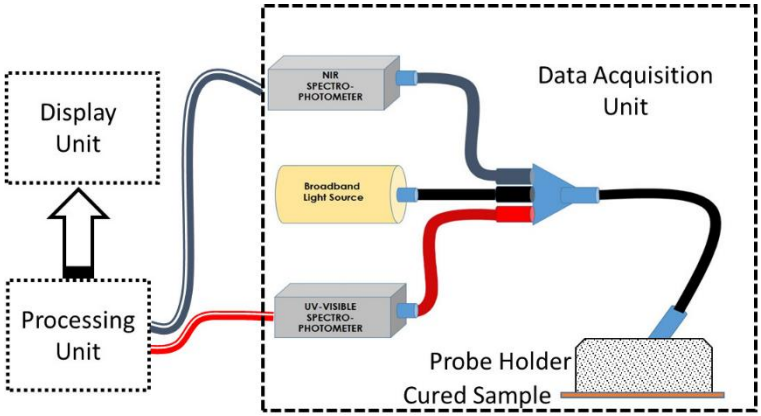

Fig. 2. Schematic arrangement of DRS setup.

A probe-based diffuse reflectance arrangement is used to ensure the potential use of the phantom samples, in the standardization and characterization of biomedical imaging tools for diagnostic applications. The schematics of portable diffused reflectance measurement system used in our study is illustrated in Figure 1. Broadband light from a tungsten-halogen source (HL 2000 LL, Ocean Optics) is incident on cured phantom sample and the reflected light is collected via the same probe kept at 45º. Reference spectrum using PTFE standard is stored in the acquisition system and dark current corrections are made, prior to the data acquisition. The collected light is split using a splicer and passed through two spectrophotometers covering UV-Visible (Flame T XR1 ES, Ocean Optics) and NIR (Flame NIR, Ocean Optics) regions separately. The data is obtained through interfacing software and is stitched together. Intensity of reflection is plotted versus wavelength and the obtained DRS spectrum is compared with the DRS of skin taken near radial artery.

Fluorescence Measurements

A monochromatic LED source of wavelength 447 nm was used to excite the sample using above mentioned arrangement. Reflected light is analyzed using a UV-Vis spectrophotometer to confirm the successful incorporation of fluorescence properties into the fabricated phantom tissue.

3 Results and Discussions

In the initial stages of current study, the absorption properties were mimicked using Nigrosin and Coffee powder, as suggested in pioneering works in tissue fabrication. The fluorescence was introduced using Sodium Fluorescein. Absorption of Nigrosin and Coffee powder in methanol solution was studied and compared with the absorption centers exhibited by chromophores of skin in the DRS spectrum. The representative images of the samples prepared and their DRS spectrum in comparison with human skin is shown in Figure 2. The intensity of reflection is found to increase with wavelength with no significant absorption in NIR. The intensity doesn't decrease as seen in the case of DRS of skin in NIR region. This shortcoming of absorbing agents with flat-band

absorption regions had to be overcome with different choices of absorbing agents.

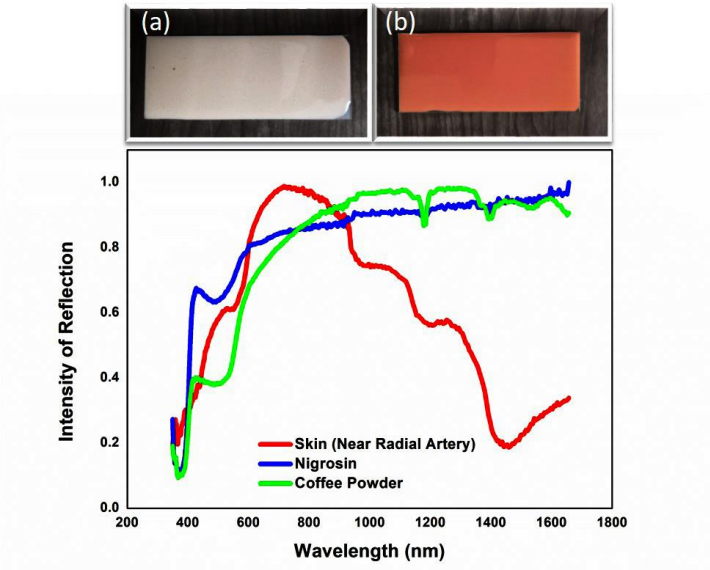

Fig. 2. Pictures of the phantom samples prepared using (a) India Ink (Nigrosin) and (b) Coffee powder. (c) DRS spectra of samples in (a) and (b) compared with that of skin (near radial artery).

Various dyes and fluorescent agents were tried in order to tailor absorption and endogenous fluorescence properties of the phantom tissue samples, after preliminary studies. Solutions with dyes such as Acridine Yellow, Indocyanine Green, Methylene Blue, Sodium Fluorescein and Congo Red were prepared in methanol with varying concentrations. The absorption of dyes compared with that reported in literature [25,26]. Indocyanine Green (800 nm), Methylene Blue (650 nm), and Sodium Fluorescein were chosen for the fabrication process for the close resemblance in the absorption with intensity variation of DRS of skin, and on account of bio-compatibility of said dyes. A number of trials were done by varying the concentration of absorbing agent, scattering agents and fluorescent agent before the concentrations were optimized in order to meet the primary challenge of identifying the optimized concentrations of absorption agents to mimic the optical properties of dermatological samples.

An indicative result during the optimization procedure in synthesizing the tissue samples with Methylene Blue, Indocyanine Green and Sodium Fluorescein with TiO_2 as scattering agent in a PDMS base matrix, is given in Figure 3. In trial 1 to 3 (indicated as T1-T3), the concentration of scattering agent TiO_2 is increased gradually from T1-T3 while the concentration of other components is kept fixed, see Table 1. In trial T4-T6, concentration of scattering agent is kept fixed and the concentration of other components are increased from T4-T6 in an orderly fashion as given in Table 1. The obtained result mentioned here does not show absorption peaks of Methylene Blue and Sodium Fluorescence in visible region. The concentration optimization process was repeated until the samples showed tailored absorption properties.

Table 1. Details of the prepared samples T1-T6.

Sample Name	TiO_2 (mg)	Methylene Blue Concn. (M)	Indocyanine Green Concn. (M)	Sodium Fluorescein Concn. (M)
T1	10	0.1	0.5	0.1
T2	15	0.1	0.5	0.1
T3	20	0.1	0.5	0.1
T4	15	0.006	0.03	0.006
T5	15	0.01	0.05	0.01
T6	15	0.02	0.1	0.02

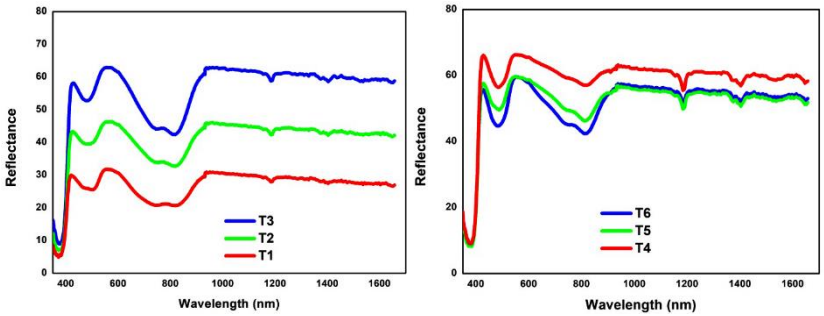

Fig. 3. Diffused reflectance spectra of samples (a) on increasing the concentration of the scattering agent (T1 to T3) while keeping the concentration of absorbing agent fixed, and (b) on increasing the concentration of absorbing agent (T4 to T6) while keeping the concentration of scattering agent fixed.

The optimized concentrations for which the samples showed tailored absorption properties are summarized in the Table 2. In samples S1-S3, concentration of scattering agent is varied while keeping the other parameters fixed. In samples S4-S6, the concentration of absorption controlling dyes were varied keeping other parameters unchanged. Photographs of the cured samples which can form database of different color palette, are shown in Figure 4.

Table 2. Details of the prepared samples S1-S6.

Sample Name	PDMS + CA (μL)	TiO_2 (g)	Methylene Blue		Indocyanine Green		Sodium Fluorescein	
			Concn. (M)	Vol. (μL)	Concn. (mM)	Vol. (μL)	Concn. (mM)	Vol. (μL)
S1	200	0.0106	1.03	50	0.3225	50	2.87	50
S2	200	0.0232	1.03	50	0.3225	50	2.87	50
S3	200	0.0325	1.03	50	0.3225	50	2.87	50
S4	200	0.0204	0.103	100	0.03225	100	0.287	100
S5	200	0.0216	0.0515	100	0.016125	100	0.1435	100
S6	200	0.0220	0.034	100	0.01075	100	0.0956	100

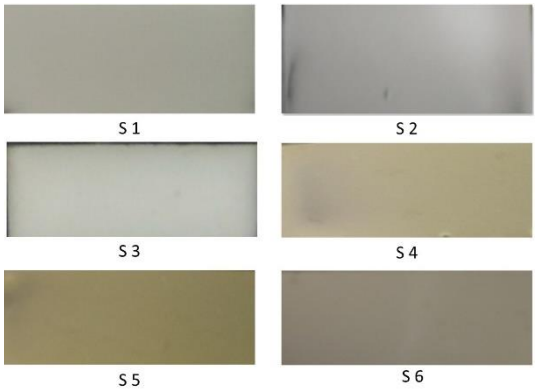

Fig. 4. Photographs of the prepared samples.

The characteristic absorption peaks of the absorbing agents observed in the DRS spectra of the synthesized phantom samples S1-S6 shown in Figure 5 clearly indicates the tailored optical properties.

On increasing the concentration of scattering agent while the concentration of absorbing agent is kept fixed, it is found that the intensity of reflection increases gradually from S1 to S3. The obtained result is shown in Figure 5(a). When the concentration of absorbing agent is decreased while the concentration of scattering agent is kept fixed, intensity of reflection increased gradually from S4 to S6. This is shown in Figure 5(b). The synthesized samples showing characteristic absorption properties thus validates our requirement of tailored optical properties. The obtained spectra are compared with the spectra of human hand taken near radial artery to study the similarities, see Figure 6. The intensity of DRS spectra of skin increases with increase in wavelength upto 650 nm and decreases with further increase in wavelength, specifically in NIR region. In this spectra, characteristic absorptions of oxyhaemoglobin, deoxyhaemoglobin can be seen around 430 nm and 550 nm respectively.

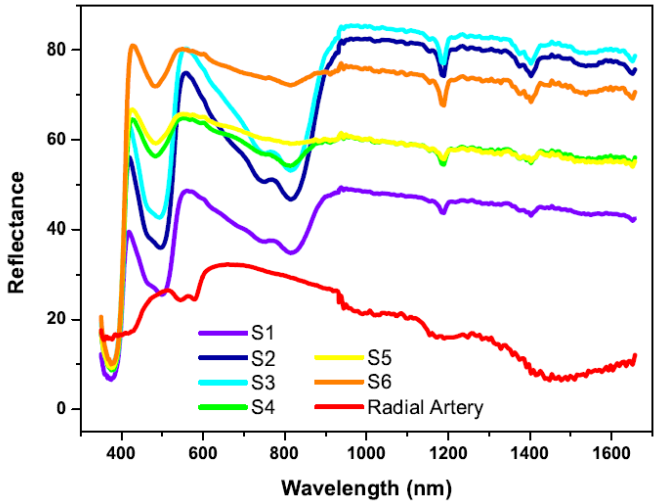

Fig. 6. DRS phantoms with DRS obtained from near radial artery.

The reported sample also exhibits endogenous fluorescence in visible region due to the presence of Sodium Fluorescein. The fluorescence spectrum obtained on exciting the sample with an LED source of wavelength 447 nm is shown in Figure 6. This is to mimic the auto-fluorescence in the skin. It is to be noted that the endogenous auto-fluorescence exhibited by human skin due

to the presence of reduced nicotinamide adenine dinucleotide, NAD(P)H, has emission maxima at 450 nm.

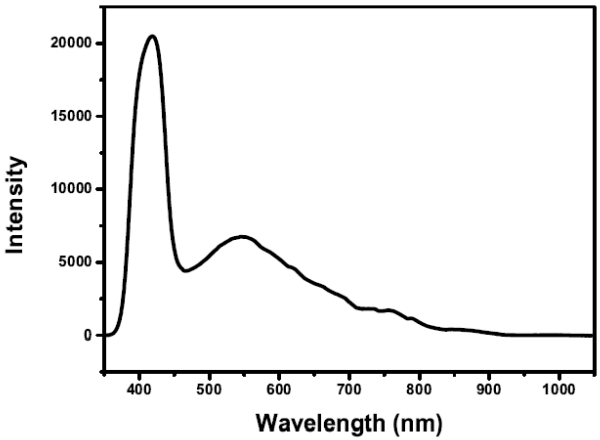

Fig. 7. Fluorescence spectra of synthesized phantom sample.

The complex and heterogeneous structure with the chromophores and fluorophores embedded in different layers makes it exceptionally difficult to mimic the optical properties of human skin, yet alone morphological. Existing organic dyes, which are already been proven to be biocompatible and are being used in the realm of diagnostics, provides tailored absorption properties to the phantom. It is to be noted that a shift in absorption can be observed with change in concentration due to molecular aggregation. The samples synthesized, in addition to having characteristic and tailored absorption, also shows similar trends in variation of diffuse reflectance with wavelength, as that of human skin. The autofluorescence exhibited by human skin is also successfully mimicked by the synthesized samples.

4 Conclusion

Tailoring of optical properties in solid phantom tissue samples using bio-compatible organic dyes used in diagnostic tools has potential applications in bio-medical instrumentation. The different color palette of human skin tone

arising from anthropological and dermatological factors can be mimicked by samples of varying intensity synthesized by varying concentration of the dyes. Although it is impossible to mimic the exact same properties of human skin due to its complex structure and presence of chromophores, samples we report displayed remarkable similarity in the nature of relative intensities up to 850~nm. The obtained results suggest a promising approach for fabrication of phantoms mimicking the optical characteristics of the biological tissues. The tunable properties of the tissues along with the low-cost of fabrication makes this technique a promising one for bio-medical applications.

Acknowledgments

Authors acknowledge the financial support received through DST-SERB (File No: ECR/2016/001708 dated 24-March-2017) under the scheme Early Career Research Award to Dr. Shinoj V K, the corresponding author.

References

1. Pogue, B.W., Patterson, M.S.: Review of tissue simulating phantoms for optical spectroscopy, imaging and dosimetry. Journal of biomedical optics 11(4), 041102 (2006).
2. Bouchard, J.P., Noiseux, I., Veilleux, I., Mermut, O.: The role of optical tissue phantom in verification and validation of medical imaging devices. In 2011 International Workshop on Biophotonics, IEEE, 1-3 (2011).
3. Shinoj, V.K., Murukeshan, V.M., Baskaran, M., Aung, T.: Integrated flexible handheld probe for imaging and evaluation of iridocorneal angle. Journal of biomedical optics 20(1), 016014 (2015).
4. Monte, A.F.G., Reis, A.F., Junior, L.B.C., Antunes, A.: Preparation and quantitative characterization of polydimethylsiloxane optical phantoms with zinc-phthalocyanine dye absorbers. Applied optics 57(20), 5865-5871 (2018).
5. Kennedy, G.T., Lentsch, G.R., Trieu, B., Ponticorvo, A., Saager, R.B., Durkin, A.J.: Solid tissue simulating phantoms having absorption at 970 nm for diffuse optics. Journal of biomedical optics 22(7), 076013 (2017).
6. Saager, R.B., Quach, A., Rowland, R.A., Baldado, M.L., Durkin, A.J.: Low-cost tissue simulating phantoms with adjustable wavelength-dependent scattering properties in the visible and infrared ranges. Journal of biomedical optics 21(6), 067001 (2016).
7. Greening, G.J., Powless, A.J., Hutcheson, J.A., Prieto, S.P., Majid, A.A., Muldoon, T.J.: Design and validation of a diffuse reflectance and spectroscopic microendoscope with poly (dimethylsiloxane)-based phantoms. In Optical

Diagnostics and Sensing XV: Toward Point-of-Care Diagnostics, International Society for Optics and Photonics 9332, 93320R (2015).
8. Ayers, F., Grant, A., Kuo, D., Cuccia, D.J., Durkin, A.J.: Fabrication and characterization of silicone-based tissue phantoms with tunable optical properties in the visible and near infrared domain. In Design and Performance Validation of Phantoms Used in Conjunction with Optical Measurements of Tissue, International Society for Optics and Photonics 6870, 687007 (2008).
9. Lister, T., Wright, P.A., Chappell, P.H.: Optical properties of human skin. Journal of biomedical optics 17(9), 090901 (2012).
10. Igarashi, T., Nishino, K., Nayar, S.K.: The Appearance of Human Skin (2005).
11. Tuchin, V.V.: Light scattering study of tissues. Physics-Uspekhi 40(5), 495 (1997).
12. Monici, M.: Cell and tissue autofluorescence research and diagnostic applications. Biotechnology annual review 11, 227-256 (2005).
13. Bashkatov, A., Genina, E., Kochubey, V., Tuchin, V.: Optical properties of human skin, subcutaneous and mucous tissues in the wavelength range from 400 to 2000 nm. Journal of Physics D: Applied Physics 38(15), 2543 (2005).
14. Anderson, R.R., Parrish, J.A.: The optics of human skin. Journal of investigative dermatology 77(1), 13-19 (1981).
15. Yavari, H.: Diffuse Reflectance Spectroscopy: Using Multivariate analysis method for determination of tissue optical properties (2016).
16. Saager, R.B., Kondru, C., Au, K., Sry, K., Ayers, F., Durkin, A.J.: Multilayer silicone phantoms for the evaluation of quantitative optical techniques in skin imaging. In Design and Performance Validation of Phantoms Used in Conjunction with Optical Measurement of Tissue II, International Society for Optics and Photonics 7567, 756706 (2010).
17. Greening, G.J., Istfan, R., Higgins, L.M., Balachandran, K., Roblyer, D.M., Pierce, M.C., Muldoon, T.J.: Characterization of thin poly (dimethylsiloxane)-based tissue-simulating phantoms with tunable reduced scattering and absorption coefficients at visible and near-infrared wavelengths. Journal of biomedical optics 19(11), 115002 (2014).
18. Bays, R., Wagnieres, G., Robert, D., Theumann, J.F., Vitkin, A., Savary, J.F., Monnier, P. van den Bergh, H.: Three-dimensional optical phantom and its application in photodynamic therapy. Lasers in Surgery and Medicine: The Official Journal of the American Society for Laser Medicine and Surgery 21(3), 227-234 (1997).
19. Bolin, F.P., Preuss, L.E., Taylor, R.C., Ference, R.J.: Refractive index of some mammalian tissues using a fiber optic cladding method. Applied optics 28(12), 2297-2303 (1989).
20. Grant, A.M, Sry, K., Saager, R., Ayers, F., Pfefer, T.J., Kelly, K.M., Tseng, S.H., Durkin, A.J.: Diffuse optical spectroscopy of melanoma-simulating silicone phantoms. In Biomedical Applications of Light Scattering III, International Society for Optics and Photonics 7187, 718702 (2009).

21. Firbank, M., Oda, M., Delpy, D.T.: An improved design for a stable and reproducible phantom material for use in near-infrared spectroscopy and imaging. Physics in Medicine & Biology 40(5), 955 (1995).
22. Ramanamurthy, S.V.: Methemoglobinemia: a reappraisal with an Indian perspective. Hematology (2013).
23. Barlow, R.B., Polanyi, M.L.: Absorption measurements for oxygenated and reduced hemoglobin in the range 0.6-1.88 microns. Clinical Chemistry 8, 67-71 (1962).
24. INFABOOST - engerix-b-20mg-adult: https://www.hpra.ie/docs/default-source/vaccine-pils/engerix-b-20mg-adult.pdf.
25. Salem, A.: A Study on the Structural, Electrical and Dielectric Properties of Fluorescein Dye as a New Organic Semiconductor Material. IOSR Journal of Electrical and Electronics Engineering 11(6), 34-41 (2016).
26. Kochubey, V., Kulyabina, T., Tuchin, V., Altshuler, G.: Spectral characteristics of indocyanine green upon its interaction with biological tissues. Optics and Spectroscopy 99(4), 560-566 (2005).

Green synthesis of Cerium oxide nanoparticles using Aloe vera extract

Aleena Norbert[1], Sainadh C U[1], Rachel Reena Philip[1]
[1]*Thin Film Research Lab, Department of Physics, Union Christian College, Aluva, Kerala -683102*
**reenatara@gmail.com*

Abstract. Green nanotechnology is an emerging field of nanoscience, which has received much attention in recent years for the synthesis of nanomaterials through environment friendly routes. This work focuses on the synthesis of cerium oxide nanoparticles using this simple, cost effective and environment friendly green method. Here, aloe vera leaf extract is used as the reducing and stabilizing agent in order to control size and morphology. The structure and morphology of the nanoparticles are investigated using X-ray diffraction spectroscopy and Field emission scanning electron microscopy. The XRD confirms the formation of cubic fluorite structure of CeO_2 nanoparticles and FESEM shows a homogeneous grain structure with smooth-edges. The optical characterizations are carried out using UV-Visible DRS and Photoluminescence spectral analysis. A direct band gap of 3.3eV is detected from the former and the peaks in PL spectra suggests the presence of defect centers localized between the Ce 4f and O 2p levels. Further, the FTIR spectral analysis reveals the Ce-O and O-H stretching vibrations.

Keywords: Phytosynthesis, Cerium oxide, Aloe-vera extract.

1 Introduction

Green nanotechnology is an emerging field of nanoscience, that has earned much attention in recent years for developing the synthesis processes of nanomaterials through green synthetic and environmental friendly routes. In green synthesis, extracts from fungi, algae, bacteria, and plants that provide metabolites to act as reducing agents are commonly used.

Research to date indicates that nanoparticles synthesized from plant extracts hold great potential for use in photonics, electronics, medicine and waste treatment due to its environmental friendliness and unique single-step synthesis involving reduction followed by stabilization and capping of nanoparticles. They create innovative opportunity to design and develop novel

methods to make metal and metal oxide nanoparticles for antimicrobial, catalytic, biosensor and therapeutics applications as well as for cancer diagnosis and photodegradation of dyes [1,2].

Phytosynthesized cubic fluorite type cerium dioxide nanoparticles are found to be non-toxic and biocompatible with normal human cells. Hence it is used for targeted drug delivery. They also circumvent the existing problems of drug resistant bacteria and serve as excellent antibacterial agents in comparison with other metal oxides. The quick transition of the oxidation state between Ce^{3+} and Ce^{4+} of CeO_2 nanoparticles produce Reactive Oxygen Species (ROS) like OH^-, H_2O_2 and O_2^{2-} on the surface which can tune the activities of the nanoparticles [3].

In this work samples are prepared using plant extracts and their structural, morphological and optical characterization are done using X-Ray Diffraction techniques (XRD), Field emission Scanning Electron Microscopy (FE-SEM), Fourier Transform Infrared Microscopy (FT-IR), UV-Vis DRS and Photoluminescence measurements.

2 Materials and Methods

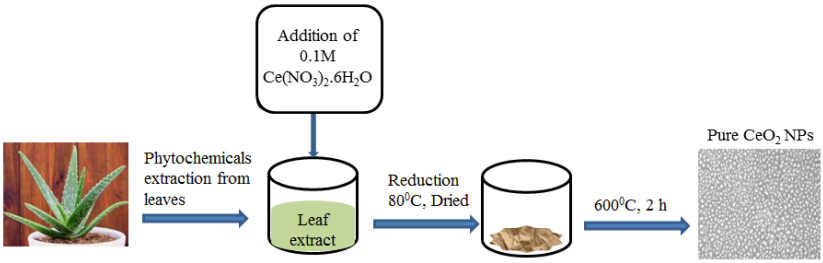

Fig. 1. Synthesis scheme of CeO2 NPs.

2.1 Synthesis of CeO_2 NPs

CeO_2 NPs are synthesized by dissolving 0.1M of cerium nitrate hexahydrate ($(Ce_2(NO_3)_3.6H_2O$), Himedia) in 40 mL distilled water with continuous stirring. When the precursor salt is completely dissolved, 10 mL of aloe vera

leaf extract prepared by boiling aloe vera pulp in distilled water at 80^0C is added and stirred for 30 min continuously. Then it is transferred to a hot plate and heated at 80^0C till the supernatant got evaporated. The resultant powder is then pounded into fine powder and annealed at 600^0C for 2 h.

2.2 Characterization

XRD analysis is carried out using Bruker D8 Advance X-ray diffractometer and the crystal structure and crystallite size of the NPs are studied. FTIR spectral analysis is done with a FTIR spectrophotometer in the range between 500 and 4000 cm^{-1} for determining the functional groups. The surface morphology is analyzed by Carl Zeiss FESEM. Optical band gap of the sample is determined using UV-Vis DRS spectrophotometer. Photoluminescence studies are performed at room temperature on Horiba Fluoromax-4C with an excitation wavelength of 350 nm.

3 Results and Discussions

3.1 X-ray diffraction studies

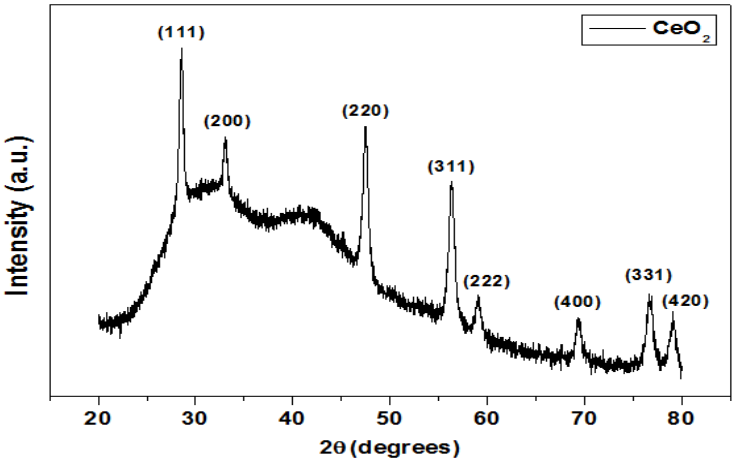

Fig.2. XRD pattern of CeO_2 NPs.

The XRD pattern of CeO_2 NPs is shown in Fig.1. The peaks at 2θ values of 28.6^0, 33.1^0, 47.5^0, 56.3^0, 59.1^0, 69.4^0, 76.7^0 and 79.2^0 correspond to (111),

(200), (220), (311), (222), (400), (331) and (420) planes respectively. This indicates the cubic fluorite structure of CeO_2 NPs in accordance with the JCPDS card no. 034-0394. The average crystallite size D of the sample is ~28 nm, which is calculated using the Debye-Scherrer formula given as

$$D = \frac{0.9\lambda}{\beta cos\theta} \quad (1)$$

Where λ is the wavelength of the X-ray used (1.5405 Å), β is the full width at half maximum in radians and θ is the Bragg's diffraction angle.

3.2 FTIR Spectroscopy

The FTIR spectrum of the sample is given in Fig. 3. The FTIR spectroscopy is done within a range of 500-4000 cm^{-1}. The band at 606 cm^{-1} corresponds to the Ce-O strectching vibration. The appearance of the band at 1216 cm^{-1} is related to the vibrations of C-O-C functional group. Carbon is a contaminant that bonds with hydroxyl groups, oxygen and hydrogen on the surface. The bands around 1367, 2965 and 3018 cm^{-1} correspond to C-H group. The much intense band at 1738 cm^{-1} is attributed to the C=O group. The small band at 3744 cm^{-1} is associated with the O-H stretching vibration of residual water and hydroxyl groups [3].

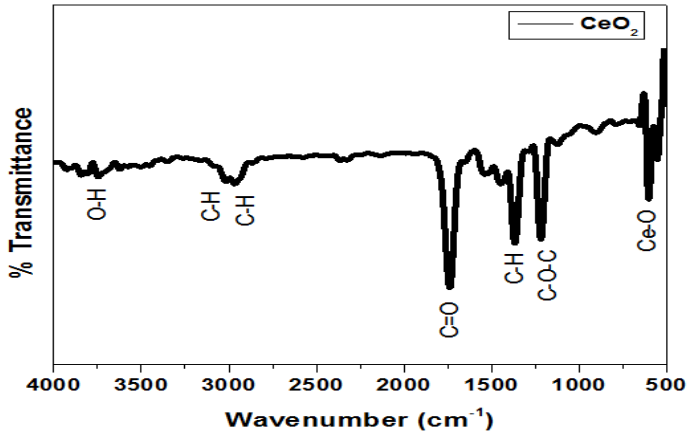

Fig.3. FTIR spectrum of CeO_2 NPs.

3.3 FESEM Studies

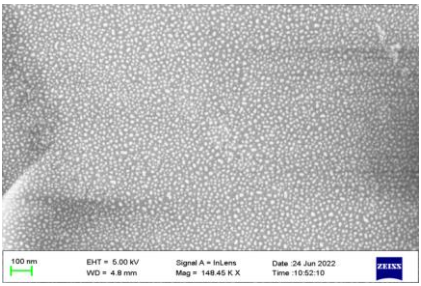

Fig.4. FESEM image of CeO_2 NPs

The surface morphology of the CeO_2 NPs is shown in Fig 4 at 100 nm scale. The FESEM image clearly shows a homogeneous appearance of smooth edged grains with sizes in the range of 12-30 nm.

3.4 Diffuse Reflectance Spectroscopy Studies

The band gap energy of the sample is determined from the reflectance data using the Kubelka-Munk function

$$F(R) = \frac{(1-R)^2}{2R} \qquad (2)$$

where R is the reflectance. The direct band gap obtained by plotting [F(R) X hυ]^2 vs hυ for CeO_2 NPs is found to be 3.3 eV,which falls in the UV region of solar spectrum.

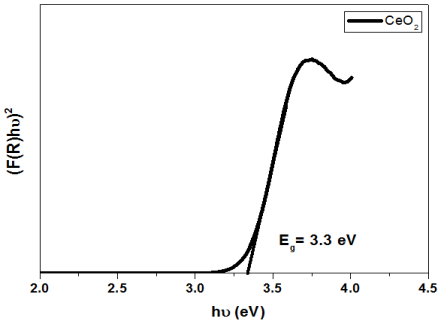

Fig.5. Kubelka-Munk plot of CeO_2 NPs

3.5 Photoluminescence Spectroscopy

Fig 6 shows the PL spectrum of CeO_2 NPs under the excitation wavelength of 350 nm. The violet emission peak at 438 nm is due to the defect states existing between the Ce 4f state and O 2p valence band. The two blue emission peaks observed at 450 and 468 nm are attributed to localization of the energy levels between the Ce 4f state and O 2p. The blue-green emission peaks at 481 and 491 nm are due to surface defects in the CeO_2 NPs. The green emission peak observed at 561 nm is due to the low density of oxygen vacancies [4].

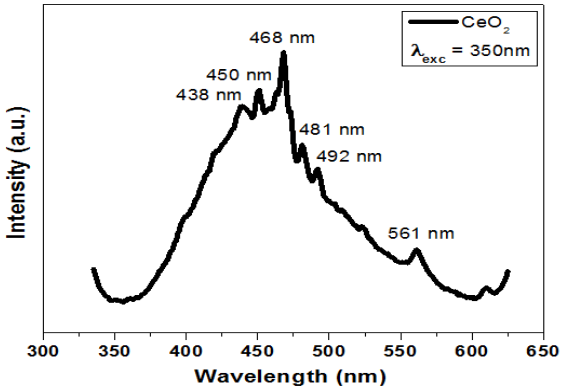

Fig.6. PL spectrum of CeO_2 NPs

4 Conclusion

CeO_2 NPs are successfully synthesized by green method using aloe vera extract as reducing and stabilizing agent. The material properties are examined by XRD, FTIR, FESEM, DRS and PL. Though the small size and smooth edged morphology of the nanoparticles are advantageous properties that aid antibacterial applications, the wide band gap of CeO_2 that falls in the UV region acts as an inhibiting factor to its efficiency. Therefore, various strategies like metal/non-metallic doping, structural modifications and coupling with other semiconductors are used to reduce the band gap and to increase its efficiency in antimicrobial applications.

References

1. Z. Foroutan, A. R. Afshari, Z. Sabouri, A. Mostafapour, B. F. Far, M. Jalili-Nik, M. Darroudi, *Ceram. Int*., 2022, 48, 30441–30450.
2. P. Maleki, F. Nemati, A. Gholoobi, A. Hashemzadeh, Z. Sabouri, M. Darroudi, *Inorg. Chem. Commun*., 2021, 131, 108762.
3. A. Thill, O. Zeyons, O. Spalla, F. Chauvat, J. Rose, M. Auffan, A. M. Flank, *Environ. Sci. Technol*., 2006, 40, 6151.
4. S. Safat, F. Buazar, S. Albukhaty, S. Matroodi, *Sci. Rep*., 2021, 11, 1–11.
5. K. Kumari, R.N. Aljawfi, A.K. Chawla, *Ceram Int*, 2020, 46, 7482.

Cyclic Voltametric (CV) studies of solvothermally synthesized $CsTiBr_3$/rGO composite for supercapacitor applications

K A Benazeera Beegum[1], Christeena Thomas[1], Saranya Sasi[1], Suvarna Ganesh[1], Alex Mathew[1], R Reshmi[1*]

[1]*Optoelectronic and Nanomaterials Research Laboratory, Department of Physics, Union Christian College, Aluva, Kerala, India—683102*

**rreshmi@gmail.com*

Abstract. Inorganic halide perovskites (IHP), ABX_3 (A and B are inorganic cations and X is halide anion), are emerging materials with excellent optoelectronic properties. A lead free IHP of $CsTiBr_3$ and its composite with reduced graphene oxide (rGO) is synthesized by solvothermal process. The structural analysis by XRD and Raman spectrum could confirm the composite formation of $CsTiBr_3$ with rGO. The pure $CsTiBr_3$ is composed of clusters of nanorods having different length and cross-sectional area. The incorporation of rGO into the $CsTiBr_3$ crystal caused morphological modification. The two-dimensional sheets of rGO becomes a mattress in which the nanorods can lie. The band gap of $CsTiBr_3$ nanorods reduced from 3.05eV to 2.96eV by the incorporation of 1% rGO. The structural modification and bandgap tuning by the $CsTiBr_3$/rGO composite resulted in drastic decrease in impedance. The specific capacitance, areal capacitance and double layer capacitance shows multifold increase due to the impedance variation.

Keywords: Inorganic halide perovskites, Specific capacitance, Areal capacitance, Double layer capacitance.

1 Introduction

Halide perovskites (HP) are emerging materials in the field of energy storage applications because of its promising ion diffusion properties [1-3]. Supercapacitors and batteries are the two remarkable energy storage devices. Efforts are ongoing to find out the reason for the increased mobility of ion in lithium ion battery to a large extent through halide perovskite incorporation [4]. Unlike batteries, supercapacitors possess long cycle stability, higher reversibility, fast charging/discharging and power performance [5,6]. The electronic and ionic conduction nature of HPs are utilised in superconductors

to store energy via reverse adsorption process on porous electrodes [7,8]. The anions and cations in a perovskite material have low activation energy and can easily move through the perovskite active layer when subjected to an external electric field or under light illumination.

The first HP supercapacitor is Methylammonium lead iodide ($MAPbI_3$) based by Zhou et al with an areal capacitance of 3.68µF/cm^2 [9] and later the areal capacitance of these supercapacitors could improve upto 21.5 µF/cm^2 [10]. An all-inorganic halide perovskite of $CsPbI_3$ microwire supercapacitors was also reported with an excellent areal capacitance of 7.23mF/cm^{2}at a scan rate of 2mV/S [11]. The major environmental issue raised by the presence of toxic lead in these active materials limits its usage in commercial applications. Lead free halide perovskites supercapacitors are also reported with $(CH_3NH_3)_3Bi_2I_9$, $(CN_2SH_5)_3BiI_6$, $KCoF_3$ and $KNiF_3$[12-14] with excellent capacitance retention ability after 1000 charge-discharge cycles. In the present study, we are reporting for first time the areal capacitance and double layer capacitance of a lead-free halide perovskite of $CsTiBr_3$ nonorod and its composite with reduced graphene oxide (rGO). rGO is an extraordinary material with unique optoelectronic properties [15,16]. The two-dimensional sheet like structure of rGO enhances the surface area of $CsTiBr_3$ nanorods that makes it suitable for applications which require large area. Besides to surface area enhancement the presence of rGO intensifies the conductivity too. The morphological modulation and improved surface area in the $CsTiBr_3$/rGO composite will improve the capacitative characteristics to a great extent 7[17].

2 Experimental

The nanorods of $CsTiBr_3$ and $CsTiBr_3$/rGO composite was synthesized via solvothermal method. The precursors cesium bromide (CsBr) and titanium bromide ($TiBr_4$) in 1:1 ratio is dissolved in hydrobromic acid (HBr). The solution is magnetically stirred for 20minutes and poured into Teflon beaker. For the synthesis of $CsTiBr_3$/rGO composite, graphene oxide powder synthesized via modified hummers method is added along with other precursors. The Teflon beaker is enclosed in an autoclave and kept inside hot air oven for 24hours. The solvothermal process is carried out at 200^{0}C. The precipitate obtained is vacuum filtered and is used to prepare the dye for CV analysis. 5mg of $CsTiBr_3$ in 1ml water is sonicated for two hours to get a uniform dye suspension. 10µl of this dye is micropipetted and dropped on

glassy carbon electrode to dry. The electrode is dipped in 0.5molar H_2SO_4 electrolyte and set as the working electrode in the three electrode system.

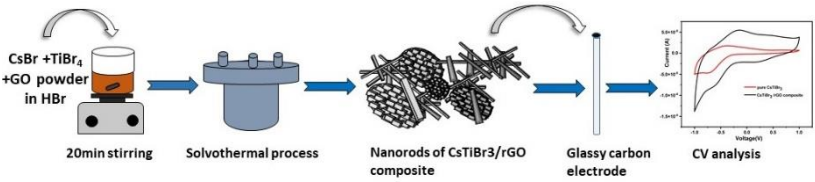

Fig. 1. Schematic representation of the solvothermal synthesis of pure $CsTiBr_3$ and $CsTiBr_3$/rGO composite.

3 Results and Discussions

The structural characterization of the pure $CsTiBr_3$ and $CsTiBr_3$/rGO composite was done by XRD analysis. Figure (1.a) illustrates the XRD pattern of both samples. All the major peaks are indexed and in good agreement with ICDD 00-084-2420 which confirms the formation of $CsTiBr_3$. The XRD patterns are identical for both the samples and the characteristic XRD peaks of rGO is not seen in $CsTiBr_3$/rGO composite. Jijun et al [18]and Chen et al [19] reported the same result and explained the absence of XRD peak of rGO as the destroyed regular stacks of two dimensional sheets of rGO in a composite and the lean amount of rGO in the composite. The $CsTiBr_3$/rGO composite was prepared by adding only one weight percentage rGO to the precursors during the solvothermal synthesis. The increased full width at half maximum (FWHM) for the $CsTiBr_3$/rGO composite shows that the crystallinity has decreased on composite formation. The confirmation of the composite formation was done by EDAX and Raman spectrum analysis. The elemental characterisation by EDAX (figure 1.d) confirms the presence of cesium, titanium, bromine, carbon and oxygen in $CsTiBr_3$ /rGO composite. Besides to the Raman peaks of $CsTiBr_3$ bond stretching vibrations, the $CsTiBr_3$/ rGO composite has the D band G band vibrational peaks too (figure 1.b). The characterstic D band and G band vibrational peaks of carbon compounds at 1356cm^{-1} and 1580cm^{-1} [20,21] are shifted to 1362cm^{-1} and 1598cm^{-1}. The shift in these peaks indicates the $CsTiBr_3$/rGO composite preferably the discrete presence of rGO [22].

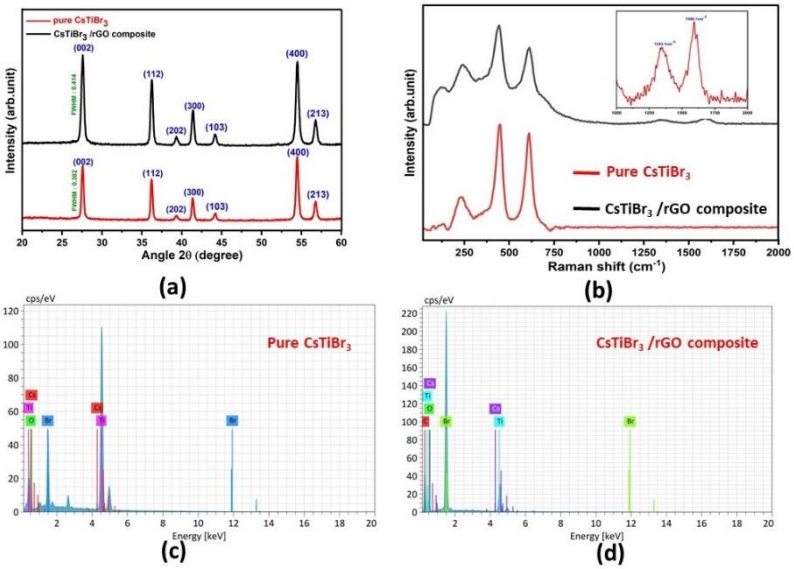

Fig. 2. (a) XRD pattern and (b) raman shift, (c)and (d) EDAX pattern of pure $CsTiBr_3$ and $CsTiBr_3$/rGO composite nanorods prepared by solvothermal method.

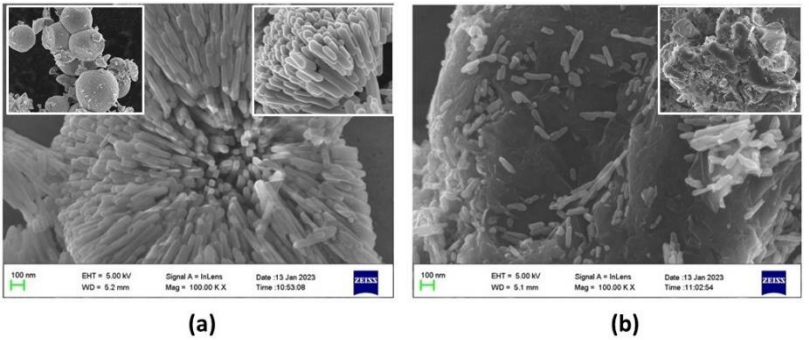

Fig. 3. FESEM images of (a) pure $CsTiBr_3$ and (b) $CsTiBr_3$/rGO composite nanorods prepared by solvothermal method.

The FESEM images of pure $CsTiBr_3$ and $CsTiBr_3$/rGO composite is shown in figure 2. The solvothermal synthesis resulted in nanorod formation of $CsTiBr_3$. The nanorods of $CsTiBr_3$ orderly arranged to get clusters and spheres. The length and cross-sectional area of each nanorod varies from each other. The shape of nanorods does not change in the composite formation with rGO. The nanorods are embedded in the two dimensional sheets of rGO. The 2D sheets on which the nanorods lie provides a conduction path for the charge carriers. The shift in raman peaks of rGO in the $CsTiBr_3$/rGO composite is an evidence to charge transfer between $CsTiBr_3$ and rGO [22].

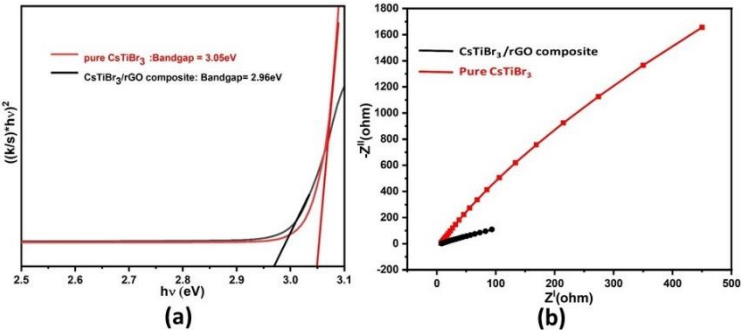

Fig. 4. (a) Kubulka munk plot and (b) Nyquist plot of pure $CsTiBr_3$ and $CsTiBr_3$/rGO composite nanorods prepared by solvothermal method.

The kubulka-munk plot is drawn between $\left(\frac{k}{s}h\nu\right)^2$ and hν where k and s are the absorption and reflection coefficients.

$$k = (1-R)^2 \ldots\ldots\ldots\ldots \quad (1)$$

$$S = 2R \quad \ldots\ldots\ldots\ldots \quad (2)$$

R is the reflectance obtained from DRS analysis

The bandgap of pure $CsTiBr_3$ is obtained as 3.05eV and that of $CsTiBr_3$/rGO composite as 2.96eV. The bandgap reduction is achieved through the composite formation with rGO.

The real and imaginary part of the impedence (Z^1 and Z^{11}) obtained from AC conductivity measurement is plotted. The drastic decrease in impedence for the $CsTiBr_3$/rGO composite compared to pure $CsTiBr_3$ is evident from the

Nyquist plot. The decreased impedence is attributed to the reduction in bandgap and the structural modification of $CsTiBr_3$/rGO composite. The two dimensional sheet of rGO in which the $CsTiBr_3$ is embedded causes easy passage of the charge carriers.

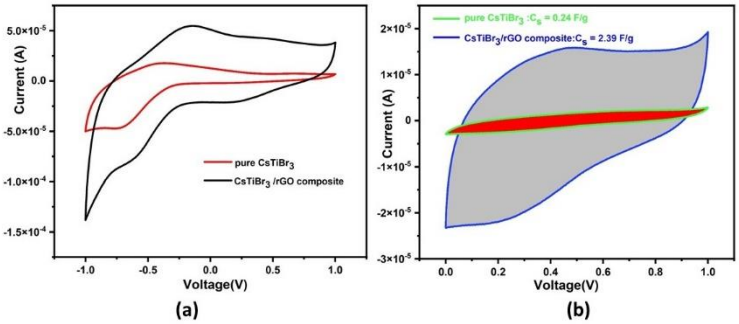

Fig. 5. The cyclic voltametric loop for voltage range (a) -1V to 1Vand (b) 0 to 1V of pure $CsTiBr_3$ and $CsTiBr_3$/rGO composite nanorods prepared by solvothermal method.

The cyclic voltametric loop for the voltage range -1V to 1V and 0 to 1V are drawn at scanning rate 100mV/s. The nonfaradic region in the positive voltage range of figure (5a) points to the possibility that the material can be used for supercapacitor application. The area of the current - voltage loop is a direct indication of the specific capacitance of the material [23]. The specific capacitance C_s is given by

$$C_s = \frac{Q}{mV} \dots\dots\dots\dots\dots (3), Q: Charge, m: mass \wedge V: Voltage$$

$$But Q = \cdots \dots\dots\dots\dots (4), I: Current, t: time$$

$$C_s = \frac{I}{m\left(\frac{V}{t}\right)} = \frac{I}{mk} \dots\dots\dots\dots\dots (5), k: scanningrate$$

$$I = C_s * m * k \dots\dots\dots\dots\dots (6)$$

The area (A) inside current(I) Vs voltage(V) loop for the charging and discharging process in a voltage range V_1 to V_2 is,

$$A = 2 * (V_2 - V_1) * C_s * m * k \quad \dots\dots\dots\dots\dots (7)$$

$$Cs = \frac{A}{2 * (V2 - V1) * m * k} \dots\dots\dots\dots\dots (8)$$

The specific capacitance of the pure $CsTiBr_3$ and $CsTiBr_3$/rGO composite is obtained as 0.24 F/g and 2.39 F/g. The increased specific capacitance for the $CsTiBr_3$/rGO composite is due to the reduction in impedance and increased surface area [23].

The areal capacitance of the $CsTiBr_3$ electrode is also calculated from the area of CV curve in the 0 to 1V range using the equation [24],

$$Arealcapacitance, C_A = \frac{AreaundertheCVcurve}{(V2-V1)*k*Areaoftheelectrode} \ldots\ldots\ldots\ldots\ldots (9)$$

The areal capacitance is calculated as 0.34mF/cm^2 and 3.3mF/cm^2 for the pure $CsTiBr_3$ and $CsTiBr_3$/rGO composite electrode respectively. The ten times increase in areal capacitance is again a measure of the increased surface area on composite formation.

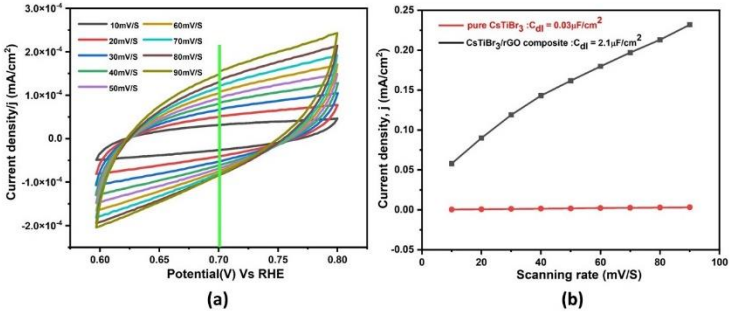

Fig. 6. (a)The cyclic voltametric loop at different scanning rate and (b) Δj Vs scanning rate curve of pure $CsTiBr_3$ and $CsTiBr_3$/rGO composite nanorods prepared by solvothermal method.

The double layer capacitance(C_{dl}) is the direct measurement of the capacity of an electrical double layer type super capacitors. In an electrical double layer capacitor, the two layers are formed by the electrons on the working electrode and ions in the electrolyte. The solvent attached to the electrode behaves as the dielectric medium between the opposite polarity carriers. The current density(j) against potential (V Vs RHE) curve at different scanning rate is plotted as in figure (6.a).

$$Currentdensity, j = \frac{CurrentI}{Areaoftheelectrode}\left(\frac{mA}{cm^2}\right)$$

$PotentialVVsRHE$ =E(Ag/AgCl) + E^e(Ag/AgCl) + 0.0591* p^H

E(Ag/AgCl) is the measured potential value
E^e(Ag/AgCl) = 0.1976 at 25°C
$p^H of 0.5 molar H_2SO_4$ = 0.03

The difference in current density (Δj) for the charging and discharging process at a particular scanning rate is calculated. The slope of Δj Vs scanning rate curve gives the double layer capacitance [25]. It can be seen that the double layer capacitance of $CsTiBr_3$/rGO composite has increased 70 times than the pure $CsTiBr_3$. The enhanced specific capacitance and double layer capacitance of $CsTiBr_3$/rGO composite can make use in charge storage applications.

4 Conclusion

A lead free IHP of $CsTiBr_3$ and its composite with reduced graphene oxide (rGO) is synthesized by solvothermal process. XRD analysis and Raman spectrum confirmed the composite formation of $CsTiBr_3$ with rGO. The pure $CsTiBr_3$ is composed of clusters of nanorods having different length and cross-sectional area. rGO brought morphological modification in the $CsTiBr_3$/rGO composite. In the composite, the naorods of $CsTiBr_3$ is embedded in the two dimensional sheet of rGO to facilitate easy charge flow and to improve the surface area. The band gap of $CsTiBr_3$ nanorods reduced from 3.05eV to 2.96eV by the incorporation of 1% rGO. The structural modification and bandgap tuning by the $CsTiBr_3$/rGO composite resulted in drastic decrease in impedance. The morphological modulation and impedence variation reflected in multifold increase in specific capacitance, areal capacitance and double layer capacitance in $CsTiBr_3$/rGO composite.

Acknowledgement

The authors gratefully acknowledge KSCSTE SARD scheme and DST-SERB (CRG/2018/003785) for the funding provided.

References

1. Almora, Osbel, et al. "Capacitive dark currents, hysteresis, and electrode polarization in lead halide perovskite solar cells." *The journal of physical chemistry letters* 6.9 (2015): 1645-1652.
2. Wang, Yonggang, et al. "Nano active materials for lithium-ion batteries." *Nanoscale* 2.8 (2010): 1294-1305.
3. Wang, Yonggang, et al. "Nano active materials for lithium-ion batteries." *Nanoscale* 2.8 (2010): 1294-1305.
4. Li, Yan, et al. "An electrochemically neutralized energy-assisted low-cost acid-alkaline electrolyzer for energy-saving electrolysis hydrogen generation." *Journal of Materials Chemistry A* 6.12 (2018): 4948-4954.
5. Roy, Atanu, et al. "Investigation on energy storage and conversion properties of multifunctional PANI-MWCNT composite." *International Journal of Hydrogen Energy* 43.14 (2018): 7128-7139.
6. Wu, Y. Z., et al. "Hydrothermal synthesis of Fe3O4 nanorods/graphitic C3N4 composite with enhanced supercapacitive performance." *Materials Letters* 198 (2017): 114-117.
7. Dawson, James A., Theodosios Famprikis, and Karen E. Johnston. "Anti-perovskites for solid-state batteries: recent developments, current challenges and future prospects." *Journal of Materials Chemistry A* 9.35 (2021): 18746-18772.
8. Wang, Yan, et al. "Supercapacitor devices based on graphene materials." *The Journal of Physical Chemistry C* 113.30 (2009): 13103-13107.
9. Kumar, Ramesh, and Monojit Bag. "Hybrid Halide Perovskite-Based Electrochemical Supercapacitors: Recent Progress and Perspective." *Energy Technology* 10.3 (2022): 2100889.
10. Popoola, Idris, et al. "Fabrication of organometallic halide perovskite electrochemical supercapacitors utilizing quasi-solid-state electrolytes for energy storage devices." *Electrochimica Acta* 332 (2020): 135536.
11. Maji, Prasenjit, et al. "Fabrication of symmetric supercapacitor using cesium lead iodide (CsPbI3) microwire." *Materials Letters* 227 (2018): 268-271.
12. Pious, Johnpaul K., et al. "Zero-dimensional methylammonium bismuth iodide-based lead-free perovskite capacitor." *ACS omega* 2.9 (2017): 5798-5802.
13. Li, Tianyue, et al. "Thiourea bismuth iodide: crystal structure, characterization and high performance as an electrode material for supercapacitors." *Batteries & Supercaps* 2.6 (2019): 568-575.
14. Ding, Rui, et al. "Perovskite KNi 0.8 Co 0.2 F 3 nanocrystals for supercapacitors." *Journal of Materials Chemistry A* 5.34 (2017): 17822-17827.

15. Fu, Huiying. "Review of lead-free halide perovskites as light-absorbers for photovoltaic applications: from materials to solar cells." *Solar Energy Materials and Solar Cells* 193 (2019): 107-132.
16. Van Le, Quyet, Ho Won Jang, and Soo Young Kim. "Recent advances toward high-efficiency halide perovskite light-emitting diodes: review and perspective." *Small Methods* 2.10 (2018): 1700419.
17. Jin, Wei, and Govindhan Maduraiveeran. "Recent advances of porous transition metal-based nanomaterials for electrochemical energy conversion and storage applications." *Materials Today Energy* 13 (2019): 64-84.
18. Ding, Jijun, Xingbin Yan, and Qunji Xue. "Study on field emission and photoluminescence properties of ZnO/graphene hybrids grown on Si substrates." *Materials Chemistry and Physics* 133.1 (2012): 405-409.
19. Chen, Yan-Li, et al. "Zinc oxide/reduced graphene oxide composites and electrochemical capacitance enhanced by homogeneous incorporation of reduced graphene oxide sheets in zinc oxide matrix." *The Journal of Physical Chemistry C* 115.5 (2011): 2563-2571.
20. Sreeja, V. G., et al. "Structural, Spectral, Electrical and Nonlinear Optical Characterizations of rGO-PANI Composites." *Materials Today: Proceedings* 10 (2019): 456-465.
21. Yan, Huangping, et al. "The effect of rGO-doping on the performance of SnO2/rGO flexible humidity sensor." *Nanomaterials* 11.12 (2021): 3368.
22. Zhou, Jisheng, et al. "Magnetite/graphene nanosheet composites: interfacial interaction and its impact on the durable high-rate performance in lithium-ion batteries." *Rsc Advances* 1.5 (2011): 782-791.
23. Sasmal, Ananta, and Arpan Kumar Nayak. "Morphology-dependent solvothermal synthesis of spinel NiCo2O4 nanostructures for enhanced energy storage device application." *Journal of Energy Storage* 58 (2023): 106342.
24. Kumar, Ramesh, and Monojit Bag. "Quantifying capacitive and diffusion-controlled charge storage from 3D bulk to 2D layered halide perovskite-based porous electrodes for efficient supercapacitor applications." *The Journal of Physical Chemistry C* 125.31 (2021): 16946-16954.
25. Saseendran, Swathy B., Anamika Ashok, and A. S. Asha. "Edge terminated and interlayer expanded pristine MoS2 nanostructures with 1T on 2H phase, for enhanced hydrogen evolution reaction." *International Journal of Hydrogen Energy* 47.16 (2022): 9579-9592..

Photocatalytic Degradation of Methyl Orange by Electrochemically Synthesized TiO_2 Nanotubes

Hiba Rahman[1,2], Rachel Reena Philip[1*]

[1]*Thin Film Research Lab, Department of Physics, Union Christian College, Aluva, Kerala, India*

[1]*Department of Physics, Al Ameen College, Edathala, Aluva, India*

**reenatara@gmail.com*

Abstract. Titanium dioxide is being extensively used in many environmental applications due to its antibacterial properties and high performance in degradation of various dyes. In this study we report the synthesis and photocatalytic activity of anatase TiO_2 nanotubes prepared by electrochemical anodization. The prepared samples exhibit a band gap of 3.0eV. The compositional analysis using EDAX confirms the formation of anatase TiO_2. The structural and morphological characterizations are done using X-ray Diffraction, Field Emission Scanning Microscopy and Atomic Force Microscopy. The FESEM and AFM analyses confirm the formation of well aligned array of TiO_2 nanotubes which are appreciably interconnected. These interconnected array of nanotubes increase the surface area and provide more adsorption sites that contribute to the high dye degradation rates in comparison with the TiO_2 nanostructures in literature. The prepared samples are able to degrade 82.2% of methyl orange in 180 minutes under solar radiation.

Keywords: TiO_2, electrochemical anodization, photocatalysis.

1 Introduction

In recent years, water pollution caused by various industries has become a serious threat to human as well as aquatic life. TiO_2 has attracted researchers over decades due to its low cost, chemical stability and effectiveness in environmental remediation [1–4]. TiO_2 exists in three different crystalline phases as anatase, brookite and rutile. Among these anatase phase is extensively investigated due to its excellent photocatalytic activity [5–7].

Generally, electron-hole pairs are generated when TiO_2 is exposed to a radiation of energy higher than its band gap. The valence band holes and

conduction band electrons are capable of producing hydroxyl radicals which oxidise chemical pollutants [6,8]. The photocatalytic activity of a material is influenced by several factors like crystalline phase, crystallite size, surface area and impurity contents [2,9]. Anatase TiO_2 with indirect band gap is found to have a longer life time for electrons and holes [10]. The photocatalytic degradation efficiency of anatase TiO_2 is highly dependent on the surface area as it provides adsorption sites. TiO_2 nanostructures can be synthesized in different shapes as sheets, rods, tubes and wires [11,12]. Among these TiO_2 nanostructues, nanotubes when employed for photocatalysis can bring about higher dye degradation due to its increased surface area by providing more active sites for surface reactions [13].

Here we are reporting structural, optical and morphological properties of TiO_2 nanotubes (TONT) prepared by electrochemical anodization and the photocatalytic efficiency of TONT on degrading the chemical dye methyl orange under solar radiation.

2 Experimental

Electrochemical anodization technique is employed for the synthesis of TiO_2 nanotubes. The electrolyte is composed of ethylene glycol with 0.5 wt% ammonium fluoride and 2 vol% of distilled water. Pure Ti foils are used for both electrodes. Anodization is performed for 30 min at 50V. The setup is kept in water bath maintained at room temperature($29^{O}C$). The synthesized TONTs are sonicated in distilled water and dried to remove any nanograss formed on the surface. The samples are annealed for 2 hours at 450°C.

The samples are analyzed using Bruker D8 Advance X-ray Diffractometer to obtain the structure and phase. The surface morphology of the samples is studied by Bruker made Bio-AFM (Bioscope resolve) (RV) and FESEM (Carl Zeiss Sigma field emission scanning microscope). Optical studies are done using diffuse reflectance spectrometer [UV-Vis (Flame TUV XR1 ES) and VIS (Flame NIR)]. The composition of the samples are analysed using EDAX (Jeol 6390LA/OXFORD XMX N. Methyl Orange (MO) dye in aqueous solution is used to test the photocatalytic degradation efficiency of the samples. The samples are immersed in the dye solution and kept under solar radiation. The absorbance of the MO samples are measured using Shimadzu UV-1900i UV-Vis Spectrophotometer at regular intervals of 30, 60, 90, 120, and 180 min.

3 Results and Discussions

The X-ray diffraction (XRD) pattern of TONT sample prepared by anodization is depicted in Fig. 1. The obtained peak pattern matches well with anatase TiO_2 of QualX file 00-021-1272. The most intense reflection occurs from (101) plane at 25.28°. Reflection from the planes (004), (200), (105) and (211) contributes the other prominent peaks.

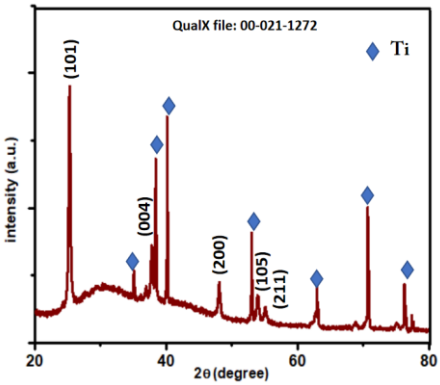

Fig. 1. XRD pattern of TONT

The Debye Scherrer formula [14] is used to calculate the crystallite size (D).

$$D = \frac{0.9\lambda}{\beta Cos\theta} \quad (1)$$

where λ is the wavelength of the irradiating source, β is the FWHM of selected peak and θ the corresponding Bragg's angle. The size of the TONT crystallites are obtained as ~20 nm.

The lattice parameters for tetragonal crystal structure is calculated using the equation

$$\frac{1}{d_{hkl}^2} = \frac{h^2+k^2}{a^2} + \frac{l^2}{c^2} \quad (2)$$

and are obtained as a= (3.787±0.002) Å and c= (9.512±0.001) Å. These values agree with the reported values for anatase TiO_2 [7,15].

The surface morphology of the TONT samples are observed using AFM and FESEM imaging techniques. The AFM images (2D and 3D) of the TONT sample depicted in Fig. 2 clearly indicates the nanotube formation on the surface of Ti substrate.

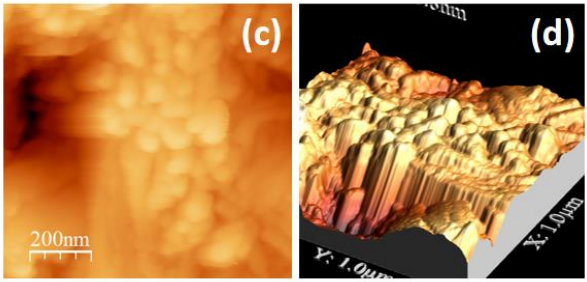

Fig. 2. AFM images of TONT [(a) 2D, (b) 3D].

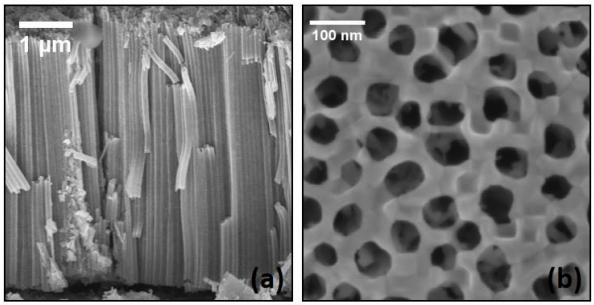

Fig. 3. FESEM images of TONT [(a) cross section, (b) top view].

Fig. 3 shows the cross sectional and top view FESEM images of the TONT samples. The formation of well aligned TiO_2 nanotubes with length ~4.74 µm is confirmed from the image. The pore diameter is obtained as ~56.8 nm and the tube wall thickness is ~35.6 nm. The top view indicates that the nanotubes are interconnected at the top. This interconnected network can lead to increased surface area which in turn provides more adsorption sites when employed for photocatalytic applications.

EDAX analysis is done to assess the composition of component elements of the specimen. Fig. 4 shows the EDAX spectrum of the TONT sample. The

prepared sample consists of oxygen ~65.4 atomic% and titanium ~34.6 atomic % confirming the stoichiometry of TiO_2.

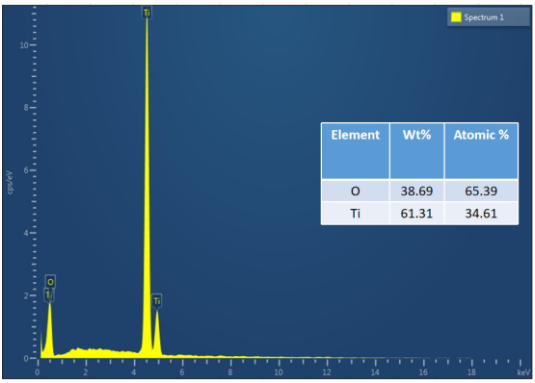

Fig. 4. EDAX spectrum of TONT.

The optical property of TONT is analysed using Diffuse Reflectance Spectrum. The band gap of the sample is evaluated using the Kubelka-Munk function [8]

$$F(R) = \frac{(1-R)^2}{2}R \qquad (3)$$

where R is the reflectance of the sample. From the plot of $(F(R)h\nu)^{1/2}$ versus $h\upsilon$, the indirect band gap of the prepared sample is evaluated and is shown in Fig. 5. The band gap of TONT is obtained as 3.0eV, in agreement with the reports on anatase TiO_2.

The photocatalytic activity of TONT is analysed by studying its degradation efficiency on methyl orange dye under solar radiation. The sample is immersed in the aqueous solution of dye and kept under sunlight for specific time intervals of 30, 60, 90, 120, and 180 min. Fig. 6 (a) shows the variation in absorbance of light by methyl orange in different time intervals. The absorbance value is found to decrease with the increase in irradiating time. As per Beer-Lambert law, this decrease in absorbance can be correlated to the decrease in concentration of the dye solution. The degradation efficiency is estimated with the equation(4)

$$\frac{C_0 - C}{C_0} \times 100 \quad (4)$$

where C_0 is the concentration of unirradiated dye and C that of the dye after irradiation for the specified time duration.

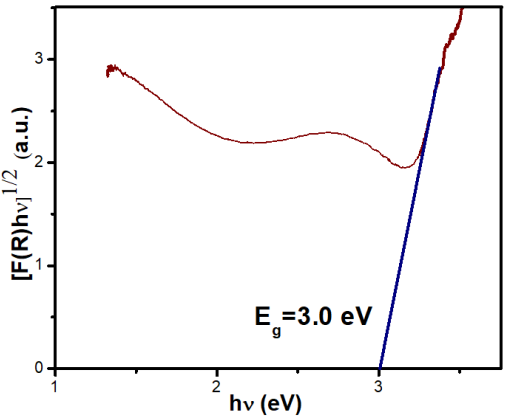

Fig. 5. $(F(R)h\nu)^{1/2}$ versus hν plot of TONT.

Degradation rate of 34% was reported for methylene blue by Nam et al. in 2 hours using titanium dioxide nanotubes [16]. Thandapani et al. could attain 81.5% degradation of methyl orange in 6 hours using TiO_2 nanoparticles under sunlight irradiation [17]. Here we could attain degradation of methyl orange at a much faster rate due to the enhanced surface area provided by the nanotubular structure. Fig. 6 (b) depicts the percentage of degradation versus irradiation time. The prepared TONT sample is found to degrade 82.2% of methyl orange dye in 180 minutes solar irradiation.

The mechanism of degradation of organic dye in water by TiO_2 nanotubes is better discussed as follows. Upon irradiating the sample with a photon of energy equal to or greater than the band gap of TiO_2, the photons will get absorbed leading to the excitation of valence band electrons to the conduction band. As a result, holes are formed in the valence band which interact with the water molecules to create hydroxyl radicals and hydrogen ions whereas the electrons from conduction band react with oxygen yielding superoxide radicals. The hydrogen ions react with the superoxide radicals forming

hydrogen peroxide which in turn reacts with conduction band electrons and produce hydroxyl radicals. These powerful hydroxyl radicals reacts with the dye pollutant adsorbed on the nanotube surface and degrade it to nontoxic by products [5,18]. Here, the increased surface area contributes to the increased rate of dye degradation by providing more adsorption sites for the dye molecules, causing enhanced interaction rate between the dye molecules and hydroxyl radicals.

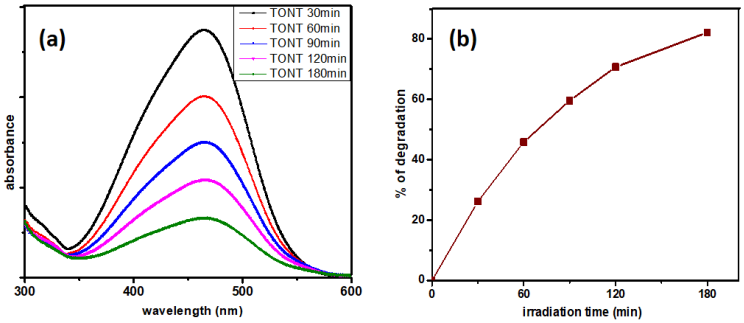

Fig. 6. (a) absorbance Vs wavelength plot for TONT [at time intervals 30, 60, 90, 120, and 180 min], (b) degradation rate of MO.

4 Conclusion

In this study, titanium dioxide nanotubes prepared using the method of electrochemical anodization are structurally, compositionally, morphologically characterized before using them for photocatalytic application. The anatase phase with (101) orientation is confirmed for the samples. TONTs are found to have band gap of 3.0eV and well aligned nanotubular structure. The high photocatalytic degradation rate over the dye MO under sunlight suggest application of TONTs in optoelectronic materials and devices for environmental sustainability.

Acknowledgments

The authors acknowledge DST-SERB for funding through a major research project (Ref. No. CRG/2020/000448). The authors thank Dr. Shinoj V.K (

Physics department, UCC) and Mr. Mohan Gangrade (UGC-DAE CSR, Indore) for DRS and AFM measurements respectively.

References

1. Song E, Kim Y T and Choi J 2019 Anion additives in rapid breakdown anodization for nonmetal-doped TiO2 nanotube powders *Electrochem. commun.* **109** 106610
2. Hoffmann M R, Martin S T, Choi W and Bahnemann D W 1995 Environmental Applications of Semiconductor Photocatalysis *Chem. Rev.* **95** 69–96
3. Singh J, Kumar S, Rishikesh, Manna A K and Soni R K 2020 Fabrication of ZnO–TiO2 nanohybrids for rapid sunlight driven photodegradation of textile dyes and antibiotic residue molecules *Opt. Mater. (Amst).* **107** 110138
4. De Los Santos D M, Aguilar T, Sánchez-Coronilla A, Navas J, Cruz Hernández N, Alcántara R, Fernández-Lorenzo C and Martín-Calleja J 2014 Electronic and structural properties of highly aluminum ion doped TiO 2 nanoparticles: A combined experimental and theoretical study *ChemPhysChem* **15** 2267–80
5. Zhang J, Tian B, Wang L, Xing M and Lei J 2018 Mechanism of Photocatalysis 1–15
6. Nunes D, Pimentel A, Santos L, Barquinha P, Fortunato E and Martins R 2017 Photocatalytic TiO2 nanorod spheres and arrays compatible with flexible applications *Catalysts* **7**
7. Gupta S M and Tripathi M 2011 A review of TiO2 nanoparticles *Chinese Sci. Bull.* **56** 1639–57
8. Joseph J A, Nair S B, John K A, Babu S, Shaji S, Shinoj V K and Philip R R 2020 Aluminium doping in iron oxide nanoporous structures to tailor material properties for photocatalytic applications *J. Appl. Electrochem.* **50** 81–92
9. Harikishore M, Sandhyarani M, Venkateswarlu K, Nellaippan T A and Rameshbabu N 2014 Effect of Ag Doping on Antibacterial and Photocatalytic Activity of Nanocrystalline TiO 2 *Procedia Mater. Sci.* **6** 557–66
10. Chen D, Cheng Y, Zhou N, Chen P, Wang Y, Li K, Huo S, Cheng P, Peng P, Zhang R, Wang L, Liu H, Liu Y and Ruan R 2020 Photocatalytic degradation of organic pollutants using TiO2-based photocatalysts: A review *J. Clean. Prod.* **268** 121725
11. Shalini S, Balasundaraprabhu R, Satish Kumar T, Muthukumarasamy N, Prasanna S, Sivakumaran K and Kannan M D 2018 Enhanced performance of sodium doped TiO2 nanorods based dye sensitized solar cells sensitized with extract from petals of Hibiscus sabdariffa (Roselle) *Mater. Lett.* **221** 192–5
12. Ma D, Xin Y, Gao M and Wu J 2014 Fabrication and photocatalytic properties of cationic and anionic S-doped TiO2 nanofibers by electrospinning *Appl. Catal. B Environ.* **147** 49–57
13. Nair S B, K A john, Menon S S, Rahman H, Joseph J A, Shaji S and Philip R R 2019 Influence of electrochemical reduction of selfdoping on the low temperature

crystallization and photocatalytic activities of TiO 2 nanotubes *Semicond. Sci. Technol.* **34** 095023
14. Priyanka K P, Revathy V R, Rosmin P, Thrivedu B, Elsa K M, Nimmymol J, Balakrishna K M and Varghese T 2016 Influence of la doping on structural and optical properties of TiO2 nanocrystals *Mater. Charact.* **113** 144–51
15. Zhang H and Banfield J F 2014 Structural characteristics and mechanical and thermodynamic properties of nanocrystalline TiO2 *Chem. Rev.* **114** 9613–44
16. Nam C T, Yang W D and Duc L M 2013 Study on photocatalysis of TiO2 nanotubes prepared by methanol-thermal synthesis at low temperature *Bull. Mater. Sci.* **36** 779–88
17. Thandapani K, Kathiravan M, Namasivayam E, Padiksan I A, Natesan G, Tiwari M, Giovanni B and Perumal V 2018 Enhanced larvicidal, antibacterial, and photocatalytic efficacy of TiO2 nanohybrids green synthesized using the aqueous leaf extract of Parthenium hysterophorus *Environ. Sci. Pollut. Res.* **25** 10328–39
18. Sakar M, Mithun Prakash R and Trong-On D 2019 Insights into the tio2-based photocatalytic systems and their mechanisms *Catalysts* **9** 1–30

The effect of voltage in the synthesis of manganese incorporated TiO_2 nanotubes

Priya S. Nair[1,2], Rachel Reena Philip[1*]
[1]*Thin Film Research Lab, Department of Physics, Union Christian College, Aluva-683102*
[2]*Sree Narayana Mangalam College, Maliankara – 683516*
**reenatara@gmail.com*

Abstract. The study reports a comparison of effect of voltage on the successful incorporation of Manganese in TiO_2 nanotubes and the variation it produces in the material properties. The doping method adopted here is a simple electrochemical process in which a voltage applied between the electrodes enables Mn ions from the solution to diffuse into the pure TiO_2 lattice that serves as the negative electrode. The structural, optical, compositional and morphological difference in the Mn incorporated nanotubes at two different voltages 5V and 30V are reported here. XRD depicts peaks of anatase phase for both whereas, the optical reflectance analysis shows a band gap energy of ~2.84eV for 5V doping and two band gaps of 1.32 eV and 2.87eV for 30V doped. The band gaps are lower than the typical band gap of 3.2eV reported for pure anatase TiO_2. The EDAX analysis confirms the presence of Mn in the TiO_2 lattice with an atomic % of 0.46 and 6.65 for those doped at 5V and 30v respectively. The tube diameter from FESEM image is found to be ~70nm in the 5V doped whereas, a layer possibly MnO_2 is formed on the top surface of 30V TiO_2 nanotubes. The reduction in band gaps to visible region in the doped is found to enhance the photocatalytic property of the nanotubes.

Keywords: TiO_2 nanotubes, Mn doping, Photocatalysis.

1 Introduction

Metal oxide nanostructures are potential candidates for environmental applications especially for waste water treatment [1]. Metal oxide nanostructures like ZnO, TiO_2, MnO_2 etc are gaining attention recently for their suitability in waste water treatment[2]. The properties of this material change when the size is reduced to nanoscale and this attracts the interest of researchers nowadays to the study of various properties and applications of modified metal oxide nanostructures. Photocatalysis is one method which is used to solve environmental issues, in particularly waste water treatment[3].

With the increase in the pollution rate, it is necessary to develop various technologies which are inexpensive and non-toxic to treat waste waters.

TiO_2 is a widely used photocatalyst due to its non-toxicity, availability, cost effectiveness and long-term stability [3]. The challenge in using TiO_2 is that it has a wide band gap of 3.2eV which allows absorption only in the UV region [4,5]. Since sunlight consists of visible light in larger percentage (approximately 42%), it is useful if we can bring down the band gap of TiO_2 so that it allows absorption in visible region. Doping with metal ions is an effective way to alter the band gap to the visible range of solar spectrum [6–8]. Another method is by modifying the morphology of this nanostructures therby improving the photocatalytic performance [9]. Mn is one of the suitable ions which can lower the band gap energy so that photon absorption in the entire visible region of the solar spectrum is made possible[10,11].

In the present study we have incorporated Mn in TiO_2 lattice with a simple and cost-effective process of anodisation followed by an electrochemical process of doping with metal ions by the application of two different potentials 5V and 30 V. In addition to that, the influence of voltage on the successful incorporation of Mn in TiO_2 lattice and their resultant photocatalytic performance are studied.

2 Experimental

Mn incorporated TiO_2 nanotubes are synthesised by a two-step process. The pure TNTs are produced by an electrochemical anodisation process in which Ti foil is taken as the cathode as well as anode and an electrolyte of ethylene glycol containing 0.5 wt%NH_4F and 2 Vol% H_2O is used. The process is done for 30 minutes with the application of 50V. The resultant TiO_2 nanotubes formed on the Ti foil that is taken as the anode, is then thorughly sonicated to remove nanograss formed on the surface[12,13].In the second step,the prepared TiO_2 nanotube is given a negative potential and the Ti foil is given a positive potential. A solution containing 0.5 M $MnSO_4$ solution with water is taken as the electrolyte .Here doping is carried out for two different voltages ie 5V and 30V so as to yeild two samples namely TNT5 and TNT30. The doping time is 5s. The prepared samples are subjected to acid treatment (1M HCl for 30minutes) which is followed by washing with distilled water,drying in mild hot air and annealing at 450 ^oC for 2 hours.

The structural analysis is done using XRD (PANALYTICAL, Aeris Research) with Cu Kα source and Thermo Scientific DXR Raman spectrometer is used to obtain Raman spectra. A carl Zeiss Sigma Field Emission Scanning Electron Microscope is used to obtain FESEM images.The compositional analysis is done using Energy X ray dispersive spectrometer QUANTAX 200 with X-Flash ® 6 I 100 .The optical analysis is done using a UV Visible (Flame TUV XR1 ES) and NIR(Flame NIR) based diffuse reflectance spectrophotometer. The dye used to study the photocatalytic degradation of the as prepared sample is Rhodomine B (Rh B) and the experiment is done under solar irradiation. The degradation efficiency is measured using a UV Visible spectrophotometer Shimadzu UV-3600.

3 Results and Discussions

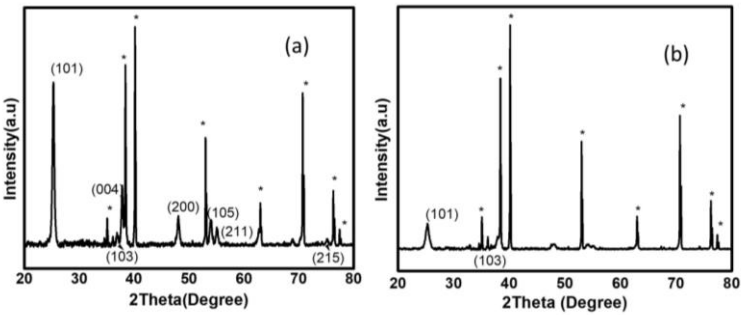

Fig. 1. X Ray diffraction image of (a)TNT5 and (b)TNT30

Fig 1(a)and (b)depicts the X ray diffraction image of TNT5 and TNT 30. Both samples are identified as TiO_2 anatase phase with the qualax card number 00-021-1272[12–14]. It is noted that peaks corresponding to planes (101),(004).(103),(200),(105),(211) and (215) are identified for TNT5 whereas planes (101) and (103) are identified for TNT30.The peak corresponding to(101) plane which shows a preferential orientation for TNT5 exhibits a diminishing intensity for TNT 30 as the voltage is increased. . The crystallite sizes (d)can be found out from Debye Scherrer equation as

$$d = \frac{0.9\lambda}{\beta cos\theta} \quad (1)$$

where λ is the wavelength of Cuk-alpha, β is the selected peak's FWHM in radians and θ the corresponding angle. The crystallite size is found to be ~22 nm for TNT5 and it increases to ~82 nm for TNT30.

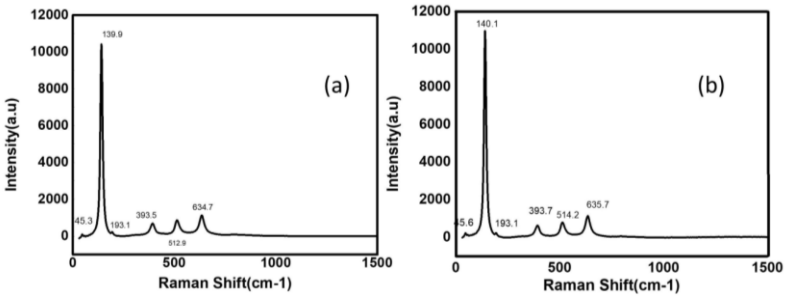

Fig. 2. Raman Spectra of (a) TNT5 (b) TNT30

Figure 2 (a) and (b) shows Raman spectra of TNT5 and TNT30. The Raman spectra of anatase TiO_2 belongs to the phase group D_{4h} . It usually consist of vibrational bands at 144 (Eg), 197 (Eg), 399 (B1g), 519 (A1g + B1g), and 639 cm−1 (Eg)[15]. In the TNT 5 sample distinguishable peaks are found at 139.9 cm^{-1}, 393.5 cm^{-1}, 512.9 cm^{-1},634.7cm^{-1} which matches with the usual peaks with slight change in frequency whereas TNT30 sample consists of distinguishable peaks at 140.1 cm^{-1},393.7cm^{-1}, 514.2 cm^{-1},635.7cm^{-1} which also matches with the usual peaks. The peak around 144 is the characteristic peak of anatase TiO2[16].A peak of low intensity is observed at 193.1 cm^{-1} for both TNT5 and TNT30 which is the Eg mode and matches with the usual peak at 197cm^{-1} with slight change in frequency. It is also noted that doping at a higher voltage cause a frequency shift keeping the intensity almost a constant.

The presence of Ti, O and Mn are confirmed from compositional analysis done by EDAX. The result is shown in Fig 2(a) and (b). The percentage compositions of various elements are shown in table 1.The sample contains a larger percentage of oxygen for both the samples than Ti. The increase in voltage increases the percentage of Mn present in the sample TNT30 from 0.46% to 6.65%. In addition to this traces of sulphur is identified in TNT30 which may be from the precursor $MnSO_4$.

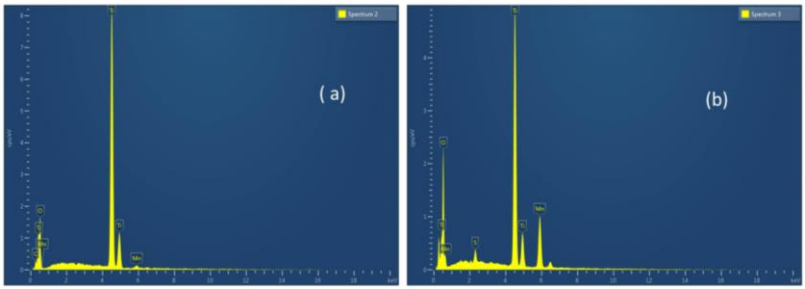

Fig. 3. EDX spectra of (c) TNT5 and (d)TNT30

Table 1. Percentage of composition of elements in TNT5 and TNT30

TNT5		TNT30	
Element	Atomic %	Element	Atomic %
C	6.67	O	71.46
O	61.64	S	0.65
Ti	31.23	Ti	21.24
Mn	0.46	Mn	6.65
Total:	100	Total:	100

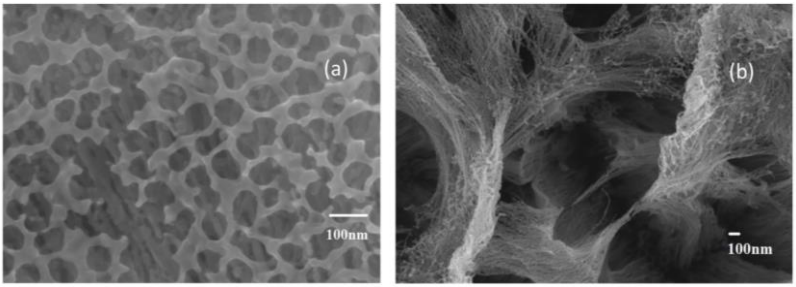

Fig. 4. FESEM images of (g)TNT 5 and (h)TNT30

The top view of TNT5 and TNT30 are shown in the Fig.4(a) and (b). The image of TNT5 shows tube like structures which are broken in between. The average tube diameter is found to be 70nm. FESEM image of TNT30 indicates a porous layer on top which blocks the view of the nanotubes below. This may be the MnO_2 layer which we can confirm from the plot of $((F(R)hv)^{1/2}$ Vs hv.[17]

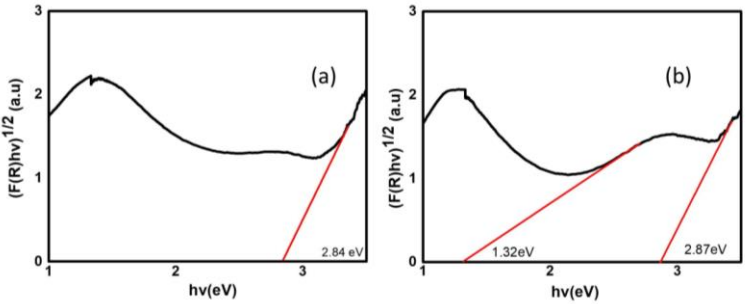

Fig. 5. Plot of ((F(R)hv)1/2 Vs hv of (a) TNT5 and (b)TNT30.

The band gap of the prepared samples are calculated by measuring the reflectance with respect to wavelength which is then used to plot $[F(R)\ hv]^{1/2}$ versus hv (shown in Fig 5(a) and (b)) where F(R) is the Kubelka munk funcion and hv is the corresponding energy value. From the graph the indirect band gap energy corresponding to TNT5 is found to be 2.84eV and that for TNT30 is found to be 1.32eV and 2.87eV [18,19]. Here Mn doping has caused a reduction in band gap to 2.84 eV which indicates the incorporation of Mn into TiO_2 lattice.In the case of TNT30 two band gaps are observed one indicating the presence of Mn incorporation into the sample whereas a second band gap corresponds to the band gap of MnO_2 layer. This suggests the formation of MnO_2 layer on the top of TiO_2 nanotubes [17]. The presence of an overlayer can be confirmed from the FESEM image of the sample.

In order to study the photocatalytic activity of the sample, Rhodamine B dye is used. The samples TNT5and TNT30 are immersed in 10ml of the dye solution under direct sunlight. The percentage of dye degradation is recorded at 0 ,30,60,120 and 180 minutes respectively. The absorption of TNT5 amd TNT30 are shown as in Fig 6(a) and (b) respectively. A reduction in the intensity of the absorption peak of the dye for various time intervals becomes evident indicating the photocatalytic action of both the samples. Percentage of degradation Vs irradiation time is shown as in Fig 6(c). TNT5 is found to have a degradation of 98.44% and that of TNT30 of 96.18%. The cycle stability of the sample is estimated by keeping the sample for 4 successive days in sunlight for 3 hours which is shown in Fig 6(d). Even though the percentage of degradation is almost comparable for both the samples, it is found that TNT5 is showing more stability than TNT30. It is also noted that the increase in

voltage forms a MnO_2 layer on the top of the nanotubes which contributes a second band gap. But this doesn't contribute to the improvement of photocatalytic action of the sample whose Mn incorporation is done at 30V instead reduces the photocatalytic stability. It is already reported by us that Mn doping at 20V forms a MnO_2 layer which results in better photocatalytic performance and with good cycle stability [17]. In contrary to this, the application of 30V reduces the photocataytic performance of TNT 30.

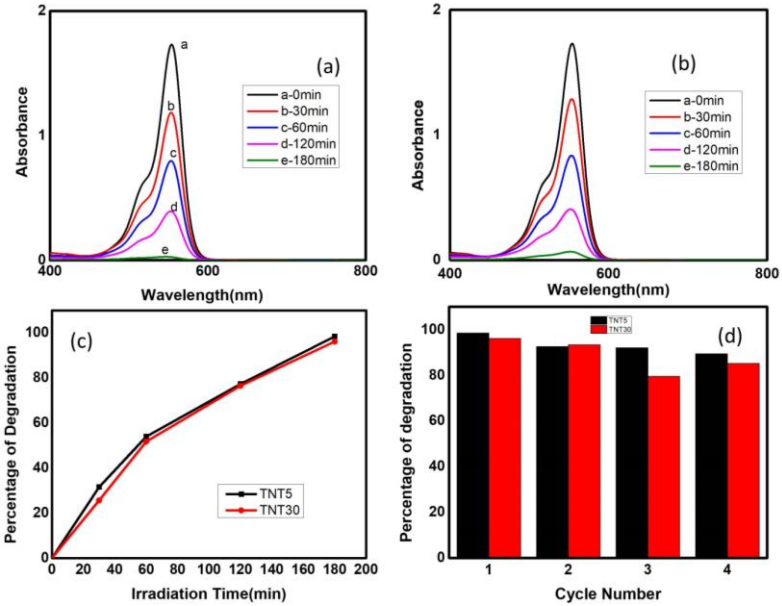

Fig. 6. Absorbance spectra of the dye showing the degradation of Rhodomine Dye by (a) TNT5 and (b)TNT30 and Percentage of degradation Vs Irradiation time(c) and Cycle stability (d) for TNT5 and TNT30

4 Conclusion

The present work reports the effect of voltage on the synthesis and photocatalytic performance of Mn doped samples in the degradation of Rh B. We successfully incorporated Mn into TiO_2 nanotubes by the application of 5V and 30V. Structural, optical, compositional and morphological studies are done on both the samples. It is observed that Mn incorporation has successfully

lowered the band gap.The application of 30V has formed an MnO_2 layer on the top of the nanotubes which slightly increases photocatalytic degradation efficiency but,compromising cyclic stability when compared to TNT5. Therfore TNT5 is a better photocatalyst with a stable performance than TNT30.

Acknowledgments

The authors thank DST for sanctionin a major research project (Ref. No. CRG/2020/000448). The corresponding and first author acknowledge,Dr. Shinoj V.K for reflectance measurements.

References

1. Y. Yang, C. Zhang, and Z. Hu, Environ. Sci. Process. Impacts **15**, 39 (2013).
2. T. Naseem and T. Durrani, Environ. Chem. Ecotoxicol. **3**, 59 (2021).
3. C. W. Lai, J. C. Juan, W. B. Ko, and S. Bee Abd Hamid, Int. J. Photoenergy **2014**, (2014).
4. M. M. Momeni, M. Hakimian, and A. Kazempour, Surf. Eng. **32**, 514 (2016).
5. S. M. Gupta and M. Tripathi, Chinese Sci. Bull. **56**, 1639 (2011).
6. M. Sakar, R. Mithun Prakash, and D. Trong-On, Catalysts **9**, (2019).
7. X. Chen and S. S. Mao, Chem. Rev. **107**, 2891 (2007).
8. M. M. Momeni and A. A. Mozafari, J. Mater. Sci. Mater. Electron. **27**, 10658 (2016).
9. K. Nakata and A. Fujishima, J. Photochem. Photobiol. C Photochem. Rev. **13**, 169 (2012).
10. L. Wang, X. Zhang, P. Zhang, Z. Cao, and J. Hu, J. Saudi Chem. Soc. **19**, 595 (2015).
11. Q. R. Deng, X. H. Xia, M. L. Guo, Y. Gao, and G. Shao, Mater. Lett. **65**, 2051 (2011).
12. S. B. Nair, A. Aijo John, J. A. Joseph, S. Babu, V. K. Shinoj, S. K. Remillard, S. Shaji, and R. R. Philip, Nanotechnology **31**, (2020).
13. S. B. Nair, K. Aijo John, H. Rahman, J. A. Joseph, S. K. Remillard, and R. R. Philip, CrystEngComm **21**, 128 (2019).
14. S. B. Nair, A. K. John, S. S. Menon, H. Rahman, J. A. Joseph, S. Shaji, and R. R. Philip, Semicond. Sci. Technol. **34**, (2019).
15. U. Balachandran and N. G. Eror, *Raman Spectra of Titanium Dioxide* (1982).
16. R. P. Antony, A. Dasgupta, S. Mahana, D. Topwal, T. Mathews, and S. Dhara, J. Raman Spectrosc. **46**, 231 (2015).
17. P. S. Nair, H. Rahman, J. A. Joseph, A. Norbert, S. Shaji, S. Tripathi, S. N. Jha, and R. R. Philip, Appl. Phys. A Mater. Sci. Process. **128**, (2022).

18. L. Yao, Electron. Thesis Diss. Repos. **6731**, (2019).
19. B. C. Hodges, E. L. Cates, and J. Kim, Nat. Nanotechnol. **13**, (2018).

Antibacterial property of ZnO nanostructures prepared by Anodization method

Surya Mary A[1], Sareen Sarah John[2], Rachel Reena Philip[1*]

[1] Thin Film Research Lab, Department of Physics, Union Christian College, Aluva, Kerala, India, PIN-683102

2 Department of Biosciences, Union Christian College, Aluva, Kerala, India, PIN-683102

*reenatara@gmail.com

Abstract. Present work discusses the antibacterial activity of pristine Zinc oxide nanoparticles against gram negative and gram positive bacteria, E. Coli, Pseudomonas, Bacillus and S.aureus. Hexagonal wurtzite ZnO nanostructures are prepared by simple cost-effective electrochemical anodization method and the structure is confirmed by XRD. Using UV-vis diffuse reflectance spectroscopy, the band gap of samples is found to be ~3.12 eV. From FESEM images, formation of clusters of ZnO nanorods is observed. PL depicts the ZnO peaks. The effect of ZnO nanoparticles on the antibacterial efficacy is studied for different concentrations, by well diffusion agar method. Antibacterial results suggest that ZnO can be used as an antibacterial agent towards both gram negative as well as gram positive bacteria but, modifications are needed for better efficiency.

Keywords: Anodization, gram positive, gram negative.

1 Introduction

ZnO is a II-VI compound having a wide band gap ~3.2 eV that falls in the UV region of the solar spectrum [1]. Zinc oxide has attracted considerable attention owing to their promising applications in areas such as electronics, optoelectronics, photovoltaics and sensing. ZnO is also used in biomedical applications and to reduce environmental toxicity since it is biocompatible, decomposable, and biosafe [2]. In nanometer range, the chemical, structural, optical, morphological as well as biological properties of the material are entirely different. Nano-sized particles of ZnO have more pronounced antimicrobial activity because their high surface-to-volume ratio enable better interaction with bacteria [3,4]. Studies have indicated selective toxicity of

these nanoparticles to bacteria while its harmful effect on human cell is very minimum. Studies show that zinc influence the biological metabolism and is an essential element to keep our body healthy. Zinc can be traced in all tissues of human body. Since the size of nano structures and biological tissues come under same scale its effect on tissues will be much more than that of the bulk material of same type. In this regard study on the antibacterial effect of ZnO nanoparticles is of greatest interest. as the mechanism behind the antibacterial activity of ZnO is not fully understood. Upon irradiation with proper light source the ability to generate reactive oxidation species (ROS) which can damage DNA is considered as the main reason behind this property [4-7]. In addition to this, release of Zn ions in to the cellular environment above the desired limit results in cell death [4].

In the present study ZnO nanostructure is prepared by simple, cost-effective electrochemical method of anodization [5] and its antibacterial activity is tested. The particles are well characterized structurally and morphologically by X-ray diffraction and Field emission Scanning electron microscopy. The optical and defect properties are studied using diffuse reflectance spectroscopy and photoluminescence.

2 Experimental

For electrochemical anodization to prepare ZnO nanostructured films, zinc plate -the anode and titanium plate- the cathode is ultrasonically cleaned initially. The electrodes are placed 3 cm apart and are dipped in aqueous solution of 0.1M NaOH. A 12 V DC voltage is applied to the electrodes for 1 hour and the ZnO nanostructures that grow on the anode are dipped in ethanol for 12 hours for removing the nano grass layer formed on the surface. It is then air annealed at 250° C for 1 hour.

Structure of the as prepared samples are analyzed by Bruker D8 Advanced X-ray diffractometer; optical studies are done with UV-Vis and NIR (Flame NIR) based diffuse reflectance spectrometer (DRS). Carl Zeiss Siga field emission scanning electron microscope (FESEM) is used to study the morphology of the prepared samples. Photo luminescence (PL) is recorded using Horiba Scientific FluoroMax-4 spectrofluorometer.

Antibacterial activity of prepared nanostructure is studied for bacillus, S.aureus gram positive and pseudomonas and E coli gram negative bacteria by well diffusion agar method. Deionized water is chosen as the control and to study the effect of concentration of ZnO on antibacterial activity. Three different samples are prepared by varying the amount of ZnO nanoparticles and it is then dispersed in DI for experiment. Prepared solution is then ultrasonicated to get uniform dispersion. Equal amount of solution is taken in each well and the activity is studied after 24-hour incubation at room temperature. By measuring the zone of inhibition, activity of samples against different bacteria is assessed.

3 Results and Discussions

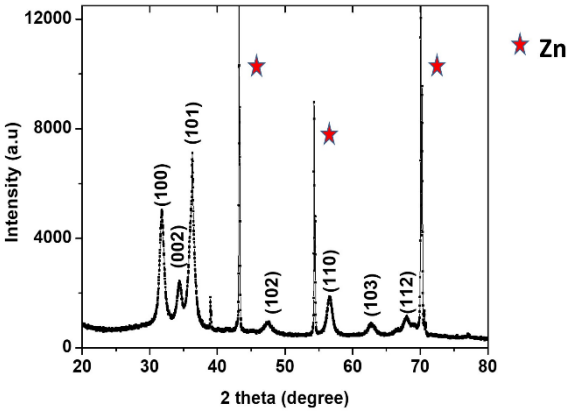

Fig. 1. XRD pattern of ZnO

Figure 1 shows the XRD pattern of ZnO nanostructure. Observed diffraction peaks corresponding to the planes (100), (002), (101), (102), (110), (103), (112) confirm wurzite hexagonal structure for the prepared samples (Qualx card no: 00-036-1451) [8]. For wurzite hexagonal structure lattice parameters a (a=b), c the lattice spacing d and (hkl) planes are related through the equation

$$\frac{1}{d^2} = \frac{4}{3a^2}(h^2 + k^2 + hk) + \frac{l^2}{c^2} \qquad (1)$$

where d is the interplanar distance.

From XRD, d value can be calculated using Braggs equation,

$$n \lambda = 2 d \sin \theta \quad (2)$$

λ is the wavelength of X-ray beam, θ is the Bragg's angle and n is the order of diffraction=1. Lattice parameters are calculated as, a ~ 3.586 A° and c ~ 5.8 A° [8] Crystalline size can be calculated using Scherrer formula

$$D = 0.9\lambda / \beta \cos \theta \quad (3)$$

where D is the average crystallite size, β the full width at half maximum of X-ray diffraction. Crystallite size is calculated using the FWHM for the most intense peak corresponding to the plane (101) and it is obtained as~ 9.6 nm.

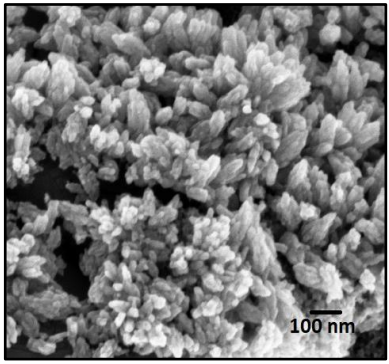

Fig. 2. FESEM image of ZnO

Morphological characteristics of the prepared nanostructure is examined using FESEM image (fig 2). It reveals that ZnO is formed over the Zn plate as vertically aligned clusters of nanorods.

Band gap energy is calculated by analyzing the optical reflectance spectra with the Kubelka-Munk function $F(R) = (1 - R)^2/2R$ Vs hv (fig 3), where hv is the photon energy. Eg,the band gap energy value is determined to be 3.12 eV. Band gap energy of ZnO nanorods can vary in the range of 3.14 to 3.05 eV [9].

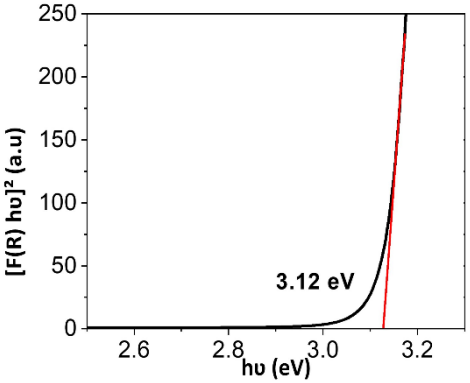

Fig. 3. Tauc plot of ZnO

The room temperature PL emission spectrum of ZnO nanoparticle recorded with excitation wavelength at 360 nm is shown in figure 4. Spectrum shows a high intense peak at 435 nm and a low intense peak at 461 nm, both corresponding to blue emission which may be due to the transition from Zn interstitial to Zinc vacancy [10]. A Low intense peak at 413 nm corresponds to violet emission which is formed when an electronic transition occurs between zinc interstitial level and valence band [11].

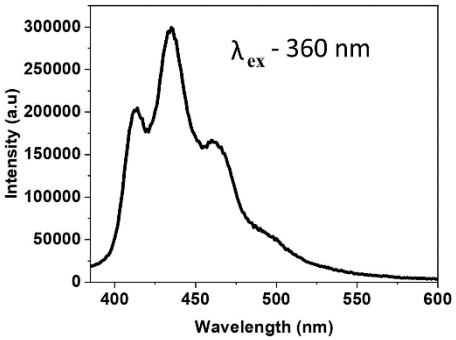

Fig. 4. PL spectrum of ZnO

Disinfectant properties of ZnO nanostructures are investigated against bacillus, S.aureus, pseudomonas and E coli by well diffusion agar method. Figure 5

shows the antibacterial activity of samples with different ZnO concentrations and the results are summarized in table 1. The study shows that only with a higher concentration of 15 mg pure ZnO, activity is observed towards the four bacterial stains which implies that material in higher concentrations is needed for effectiveness against the gram positive and gram negative bacteria. Activity towards S.aureus bacteria is slightly more. Sawai et al [11] also reported such an activity of ZnO nanoparticles towards S.aureus bacteria. The results show that though there is an attraction between ZnO particles and bacterial cells that leads to the death of bacteria, the efficiency is low. This might be due to the fact that here the work is not done under UV irradiation which is required for the production of ROS radicals. The band gap of ZnO being in the UV region, the irradiation is necessary for electron -hole production which can lead to the generation of ROS radicals that play a crucial role in the antimicrobial activity. So, the observations indicate that along with a higher concentration of ZnO, UV irradiation also could be availed for getting better antimicrobial activity with ZnO nanostructures.

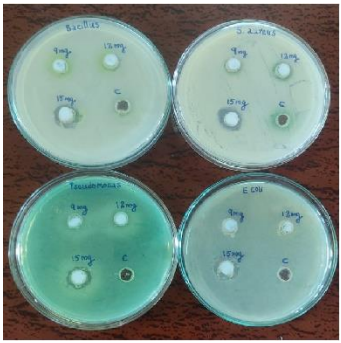

Fig. 5. Antimicrobial activity of ZnO nanoparticles with different concentrations. (C is control)

Table 1. Zone of inhibition (mm) for different bacteria

Concentration of ZnO (mg)	**Zone of inhibition (mm)**			
	Bacillus	***S.aureus***	***Pseudomonas***	***E.coli***
9	No activity	No activity	No activity	No activity
12	No activity	9	No activity	No activity
15	12	13	12	12

4 Conclusion

In the present work ZnO nanostructures are fabricated by low cost and simple anodization method. XRD indicates formation of hexagonal wurtzite ZnO nanostructure for anodized samples and PL spectrum shows the peaks corresponding to blue emission. Morphological image shows that vertically aligned agglomerated nanorods are formed on the anodized Zinc plate. Experimental results endorse anodized zinc oxide as a good candidate for antibacterial studies provided an optimized concentration is used.

Acknowledgments

The authors express gratitude to DST for the funding through the project Ref. No. CRG/2020/000448. Thanks to Dr. Shinoj V.K for reflectance measurements.

References

1. Anshuman Sahai et al, Structural and Vibrational Properties of ZnO Nanoparticles Synthesized by Chemical Precipitation Method. Physica E (58), 130-137 (2014)
2. Getu Kassegn et al, Synthesis method, antibacterial and photocatalytic activity of ZnO nanoparticles for azo dyes in wastewater treatment: A review. Inorganic Chemistry Communications 120, 108140 (2020)
3. Bruna Lallo da Silva et al, Increased antibacterial activity of ZnO nanoparticles: Influence of size and surface modification. Colloids and Surfaces B: Biointerfaces (177), 440–447 (2019)
4. Amna Sirelkhatim et al Review on Zinc Oxide Nanoparticles: Antibacterial Activity and Toxicity Mechanism. Nano-Micro Letters (7), 219–242 (2015)
5. Shalaleh Gilani et al, Antimicrobial Properties of Copper-Doped ZnO Coatings under Darkness and White Light Illumination. ACS Omega (2), 4556−4562 (2017)
6. M. Kaushik et al, Investigations on the antimicrobial activity and wound healing potential of ZnO nanoparticles. Applied Surface Science (479), 1169-1177 (2019)
7. R.K. Dutta et al, Studies on antibacterial activity of ZnO nanoparticles by ROS induced lipid peroxidation. Colloids and Surfaces B: Biointerfaces (94), 143–150 (2012)
8. Surya MaryA et al, Enhanced photocatalytic activity of nZnO/n^{+}Al:Zn homojunction with an overlayer of Al_2O_3 nanoballs. Journal of Physics D: Applied Physics (55), 175108 (2022)
9. Idiawati R et al, Effect of Growth Time on the Characteristics of ZnO Nanorods. IOP Conf. Ser. Mater. Sci. Eng. (202), 012050 (2017)

10. P.V. Athma et al, Nanostructured zinc oxide thin film by simple vapor transport deposition. Superlattices and Microstructures (85), 379-384 (2015).
11. Sawai et al, Quantitative evaluation of antibacterial activities of metallic oxide powders (ZnO, MgO and CaO) by conductimetric assay. J. Microbiol. Methods (54), 177–182 (2003)

Hematite nanoporous material as a promising antibacterial agent

Julie Ann Joseph [1*], Bindu G Nair[1,2] and Rachel Reena Philip[1]
[1] *Thin Film Research Lab, Department of Physics, Union Christian College, Aluva*
[2] *Government Polytechnic College, Perumbavoor*
* julie4sunil@gmail.com

Abstract. In the present work, the effect of hematite nanostructures in inhibiting the growth of two different bacteria is studied. Here, the nanostructures are fabricated by the simple method of electrochemical anodization followed by annealing. The X–ray diffraction studies confirm its formation with rhombohedral structure. Formation of nanoporous structures is confirmed through FESEM images. The optical studies are carried out through diffused reflectance measurements. The XPS studies suggest the presence of iron in Fe^{3+} state, which further confirm the formation of hematite phase. Antibacterial effect of hematite nanostructures is tested by agar well diffusion method. Three different concentrations of the hematite material are utilized and the results show increased antibacterial activity with increase in concentration of material. The results clearly indicate that hematite nanostructures prepared by the simple and cost-effective method can be considered as a promising antibacterial agent against these bacteria.

Keywords: Iron oxide, hematite, anodization, antibacterial agent, agar well diffusion

1 Introduction

Nanotechnology is attracting a wide interest nowadays as it offers a variety of structures in the nanoscale region for application in the fields of catalysis, gas sensing, energy storage, biomedicine etc. The advances in nanotechnology enable preparation of nanostructures, having suitable properties for these applications, with great precision and control. Recently, researchers in the biomedical field has shown particular interest in iron oxide nanostructures due to its unique properties such as abundance, low cost, bio compatibility, non-toxicity, high crystallinity, large surface area and physical and chemical stability [1,2]. Because of these characteristics, iron oxide nanostructures are widely used in drug delivery, magnetic resonance imaging and antibacterial applications [3,4]. The prominent phases of iron oxide such as hematite (α-Fe_2O_3), magnetite (Fe_3O_4) and maghemite (γ-Fe_2O_3) find a large number of

applications in the bio medical field. Hematite (α-Fe_2O_3), the most stable form of iron oxide is commonly considered as a good material in biomedical applications[5–7] . Due to its stable physical, chemical and magnetic properties it is used in targeted drug delivery and biosensing [4,8,9]. Apart from these, recent studies have suggested that the use of hematite as an antibacterial agent is effective.

Here, self-ordered hematite nanoporous structures are prepared by anodization of iron foil followed by annealing [10]. Structural, morphological, optical and compositional characterizations are performed with X-ray diffraction (XRD), Field Emission Scanning Electron Microscopy (FESEM), Diffuse reflectance Spectroscopy (DRS) and X-ray photoelectron Spectroscopy (XPS). In this study, we have also attempted to test the antibacterial efficiency of hematite nanostructures and the effect of increase in concentration of the nanostructures on the antibacterial activity.

2 Experimental

Prior to anodization, the iron foil is polished by silicon carbide papers, then ultrasonically cleaned in acetone and later dried in air. Anodization is carried out using iron foil and titanium foil respectively as anode and cathode in an electrolyte containing 0.7 wt % ammonium fluoride (NH4F) and 2 vol % deionized water in ethylene glycol solution.A potential of 40 V is applied for fifteen minutes. The surface deposited nanograss is removed by ultrasonic cleaning in deionized water for 15 seconds. The anodized samples are annealed at 500°C for 2 hours. XRD (X-ray diffraction) measurements for structural characterization are performed with a Bruker AXS D8 Advance X-ray diffractometer using the Cu kα line with λ=1.54 Å as the source. The morphology of the sample is viewed using a field emission scanning electron microscope (FESEM). Carl Zeiss microscope (Sigma HV series) is used for taking FESEM images. The UV–Visible (Flame TUV XR1 ES) and NIR (Flame NIR) spectrometers-based diffuse reflectance spectroscopy is utilized for optical measurements. The X-ray photo electron spectroscopy(XPS) data for structural and compositional assessment is taken with VSW Scientific Instrument.

For testing the antibacterial activity of iron oxide nanostructures, two bacterial strains are used - *Bacillus suptilis* and *E- coli*. The inoculum of the selected

strains are prepared by growing a single colony for 24 hours in nutrient broth. The prepared nutrient broth with bacterial strains are swabbed on to Muller – Hindar agar plates. The iron oxide nanostructures peeled from the iron foil are mixed with deionized water. To this mixture, 1 vol% HCl is added to form a solution. The antibacterial activity was identified by well diffusion method. To each well, 75 µl of the sample solution are added and kept in incubator at 37°C for 24 hours. Three different concentrations of hematite nanostructures are tested. The presence of inhibition zone measured in millimetre represents the antibacterial activity.

3 Results and Discussions

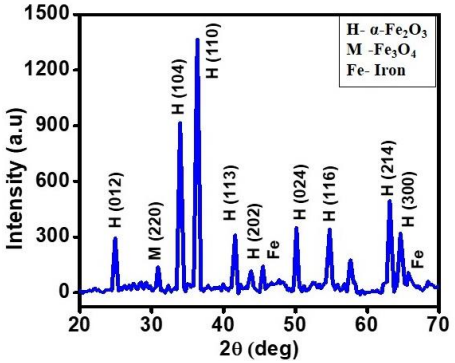

Fig. 1. X Ray profile of Iron oxide nanostructures

The crystal phases of nanostructures are examined by X-ray diffraction (XRD). The XRD profile of annealed sample is shown in Figure 1. The diffraction from (110), (104) and (214) planes are found to be the most intense suggesting the dominance of hematite (α -Fe_2O_3) phase. The other peaks correspond to (012), (113), (024) and (116) planes [11,12]. The lattice parameters deduced confirm a hexagonal crystal structure with a=b = 5.02 Å and c = 13.71 Å, aligning well with the literature values (JCPDS card no. 33-0664). The crystallite size is calculated as ~14.03 nm using the well known Scherrer formula $D= 0.9 \lambda/ \beta \cos \theta$. A small amount of magnetite (Fe_3O_4) is also formed, which has a cubic crystal structure consistent with JCPDS card no 01-1111.

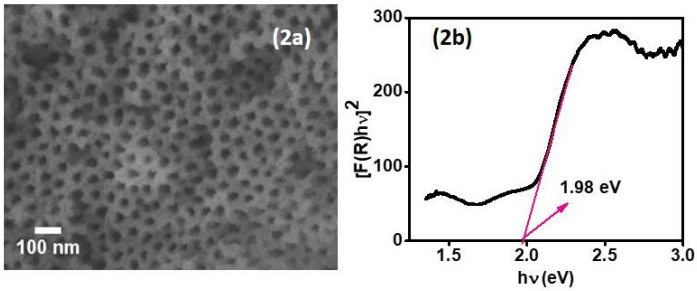

Fig. 2 (a) Image of hematite nanoporous structure (b) Tauc Plot of $[F(R)*h\nu]^2$ vs. hν

Figure 2 The morphological aspects of the hematite samples are examined using FESEM images. The FESEM image (Fig 2a) reveal that ordered nanoporous structure with an average pore diameter of ~ 35nm is formed. The reflectance R measured from DRS is used for determining the band gap with the Kubelka-Munk function, $F(R)=(1-R)^2/2R$ [13] . From the Tauc plot $[F(R)*h\nu]^2$ vs. hν, where hν is the photon energy (Fig 2b), the bandgap (E_g) is determined to be 1.98 eV.

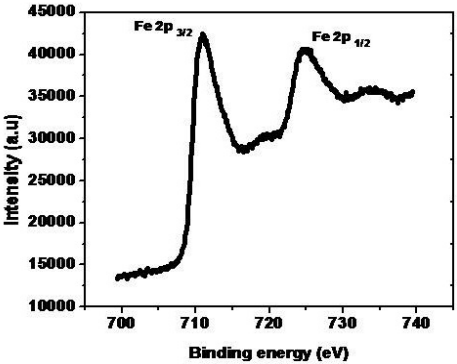

Fig. 3. Fe 2p XPS core spectra

XPS analysis was performed on the samples to verify the compound formation. Presence of iron and oxygen are confirmed from the XPS spectra. Detailed spectra of iron shows the Fe $2p_{3/2}$ and Fe $2p_{1/2}$ peaks (Figure 3). The binding energies obtained for Fe $2p_{3/2}$ and Fe $2p_{1/2}$ in the present study at 711.2 eV and

724.9 eV matches with the reported binding energy positions of Fe $2p_{3/2}$ and Fe $2p_{1/2}$ in hematite [14]. An associated satellite peak is also observed at the B.E position around 8eV higher than that of Fe $2p_{3/2}$ peak B.E, which suggest that iron is in Fe^{3+} oxidation state [15].

The antibacterial activity of hematite nanostructures is tested by agar well diffusion method. *Bacillus subtilis* and *Escherichia coli*, a gram positive and gram negative bacterial strain respectively, are utilized in the study. The activity of the control solution is also tested without adding the hematite nanostructures. The table shows the zone of inhibition measured for iron oxide nanostructures (IONS) for three different concentrations.

Table 1 Zone of Inhibition obtained for two different bacterial strains

Bacterial species	IONS 2.5 mg (in mm)	IONS 5 mg (in mm)	IONS 10 mg (in mm)
Bacillus subtilis	14	18	20
E-Coli	13	17	20

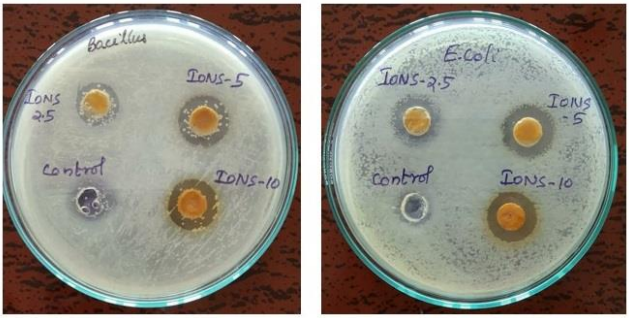

Fig. 4 The antibacterial activity of hematite nanostructures for *Bacillus subtilis* and *Escherichia coli*

As observed from the results, hematite nanostructures are found to be having good activity against both *Bacillus subtilis* and *E-Coli*. It can also be seen that higher antibacterial activity is obtained for higher concentration of the

material. The study clearly suggest that hematite nanostructures can be utilized for biomedical applications since, the oxidative stress generated by reactive oxygen species (ROS) cause DNA and protein damage in bacterial cells. ROS includes singlet oxygen ($^1O_2$), superoxide radical ($O_2^{\cdot-}$), hydroxyl radicals (OH) and hydrogen peroxide (H_2O_2)[16]. The high activity can also be associated with the very small size of the particles that can have more surface atoms which may become active on contact with bacterial cells [17]

4 Conclusion

In summary, hematite nanostructures are fabricated in ethylene glycol based electrolytes by the simple and cost effective method of anodization. Structural, morphological and compositional characterizations are performed to confirm the crystallinity and structure. The study indicates the potential of hematite nanostructures for biomedical applications.

Acknowledgments

The first author acknowledge The Department of Science and Technology (DST), Government of India for funding through Woman Scientist Scheme (Ref : DST /WOS-A /PM-7/ 2017)

References

1. Zhang G-Y, Feng Y, Xu Y-Y, Gao D-Z and Sun Y-Q 2012 Controlled synthesis of mesoporous α-Fe_2O_3 nanorods and visible light photocatalytic property *Mater. Res. Bull.* **47** 625–30
2. Li Y, Feng J, Li H, Wei X, Wang R and Zhou A 2016 Photoelectrochemical splitting of natural seawater with α-Fe_2O_3 /WO_3 nanorod arrays *Int. J. Hydrogen Energy* **41** 4096–105
3. Stephen Inbaraj B, Tsai T Y and Chen B H 2012 Synthesis, characterization and antibacterial activity of superparamagnetic nanoparticles modified with glycol chitosan *Sci. Technol. Adv. Mater.* **13** 015002
4. Sangaiya P and Jayaprakash R 2018 A Review on Iron Oxide Nanoparticles and Their Biomedical Applications *J. Supercond. Nov. Magn.* **31** 3397–413
5. Basnet P, Larsen G K, Jadeja R P, Hung Y C and Zhao Y 2013 α-Fe_2O_3 nanocolumns and nanorods fabricated by electron beam evaporation for visible light photocatalytic and antimicrobial applications *ACS Appl. Mater. Interfaces* **5** 2085–95

6. Rufus A, N. S and Philip D 2016 Synthesis of biogenic hematite (α-Fe_2O_3) nanoparticles for antibacterial and nanofluid applications *RSC Adv.* **6** 94206–17
7. Zhang W, Rittmann B and Chen Y 2011 Size Effects on Adsorption of Hematite Nanoparticles on E. coli cells *Environ. Sci. Technol.* **45** 2172–8
8. Rafi M M, Ahmed K S Z, Nazeer K P, Siva Kumar D and Thamilselvan M 2015 Synthesis, characterization and magnetic properties of hematite (α-Fe_2O_3) nanoparticles on polysaccharide templates and their antibacterial activity *Appl. Nanosci.* **5** 515–
9. Pallela P N V K, Ummey S, Ruddaraju L K, Gadi S, Cherukuri C S L, Barla S and Pammi S V N N 2019 Antibacterial efficacy of green synthesized α-Fe_2O_3 nanoparticles using Sida cordifolia plant extract *Heliyon* **5** e02765
10. Joseph J A, Nair S B, John S S, Remillard S K, Shaji S and Philip R R 2021 Zinc-doped iron oxide nanostructures for enhanced photocatalytic and antimicrobial applications *J. Appl. Electrochem.* **51** 521–38
11. Sarma B, Jurovitzki A L, Smith Y R, Ray R S and Misra M 2014 Influence of annealing temperature on the morphology and the supercapacitance behavior of iron oxide nanotube (Fe-NT) *J. Power Sources* **272** 766–75
12. Zhang Z, Hossain M F and Takahashi T 2010 Fabrication of shape-controlled α-Fe_2O_3 nanostructures by sonoelectrochemical anodization for visible light photocatalytic application *Mater. Lett.* **64** 435–8
13. Joseph J A, Nair S B, John K A, Babu S, Shaji S, Shinoj V K and Philip R R 2020 Aluminium doping in iron oxide nanoporous structures to tailor material properties for photocatalytic applications *J. Appl. Electrochem.* **50** 81–92
14. Grosvenor A P, Kobe B A, Biesinger M C and McIntyre N S 2004 Investigation of multiplet splitting of Fe 2p XPS spectra and bonding in iron compounds *Surf. Interface Anal.* **36** 1564–74
15. McIntyre N S and Zetaruk D G 1977 X-ray photoelectron spectroscopic studies of iron oxides *Anal. Chem.* **49** 1521–9
16. Sies H 1997 Oxidative stress: oxidants and antioxidants *Exp. Physiol.* **82** 291–5
17. Zhang H and Chen G 2009 potent antibacterial activities of Ag/TiO_2 nanocomposite powders synthesized by a one-pot sol-gel method *Environ. Sci. Technol.* **43** 2905–10

Photocatalytic degradation of MB dye: A comparative study between flower like hierarchical structures of MoS_2 and the Bulk MoS_2

Saranya Sasi[1], Christeena Thomas[1], Benazeera Beegum[1], Alex Mathew[1], Reshmi R[1*]

[1]*Optoelectronic and Nanomaterial's Research Laboratory, Department of Physics, Union Christian College, Aluva, Kerala 683102, India*

*rreshmi@gmail.com

Abstract. In the wide library of 2D materials, transition metal dichalcogenides have gained much attention in recent years. Molybdenum disulphide (MoS_2) being a prominent member of this family has been actively researched for the application of photocatalytic degradation of toxic dyes. The narrow band gap, and good optical absorption properties of MoS_2 make itself competent for the widely used photocatalyst Titanium dioxide (TiO_2). In this study flower like nanostructures of MoS_2 were prepared by the versatile hydrothermal technique. The crystallinity of the prepared sample was verified using XRD and Raman. A photocatalytic comparative study was made between bulk MoS_2 and the flower like structures of MoS_2. The flower - like hierarchical nanostructures exhibit a better degradation of Methylene blue dye compared with the flakes of bulk MoS_2. This morphology dependent activity of MoS_2 opens new perspectives in the field of catalysis.

Keywords: Transition metal dichalcogenides, Molybdenum disulphide, phototocatalyst

1 Introduction

Two dimensional transition metal dichalcogenides (2D TMDs) comprises rich diversity of material properties [1]. They can be a substitute for the zero band gap of graphene and have the capability to go beyond the graphene. Typically, TMDs possess an intrinsic layered structure, a layer of hexagonally connected transition metal atoms are arranged between the chalcogen layers[2], [3]. This tri-layered structures are denoted by a general formula of MX_2, Where M represents a transition metal and X is a chalcogen. The strong covalent bond holds the atoms within the layer whereas the weak Wander Valls force

connects between the layers, which facilitates the easy pealing in to single layers[4]–[6]. The TMDs incorporates the complete hierarchy of chemical properties, starting from metals (VSe_2 and NbS_2), semimetals (WTe_2 and $TiSe_2$), semiconductors (MoS_2 and WS_2), insulators (HfS_2) and up to the low temperature superconductors[7]. These materials find a broad range of applications owing to their unique chemical, physical and optical properties. Optoelectronics, catalysis, energy storage devices[8], Gas sensing [9]and biomedical applications are some of the areas which has been exploited the two dimensional TMDs.

Synthetic chemical dyes are the major portion of the industrial effluents, that contribute to the pollution of water resources. These toxic dyes are hard to degrade and can cause severe health problems even with a very minute quantity. Photocatalytic degradation is stable and low cost solution for the degradation of these poisonous dyes[10]. 2D material based photocatalysis is found to be quite interesting in the last few years. Excellent light harvesting capability, porous structure, high specific surface area, improved charge carrier separation and transportation are some of the contributing factors of 2D materials towards the catalytic activity. In the class of TMDs, Molybdenum disulphide (MoS_2) is an emerging material for the photocatalytic degradation of hazardous dyes. Good chemical stability, strong absorption properties in the visible region, tunable band gap (2 eV) and high carrier mobility, all these factors make MoS_2 a competitive candidate compared to other photocatalysts[11]. The morphology of MoS_2 shows a greater affinity to the photocatalytic activity. There are reported works on MoS_2 for battery applications, hydrogen evolution reactions etc[12]. However, the effect of morphology on the conversion efficiency of photocatalytic degradation of methylene blue (MB) dye has not been investigated in detail to the best of our knowledge.

In the present work, we have prepared the flower like nanostructures of MoS_2 by the facile hydrothermal approach. A comparison has been made with the photocatalytic behaviour of bulk MoS_2 with the flower like structures of MoS_2. The experiment was carried out by studying the photodegradation of methylene blue dye.

2 Experimental

Mn incorporated TiO_2 nanotubes are synthesised by a two step process. The In the experimental part, we have employed the simple hydrothermal method to prepare the hierarchical structures of MoS_2. We have chosen the sodium molybdate dihydrate ($Na_2MoO_4.2H_2O$) as molybdenum (Mo) and thiourea (CH_4N_2S) as sulphur (S) source respectively. The precursors in the ratio of 1:2 were dissolved in 40 ml of distilled water by stirring for 1 hour. Then the mixture solution was enclosed in a Teflon beaker and sealed in a stainless-steel autoclave. The autoclave was kept in a hot air oven for a period of 8 hours and maintained a temperature of 200^0C. The resulting black precipitate was filtered and washed with water several times to remove the impurities. Finally, the precipitate was dried at 60^0C for overnight to obtain the flower like hierarchical structures of MoS_2. Commercially purchased bulk MoS_2 (Sigma-Aldrich, 99%) is used for the comparison.

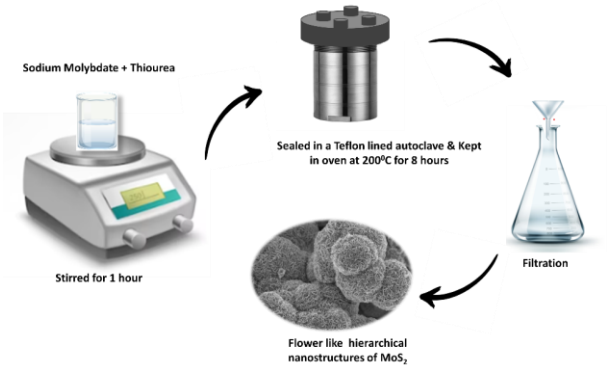

Fig: 1 Schematic representation of hydrothermal synthesis of flowerlike MoS_2

2.1 Catalytic Studies

The photocatalytic activity of Bulk MoS_2 and Hydrothermally prepared MoS_2 were compared in this study. The degradation of Methylene blue is the dye was investigated under the irradiation of a halogen bulb (5W,220V). 10 ppm methylene blue solution was prepared using water as the solvent. Initially, 10 mg of the catalyst was stirred in 10 ppm methylene blue solution under dark

conditions for 30 minutes, until the system attains the adsorption-desorption equilibrium. Then the solution was illuminated with the halogen bulb, the heating of the solution by the lamp was compensated by providing an ice bath around the solution. At regular intervals 2 ml of the solution was collected and the catalyst was removed by centrifugation. Then the collected supernatant was used for recording the UV-Vis spectrum. The absorption spectrum was utilized to study the change in the concentration of the dye.

2.2 Characterization Techniques

The XRD pattern of bulk and hydrothermally synthesized MoS2 was recorded with Rigaku Miniflex powder XRD having Cu-kα radiation of λ=1.54 A0. LabRAM HR micro-Raman spectrometer with Argon ion laser (514.5 nm) as the excitation source was used to obtain the Raman spectrum of the samples. The surface morphology was studied by using the Carl Zeiss field emission scanning electron microscope (FESEM). The absorbance spectra for the photocatalytic study was done with an optical spectrometer FLAME-T-XRI-ES.

3 Results and Discussions

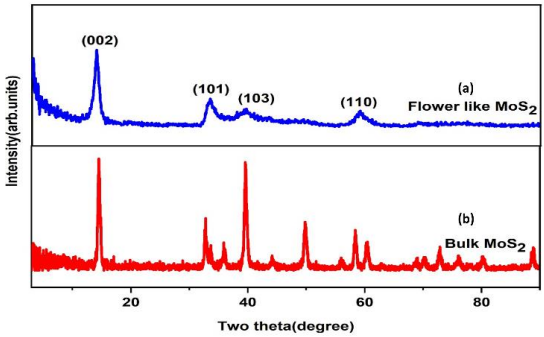

Fig: 2 XRD pattern of (a) Flower like MoS_2 (b) Bulk MoS_2

Figure 2 represents the XRD pattern of hydrothermally prepared MoS_2 and bulk MoS_2. The diffraction peaks were detected at two theta value of 14.1^0,33.60^0, $39.35^0$and 58.83^0 can be indexed to the (002), (101),(103) and (110) diffraction planes respectively. The indexed planes agreeing with the hexagonal 2H phase of MoS_2 (ICDD No: 00-037-1492). The prepared sample

was found to be pure sand crystalline, no impurity peaks were detected. The diffraction peaks of bulk MoS_2 also consistent the ICDD data file no: 00-037-1492.

Raman spectrum is an important tool to characterise the 2D materials. Figure 3 shows the comparison of the Raman spectrum of bulk MoS_2 with the flower like MoS_2. Both the samples exhibit the two characteristic peaks of MoS_2, namely E^1_{2g} and A_{1g}. These two peaks represent the in plane vibration and out of plane vibration of the atoms respectively[13], [14]. The presence of these characteristic peaks confirms the 2H phase of MoS_2, which can be corelated with the XRD results.

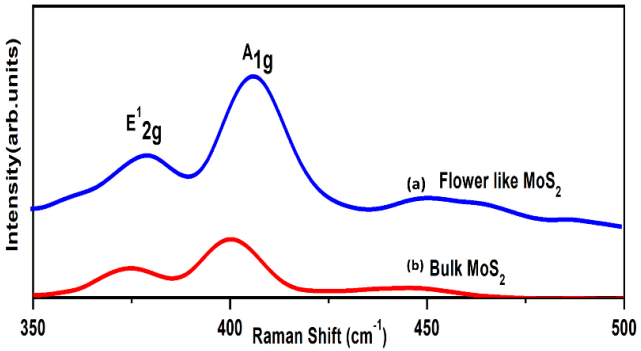

Fig: 3 Raman spectrum of (a) Flower like MoS_2 (b) Bulk MoS_2

The two peaks identified at 375cm^{-1} and 403cm^{-1} for the bulk MoS_2, and these peaks were blue shifted to 380.5 cm^{-1} and 406 cm^{-1} for hydrothermally synthesized MoS_2. The shift in the characteristic peaks can be attributed to the formation of few layered nanostructures.

The morphology of the two samples were studied by using FESEM images. Bulk MoS_2 shows flake like structures. Hydrothermally prepared MoS_2 exhibits a morphology of flower like hierarchical structures. The closely spaced petals are formed by the repeatedly arranged thin sheets of MoS_2. These regularly arranged nanoflowers provides abundant active surface area that facilitates the photocatalytic degradation[15].

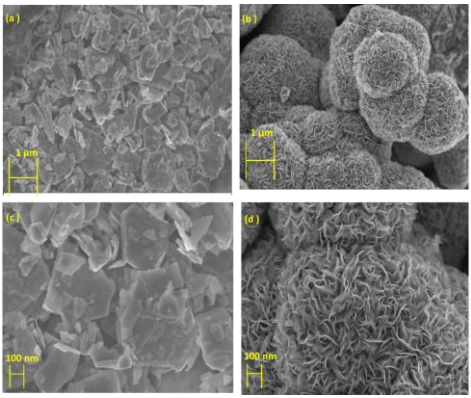

Fig: 3 FESEM images of (a)(c) Bulk MoS_2 , (b)(d) Flower like MoS_2

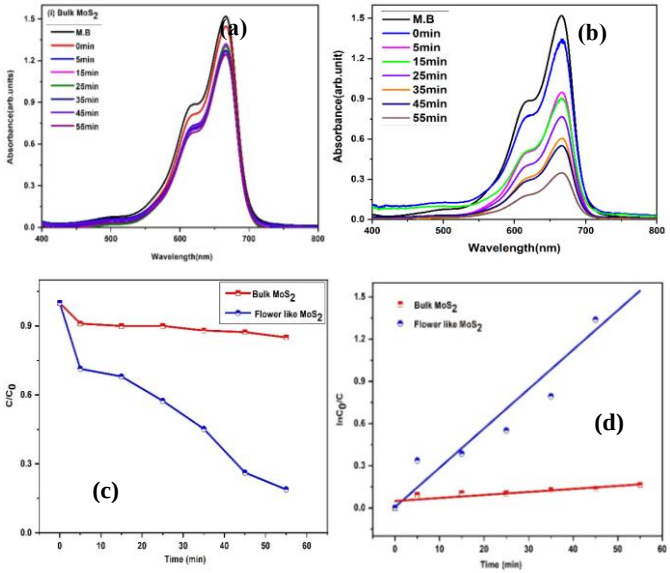

Fig: 4 Absorption spectrum of MB using the catalyst as (a) Bulk MoS_2 , (b) Flower like MoS_2,(c) Comparison of relative absorbance of the two catalysts Vs time (d) Plot of $\ln C_0/C$ Vs time of two catalysts

The photocatalytic degradation of methylene blue is compared using the two catalysts in the presence of halogen bulb. Fig4 (a,b) represents the absorption spectrum of MB at different time intervals using the bulk MoS_2 and hydrothermally prepared MoS_2 as catalysts respectively. The percentage of dye degradation was calculated from the absorbance curves of the dye using the following equation

$$\text{Percentage of degradation} = \{(C_0\text{-}C)/\ C_0\} \times 100 \qquad (1)$$

where, C_0 and C represents the absorbance of MB at initial time and at a time 't'. Methylene blue shows a degradation of 72% in 55 minutes using the hydrothermally prepared MoS_2 whereas, bulk MoS_2 as catalyst can degrade only 18% of MB at the same time. The relative absorbance ($C/\ C_0$) plot of bulk and flower like MoS_2 is compared in the Fig 4(c), which also suggest the superior catalytic activity of flower like structures.

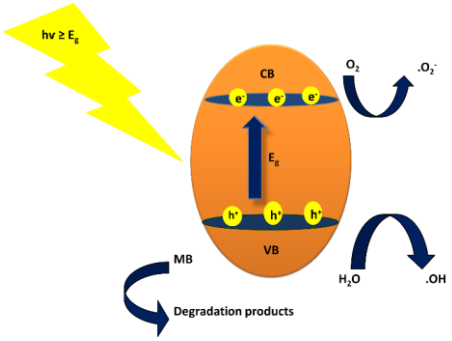

Fig: 5 Picturisation of the mechanism of photocatalytic degradation

The kinetics of photocatalytic degradation was also performed here, and found that the reaction follows the first order kinetics. The equation is given by

$$C = C_0\ e^{-kt} \qquad (2)$$

t is the time and K is the rate constant. The rate constant for the reaction was evaluated by finding the slope of ln (C_0 /C) Vs time curve, Fig 4(d). The bulk flakes of MoS_2 have a rate constant of .00214 min^{-1} while the hierarchical structures have a value of .0155 min^{-1}. The greater value of rate constant also points the better catalytic performance of flower like hierarchical structures.

The schematic representation of mechanism of photocatalytic degradation is displayed in the fig5. At the beginning, the catalyst was stirred in the dark condition, during the stirring the dye molecules get adsorbed on the catalyst surface due to the strong interaction between the two [16]. Then the dye solution containing the catalyst was illuminated with the light source with energy equal to or greater than the band gap. Thus, the electrons (e^-) get excited to the conduction band, dropping holes (h^+) in the valence band. The electron hole pair formed here assists the formation of reactive oxygen species (ROS), which can easily the degrade the toxic dye in to harmless products. The holes in the valence band reacts with the H_2O molecules to produce hydroxide radicals ($OH^{\cdot}$) and H^+ ions. The adsorbed oxygen molecules get reacted with the electrons in the conduction band and forms super oxide radicals ($.O_2^-$). This super oxide radical can degrade the MB dye and also it reacts with H_2O molecules to give the ($OH^{\cdot}$) radicals [17], [18]. The reactive oxygen species ($OH^{\cdot}$ and $.O_2^-$) helps to degrade the harmful dye into nontoxic products[19]. The whole process can be summarized as follows,

$$\text{Photocatalyst} + h\nu \rightarrow h^+ + e^- \quad (3)$$

$$h^+ + H_2O \rightarrow H^+ + OH^{\cdot} \quad (4)$$

$$e^- + O_2 \rightarrow .O_2^- \quad (5)$$

$$.O_2^- + 2H^+ + e^- \rightarrow H_2O_2 \quad (6)$$

$$H_2O_2 + e^- \rightarrow OH^{\cdot} + OH^- \quad (7)$$

4 Conclusion

We have successfully prepared the flower like nanostructures of MoS_2 using the versatile hydrothermal route. The crystalline nature of prepared catalyst was compared with the bulk using XRD and Raman spectrum. FESEM images displays the hierarchical structures of MoS_2, rather than the flakes of bulk MoS_2. These flower like morphology of hydrothermally synthesized MoS_2 is advantageous to the degradation of methylene blue with greater surface area. This enhanced surface area of the prepared catalyst demonstrates a degradation of 72% of methylene blue against the bulk MoS_2.

Acknowledgments

The authors gratefully acknowledge DST-SERB (CRG/2018/003785) for the funding provided. Saranya Sasi acknowledges DCE-ASPIRE scholarship (2021-2022) for the financial support.

References

1. R. Yang *et al.*, "2D Transition Metal Dichalcogenides for Photocatalysis," *Angewandte Chemie - International Edition*, vol. 62, no. 13. John Wiley and Sons Inc, Mar. 20, 2023.
2. N. Chaudhary, M. Khanuja, Abid, and S. S. Islam, "Hydrothermal synthesis of MoS_2 nanosheets for multiple wavelength optical sensing applications," *Sens Actuators A Phys*, vol. 277, no. 2010, pp. 190–198, 2018.
3. Y. Zhang, W. Zeng, and Y. Li, "The hydrothermal synthesis of 3D hierarchical porous MoS_2 microspheres assembled by nanosheets with excellent gas sensing properties," *J Alloys Compd*, vol. 749, pp. 355–362, 2018.
4. M. Pumera and A. H. Loo, "Layered transition-metal dichalcogenides (MoS_2 and WS_2) for sensing and biosensing," *TrAC - Trends in Analytical Chemistry*, vol. 61. Elsevier B.V., pp. 49–53, 2014.
5. V. K. Sangwan and M. C. Hersam, "Electronic Transport in Two-Dimensional Materials," 2018.
6. H. Wang, H. Yuan, S. Sae Hong, Y. Li, and Y. Cui, "Physical and chemical tuning of two-dimensional transition metal dichalcogenides," *Chemical Society Reviews*, vol. 44, no. 9. Royal Society of Chemistry, pp. 2664–2680, 2015.
7. M. Chhowalla, H. S. Shin, G. Eda, L.-J. Li, K. P. Loh, and H. Zhang, "The chemistry of two-dimensional layered transition metal dichalcogenide nanosheets.," *Nat Chem*, vol. 5, no. 4, pp. 263–75, 2013.
8. M. Mattinen, M. Leskelä, and M. Ritala, "Atomic Layer Deposition of 2D Metal Dichalcogenides for Electronics, Catalysis, Energy Storage, and Beyond," *Adv Mater Interfaces*, vol. 8, no. 6, pp. 1–47, 2021.
9. J. R. Jaleel UC, M. R, S. Devi K R, D. Pinheiro, and M. K. Mohan, "Structural, Morphological and Optical Properties of MoS_2-Based Materials for Photocatalytic Degradation of Organic Dye," *Photochem*, vol. 2, no. 3, pp. 628–650, Aug. 2022.
10. R. Ameta, S. Benjamin, A. Ameta, and S. C. Ameta, "Photocatalytic degradation of organic pollutants: A review," *Materials Science Forum*, vol. 734, no. December, pp. 247–272, 2013.
11. B. Luo, G. Liu, and L. Wang, "Recent advances in 2D materials for photocatalysis," *Nanoscale*, vol. 8, no. 13. Royal Society of Chemistry, pp. 6904–6920, Apr. 07, 2016.

12. D. Wang, Z. Pan, Z. Wu, Z. Wang, and Z. Liu, “Hydrothermal synthesis of MoS_2 nanoflowers as highly efficient hydrogen evolution reaction catalysts,” *J Power Sources*, vol. 264, pp. 229–234, 2014.
13. H. Song, A. Tang, G. Xu, L. Liu, Y. Pan, and M. Yin, “Hydrothermal synthesis and electrochemical properties of MoS_2/C nanocomposite,” *Int J Electrochem Sci*, vol. 13, no. 7, pp. 6708–6716, 2018.
14. L. Luo *et al.*, “Hydrothermal synthesis of MoS_2 with controllable morphologies and its adsorption properties for bisphenol A,” *Journal of Saudi Chemical Society*, vol. 23, no. 6, pp. 762–773, 2019.
15. X. Xiao, Y. Wang, B. Cui, X. Zhang, D. Zhang, and X. Xu, “Preparation of MoS_2 nanoflowers with rich active sites as an efficient adsorbent for aqueous organic dyes,” *New Journal of Chemistry*, vol. 44, no. 11, pp. 4558–4567, 2020.
16. H. K. Sadhanala, S. Senapati, K. V. Harika, K. K. Nanda, and A. Gedanken, “Green synthesis of MoS_2 nanoflowers for efficient degradation of methylene blue and crystal violet dyes under natural sun light conditions,” *New Journal of Chemistry*, vol. 42, no. 17, pp. 14318–14324, 2018.
17. Y. Cao, Q. Li, and W. Wang, “Construction of a crossed-layer-structure MoS_2/g-C3N4 heterojunction with enhanced photocatalytic performance,” *RSC Adv*, vol. 7, no. 10, pp. 6131–6139, 2017.
18. B. Yue *et al.*, “Photocatalytic degradation of aqueous 4-chlorophenol by silica-immobilized polyoxometalates,” *Environ Sci Technol*, vol. 36, no. 6, pp. 1325–1329, 2002, doi: 10.1021/es011038u.
19. P. Nandigana, S. Mahato, M. Dhandapani, B. Pradhan, B. Subramanian, and S. K. Panda, “Lyophilized tin-doped MoS_2 as an efficient photocatalyst for overall degradation of Rhodamine B dye,” *J Alloys Compd*, vol. 907, p. 164470, 2022, doi: 10.1016/j.jallcom.2022.164470.

Photocatalytic study of WO_3/rGO nanocomposites on Congo red dye and Rhodamine B

Rajani S Nair[1], Kala M S[1], Reshmi R[2*]

[1]*Department of Physics, St Teresa's College, Ernakulam*
[2]*Department of Optoelectronic and Nanomaterials Research Laboratory, Union Christian College, Aluva*
***rreshmi@gmail.com**

Abstract. In the present study tungsten trioxide based photocatalyst were synthesized by doping WO_3 with Ag and WO_3 with rGO using the hydrothermal method. The ternary compound Ag-WO_3-rGO was synthesized using a two-step hydrothermal method. The characterisation of the samples were done using XRD, SEM, EDX and Raman spectroscopy. The XRD peaks of the samples were in agreement with the monoclinic structure of WO_3 as per the standard JCPDS file. Pure WO_3 has shown less degradation when exposed to visible light for 60 min. In the further study with Ag-WO_3 and rGO-WO_3, the silver doped WO_3 has shown higher degradation compared with rGO doped WO_3 when exposed to visible light for 60 min. The experiment was repeated with ternary Ag-WO_3-rGO also. The results shows that Ag-WO_3 and ternary nanocomposite have excellent photocatalytic activity on Congo red dye and Rhodamine B. The degradation efficiency was observed more in the case of Congo red dye within a given time interval compared with Rhodamine B. The enhanced photocatalytic activity can be due to the increased adsorption of dye molecules, the enhanced light absorption and the increased band gap after doping.

Keywords: Photocatalysis, Tungsten trioxide, Congored, Rhodamine-B

1 Introduction

Photocatalysis has gained considerable attention over the years due to its applications in various fields for waste water treatment and antibacterial applications. The unusual properties of metal oxide nanoparticles have attracted the attention of researchers in the present time. Due to large surface area they are more sensitive to external stimuli like light. Tungsten trioxide (WO_3), a transition metal oxide is an oxygen deficient n type wide band gap semiconductor material with band gap of 2.6 eV – 3.5 eV and can be activated

by visible light irradiation. It is nontoxic, chemically and photo chemically stable. The photocatalytic activity of WO_3 can be improved by doping it with two dimensional layered materials like graphene and transition metals.

2 Experimental

Graphene oxide was synthesized using modified Hummer's method. WO_3, Ag-WO_3, rGO-WO_3 and Ag-WO_3-rGO were synthesized using hydrothermal method.

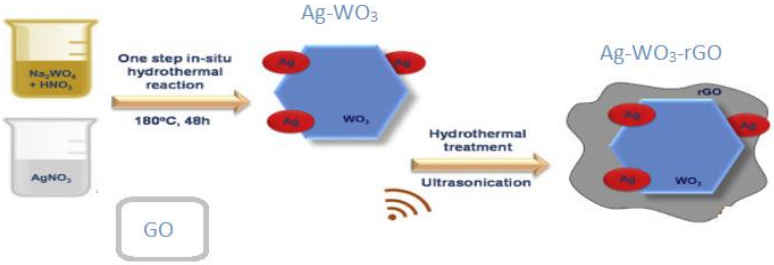

Schematic representation of synthesis of WO_3, Ag-WO_3, rGO-WO_3 and Ag-WO_3-rGO

The structure and morphology of the synthesized samples were characterized using an X-ray diffraction (XRD) with X-ray diffractometer Bruker AXS D8 Advance. The SEM and EDAX were taken using JEOL MODEL JSM-6390LV.

3 Results and Discussions

Fig 1a shows the XRD pattern of GO. The XRD spectrum of GO shows a high intense peak at $2\theta = 11.59^0$, indicating the formation of Graphene oxide structure. Comparing with the XRD spectrum of Graphite it can be observed that graphite shows peak at $2\theta = 26.6^0$[1] and the shifting of peak in the case of Graphene oxide towards the left is due to the oxidation of graphite.

Fig 1b shows the XRD patterns of WO_3, Ag-WO_3, rGO-WO_3 and the ternary sample Ag-WO_3-rGO. In the XRD spectra of the ternary nanocomposite and

rGO-WO_3, the diffraction peaks were not observed in the range from 10^0 to 15^0 showing that GO was completely reduced to rGO. The XRD patterns of the samples WO_3, Ag-WO_3, rGO-WO_3 and ternary Ag-WO_3-rGO were identical to each other substantiating that the direct incorporation of Ag and rGO does not affect the crystal structure of WO_3. The XRD peaks of WO_3, Ag-WO_3, rGO-WO_3 and ternary Ag-WO_3- rGO are in agreement with the monoclinic structure of WO_3 as per the standard JCPDS file no.43-1035. Ag nanoparticles have XRD peaks at around 38^0, 46^0, 64^0 etc. The monoclinic WO_3 also possesses peaks around these values and they are not observed due to the overlap. The XRD analysis also shows that the crystalline size has reduced in the case of WO_3 nanocomposites. The decrease in the crystalline size will enhance the photo catalytic activity due to the increase in surface area thereby increasing the adsorption/desorption.

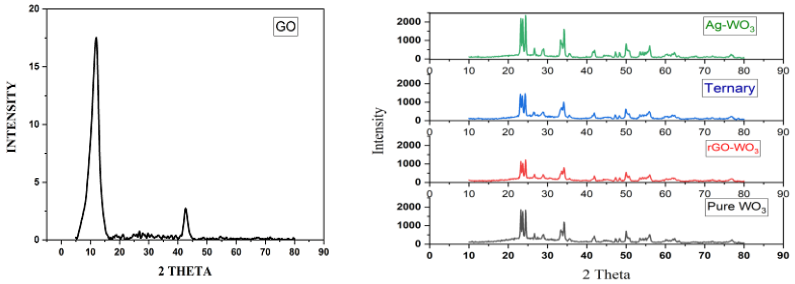

Fig. 1 (a) XRD patterns of GO **(b)** XRD patterns of WO_3 and its nanocomposites

The morphology of the synthesized nanocomposites was observed by SEM. Fig.2a to 2e shows the SEM images of WO_3, Ag-WO_3, rGO-WO_3, ternary nanocomposite and GO respectively.

The SEM image of WO_3 and Ag-WO_3 shows that it has spherical morphology. It was observed that WO_3 nano particles were randomly distributed on rGO sheets in the case of rGO-WO_3. The SEM image of GO shows that the graphene sheets are exfoliated in graphene oxide. The elemental information of the prepared nanocomposite was analysed by EDX. Fig 3 shows the EDX of WO_3 which confirms the presence of elements tungsten and oxygen.

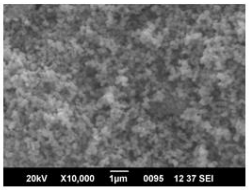

Fig.2 (a) SEM image of WO_3

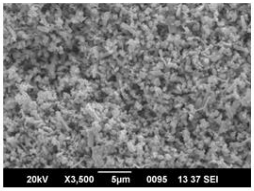

Fig.2 (b) SEM image of Ag-WO_3

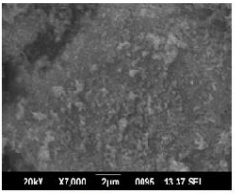

Fig.2 (c) SEM image of rGO-WO_3

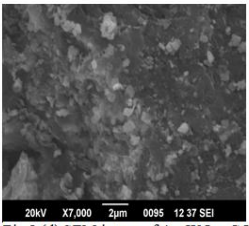

Fig.2 (d) SEM image of Ag-WO_3-rGO

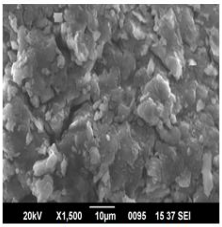

Fig.2 (e) SEM image of GO

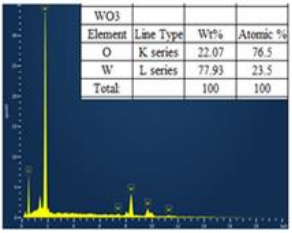

WO3			
Element	Line Type	Wt%	Atomic %
O	K series	22.07	76.5
W	L series	77.93	23.5
Total:		100	100

Fig.3(a) EDX spectrum of WO_3

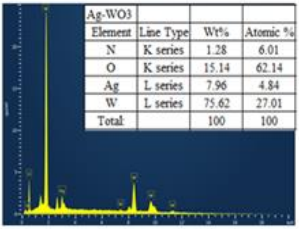

Ag-WO3			
Element	Line Type	Wt%	Atomic %
N	K series	1.28	6.01
O	K series	15.14	62.14
Ag	L series	7.96	4.84
W	L series	75.62	27.01
Total:		100	100

Fig 3(b) EDX spectrum of Ag-WO_3

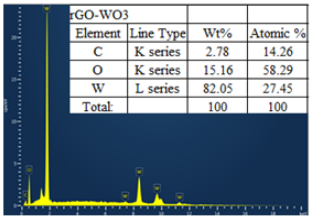

rGO-WO3			
Element	Line Type	Wt%	Atomic %
C	K series	2.78	14.26
O	K series	15.16	58.29
W	L series	82.05	27.45
Total:		100	100

Fig. 3(c) EDX spectrum of rGO-WO_3

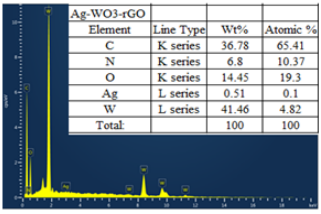

Ag-WO3-rGO			
Element	Line Type	Wt%	Atomic %
C	K series	36.78	65.41
N	K series	6.8	10.37
O	K series	14.45	19.3
Ag	L series	0.51	0.1
W	L series	41.46	4.82
Total:		100	100

Fig. 3(d) EDX spectrum of Ag-WO_3-rGO

Fig.4 shows the Raman spectrum of GO,WO_3, Ag-WO_3, rGO-WO_3 and ternary Ag-WO_3-rGO.The Raman peaks at 272,716 and 804 cm^{-1} confirms the monoclinic structure of WO_3. Some peaks of WO_3 were seen shifted to the lower wavenumber when WO_3 was doped with Ag. This blue shift is due to the shortening of W-O bonds when doped with Ag.

While analysing the Raman spectra of GO, the presence of D band and G band was observed at 1341cm^{-1} and 1579 cm^{-1} respectively. The Raman spectrum of rGO-WO_3, exhibits two bands at 1344 cm^{-1} and 1598 cm^{-1} corresponding to the graphite(G) and diamondoid(D) bands respectively. The same bands were observed in the case of rGO also. These bands are characteristic features of rGO nanocomposites. The G band corresponds to the tangential vibrations of the carbon atom and the D band is the standard sign of the presence of defective graphite carbon [2]. The same bands were observed in the case of ternary nanocomposite also. It was observed that when rGO was introduced to Ag-WO_3, there is a red shift of the G band from 1579 cm^{-1} to 1595 cm^{-1} in the case of ternary Ag-WO_3-rGO nanocomposite. The corresponding shift in the case of rGO -WO_3 is 1598 cm^{-1}. This may be due to the hole transfer between rGO and WO_3/Ag which facilitate the interaction between the components in the nanocomposite [4, 5].

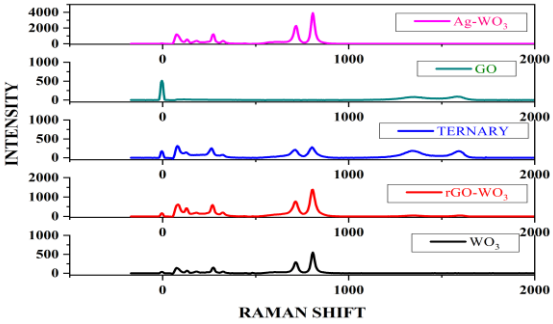

Fig 4. Raman spectrum of GO, WO_3, Ag-WO_3, rGO-WO_3 and ternary Ag-WO_3-rGO

The absorption spectra of WO_3, Ag-WO_3, rGO-WO_3 and Ag-WO_3-rGO samples are given in Fig.5. It can be observed that the spectra of all the samples exhibit a characteristic absorption band around 400 nm, indicating the existence of highly crystallized WO_3.

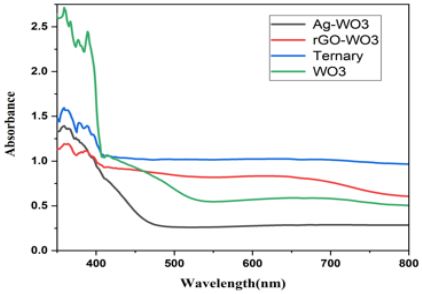

Fig.5 Absorption spectra of WO_3 and its nanocomposites

Tauc's diagram was used to calculate the optical band gap of the samples. The equation is given by

$$\alpha h\upsilon = B\left(h\upsilon - E_g\right)^n \quad \ldots\ldots\ldots\ldots\ldots\ldots\ldots\ldots\ldots\ldots\ldots\ldots \quad (1)$$

where α is the absorption coefficient calculated from absorbance using the equation$\left(\frac{4k}{\lambda}\right)$ where λ is the wavelength of incident photon, hν is the energy of the incident photon, n = ½ or 2 for indirect and direct recombination respectively, B is an arbitrary coefficient and E_g is the optical bandgap of the sample. The extrapolated band gap of WO_3, Ag-WO_3 and rGO-WO_3 are 2.2 eV, 1.4 eV and 1.72 eV respectively. Fig. 6(a) and Fig.6(b) shows the Tauc plot from which the bandgap of WO_3, Ag-WO_3 and rGO-WO_3 were measured.

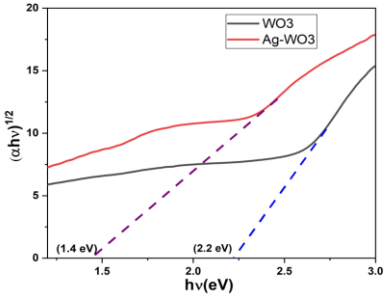

Fig 6(a) Tauc plot of WO_3 and Ag-WO_3

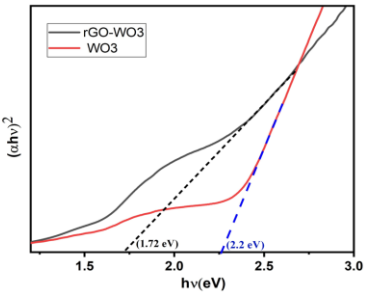

Fig 6(b) Tauc plot of WO_3 and rGO-WO_3

The photocatalytic activity of the samples is analysed by measuring its change in absorbance caused by the degradation of Congo red dye for 60 min when

irradiated with visible light. 25 mg of the prepared samples were added into 10 mL of the prepared 10 ppm dye solution and kept under dark conditions for 10 min.The absorption of catalyst added dye irradiated under light was then measured by a UV-Vis spectroscopy .Fig.7(a) to Fig.7(d) shows the photocatalytic activity of WO_3, Ag-WO_3, rGO-WO_3 and ternary respectively. The degradation efficiency of the dye was determined by the equation (3.2)

$$PDE(\%) = \frac{C_0 - C_t}{C_0} \times 100 = \frac{I_0 - I_t}{I_0} \times 100 \quad \ldots\ldots\ldots\ldots\ldots\ldots\ldots\ldots \quad (2)$$

The degradation rate of Congo red dye with WO_3 photocatalyst has shown 35.73% within 60 min of illumination, whereas WO_3 doped with Ag, exhibits a much higher degradation efficiency of 63.33%. The incorporation of WO_3 nanoparticles with rGO sheets also have increased the degradation efficiency by 56.86% within 60 min illumination. The process was repeated with ternary nanocomposite and the complete degradation of the Congo red dye within 120 min under visible irradiation was observed. This result indicates that Ag-WO_3, rGO-WO_3 and ternary Ag-WO_3-rGO nanocomposite shows improved photocatalytic activity for the effective treatment of organic dye pollutants compared with pure WO_3.

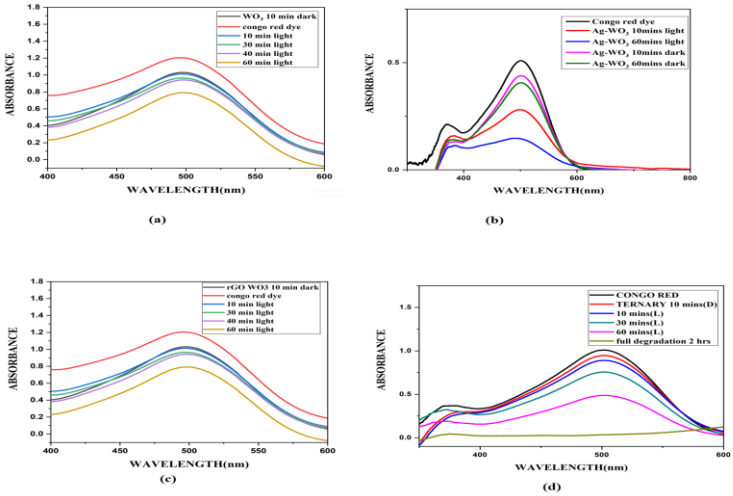

Fig.7 Absorption spectra of Congo red dye in the presence of light (a) WO_3 (b) Ag-WO_3(c) rGO-WO_3 (d) Ag-WO_3-rGO

The degradation of Rhodamine B (RhB) dye was investigated by the prepared samples for 60 min under visible light irradiation. Fig.8(a) to Fig.8(d) shows the photocatalytic activity of WO_3, Ag-WO_3, rGO-WO_3 and ternary nanocomposites respectively on RhB. Ternary, Ag-WO_3 and rGO-WO_3 have shown improved photocatalytic activity compared with pure WO_3.

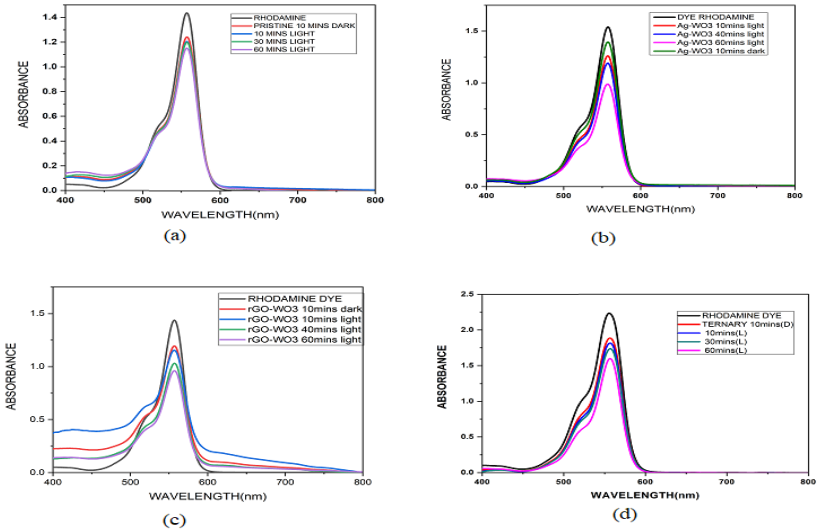

Fig.8 Absorption spectra of Congo red dye in the presence of light (a) WO3 (b) Ag-WO3 (c) rGO-WO3 (d) Ag-WO3-rGO

When WO_3 is doped with Ag, it is seen that Ag acts as an electron reservoir which enhances the photocatalytic activity of Ag-WO_3. In the case of rGO-WO_3 the addition of rGO into WO_3 would increase the specific surface area of photocatalyst. Moreover due to π - π interaction between the dye and the benzene rings of rGO, there will be more interaction between the dye and rGO which could enhance the adsorption of dye in rGO-WO_3 [3]. The enhanced adsorption can be attributed to the hydrogen-bonding interactions between H (δ+) of rGO and OH- (δ-) of dye [4].

The photocatalytic degradation mechanism of the dye solution by the WO_3 photocatalyst under visible light irradiation can be can be explained as follows.

When WO3 is irradiated with visible radiation, an electron in the valence band excites to the conduction band and a hole is created in the valence band. The electrons at the photocatalyst surface were prohibited by the molecular oxygen to produce the superoxide radical anion .O2. The superoxide radical anion .O2, further combines with H to generate .HO2. Finally, the photocatalytic degradation of the dye takes place. The active oxygen species (.OH, .HO2 or .O2 radicals) and the dyes were degraded gradually. The dye adsorbs the proton and protonates and this protonation continues and the degraded products are obtained after the certain period of time [6, 7].

When WO3 is doped with Ag, it has more defects on its grain boundary. The band gap of Ag-WO3 is lowered which can be excite more valence electrons up to the conduction band under visible light irradiation leaving holes in the valence band [8, 9]. The holes can interact with the electrons from OH- or water molecules to form hydroxyl radicals (.OH). The electrons in the conduction band (or doped Ag) can combine with the dissolved oxygen to form O_2-. Both the .OH and O_2- can contribute to the degradation of dye molecules. The addition of rGO restricts the recombination of the photogenerated electron-hole pairs which improves the photocatalytic activity of the ternary Ag-WO3-rGO nanocomposite [4].

4 Conclusion

The photocatalytic activity of WO3, Ag-WO3, rGO-WO3 and ternary Ag-WO3 -rGO in aqueous Congo red dye and Rhodamine B solution were studied. The results show that Ag-WO3 and ternary nanocomposite show excellent degradation of Congo red dye and Rhodamine B under visible light irradiation. The optical band gap of the samples were reduced when WO3 was doped with Ag/rGO which enhanced the photocatalytic activities. The enhanced photocatalytic activity can be attributed to the increased adsorption of dye molecules, the enhanced light absorption and the efficient charge separation.

Acknowledgments

The authors gratefully acknowledge DCE-ASPIRE scholarship (2021-2022) for the financial support.

References

1. Faiz, MS Amir, CA Che Azurahanim, Syahidah Azis Raba'ah, and Mohd Zawawi Ruzniza. "Low cost and green approach in the reduction of graphene oxide (GO) using palm oil leaves extract for potential in industrial applications." Results in Physics 16 (2020): 102954.
2. Mohammed Harshulkhan, S., K. Janaki, G. Velraj, R. Sakthi Ganapthy, and M. Nagarajan. "Effect of Ag doping on structural, optical and photocatalytic activity of tungsten oxide (WO3) nanoparticles." Journal of Materials Science: Materials in Electronics 27, no. 5 (2016): 4744- 4751.
3. Fu, Li, Tian Xia, Yuhong Zheng, Jun Yang, Aiwu Wang, and Zhong Wang. "Preparation of WO3-reduced graphene oxide nanocomposites with enhanced photocatalytic property." Ceramics International 41, no. 4 (2015): 5903-5908.
4. Tran, Vy Anh, Thang Phan Nguyen, Il Tae Kim, Sang-Wha Lee, and Cong Tu Nguyen. "Excellent photocatalytic activity of ternary Ag@ WO3@ rGO nanocomposites under solar simulation irradiation" Journal of Science: Advanced Materials and Devices 6, no. 1 (2021): 108-117.
5. Nguyen, Cong Tu, Tuan Phong Pham, Thi Lan Anh Luu, Xuan Sang Nguyen, Thanh Tung Nguyen, Huu Lam Nguyen, and Duc Chien Nguyen. "Constraint effect caused by graphene on in situ grown Gr@ WO3-nanobrick hybrid material" Ceramics International 46, no. 7 (2020): 8711-8718.
6. Jeyapaul, T., K. Prakash, S. Harikengaram, A. Chellamani, and V. Selvam. "Synthesis of WO3 nanorods and their photocatalytic degradation of organic contaminants." Rasayan J. Chem 11, no. 4 (2018): 1405-1414.
7. Ke, Dingning, Huajun Liu, Tianyou Peng, Xun Liu, and Ke Dai. "Preparation and photocatalytic activity of WO3/TiO2 nanocomposite particles." Materials Letters 62, no. 3 (2008): 447-450.
8. Matalkeh, Maha, Gheyath K. Nasrallah, Farah M. Shurrab, Enas S. Al-Absi, Widad Mohammed, Ahmed Elzatahry, and Khaled M. Saoud. "Visible light photocatalytic activity of 40 Ag/WO3 nanoparticles and its antibacterial activity under ambient light and in the dark." Results in Engineering 13 (2022): 100313.
9. Maha, Matalkeh, Gheyath K. Nasrallah, Farah M. Shurrab, Enas S. Al-Absi, Widad Mohammed, Ahmed Elzatahry, and Khaled M. Saoud. "Visible Light Photocatalytic Activity of Ag/WO3 Nanoparticles and its Antibacterial Activity Under Ambient Light and in The Dark." (2022).

Biosensors Based On Novel 2D Nanomaterials: A Short Review

Christeena Thomas[1], Reshmi R[1*]
[1]*Optoelectronic and Nanomaterial's Research Laboratory, Department of Physics, Union Christian College, Aluva, Kerala 683102,India*
***rreshmi@gmail.com**

Abstract. Biosensors are analytical devices that can ensure specific, sensitive, and fast responses by quantifying biological, physical, or chemical events. Biosensors have a wide spectrum of applications in industry, agriculture, healthcare monitoring, defense, security, etc. In recent years researchers have witnessed the capability of novel nanomaterials to revolutionize the potential of biosensors. The unique physiochemical and mechanical properties of nanomaterials can offer very fast, robust, real-time, and stable detection of events without compromising their selectivity and sensitivity. Among different nanomaterials, two- Dimensional(2D) nanomaterials hold high surface-to-volume ratios with excellent electrical, optical, and catalytic properties. This review focuses on the role of 2D nanomaterials in advanced biosensors giving more importance to electrochemical biosensors

Keywords: Biosensor, electrochemical analysis.

1 Introduction

Nanotechnology has the ability to engineer the materials precisely at the nanometre scale and these new unique materials can exhibit different characteristics and properties from bulk material. Nanotechnology offers a broad range of applications from electronics, Optical communication, and biological systems. It impacts biomedical research and technology for studying the fundamental interactions and dynamics at the single cell/molecule level [1,2]. In the current scenario of biomedical research, accurate and early detection of various diseases at the early stages of disease development has significant importance. There is a need to enhance the capability of sensor technology for health, environmental monitoring, and biological analysis. The main area of concern is new strains of microbial organisms and the spread of infectious diseases that require rapid detection and identification. Progress in nanotechnology resulted in the fabrication of highly selective biosensors with ultrasensitivity and selectivity [3].

Biosensors are analytical devices that use biological recognition elements such as enzymes, antibodies, or nucleic acids, to detect the presence or concentration of specific analytes. The first biosensor was developed by Leland C. Clark Jr. and co-workers in 1962 to measure the concentration of oxygen in blood using the enzyme glucose oxidase as the recognition element [4]. The first commercial biosensor was introduced in 1975 by Yellow Spring Instruments. Since then, biosensors have been extensively used in numerous applications including medical diagnosis, environmental monitoring, food safety, military purposes, and bio processing [5]. The principle of biosensors is based on the specific binding interaction between the biological recognition element and the target analyte, which results in a measurable signal.

Research now shows that the introduction of different nanomaterials such as metal oxides, metal nanoparticles, carbon-based materials, 2D nanomaterials, and their hybrids can effectively improve the performance of a sensor. The properties such as linear range, sensitivity, quick response, detection limit, selectivity, biocompatibility, and stability determine the applicability of nanomaterials in biosensors [6]. Among different nanomaterials 2D nanomaterials have extra importance in biomedical research because of their unique physiochemical properties including high surface-to-volume ratios and tunable electronic properties. They belong to a large and diverse class of carbon material, chalcogenides, phosphides, nitrides, halides, and layered silicate minerals. They may be individual nanosheets or layered multi-sheet planar materials. Depending on chemical compositions and structural configurations, they can be classified as metallic, semi-metallic, semiconducting, insulating, or superconducting [7,8].

2 Biosensors

According to Eggins, a biosensor is *"A device incorporating a biological sensing element connected to a transducer to convert an observed response into a measurable signal, whose magnitude is proportional to the concentration of a specific chemical or set of chemicals"*. Every biosensor is typically composed of three main components: A biological sensing element, a transducer, and a signal processor. Based on the receptor type and transduction mechanism biosensors are classified into different categories. Depending on the transducers used biosensors are classified into electrochemical, optical, and mechanical biosensors. Looking into the receptor

type biosensors are classified into enzyme-based, DNA-based, antibody-based, aptamers, and immun0 sensors [9,10]. A schematic representation of a general biosensor is shown in figure 1.

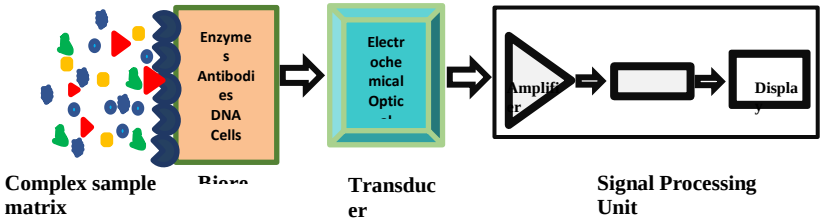

Fig 1. Schematic representation of electrochemical sensor

The desirable features of a biosensor are,

1. Selectivity:- A biosensor should be specific to a particular analyte of interest while disregarding all the other components in the sample.
2. Sensitivity:- It should be able to detect the minimal concentration of an analyte even in a complex sample matrix.
3. Stability:- A biosensor must be capable to perform over time without any degradation in activity.
4. Speed:- It should provide rapid real-time responses, especially in the case of point-of-care devices.
5. Reproducibility:- It should provide consistent and reliable results irrespective of any environmental conditions.
6. Miniaturization:- In the case of a point care device it should be small and portable.
7. Affordability:- It should be accessible, user-friendly, and low-cost.
8. Biocompatibility:- When used in a biological system a biosensor does not cause any adverse effect on the system.

On a broad spectrum, biosensors are classified into enzymatic and non-enzymatic biosensors.

2.1 Enzymatic Biosensors

Enzymatic biosensors use enzymes as the biological recognition element and they are conjugated with a physical transducer. It can provide highly specific and selective detection of analyte molecules [11]. Immobilization of enzymes to a solid support or matrix is a crucial part of the fabrication of enzyme-based biosensors. This can be achieved in many ways like adsorption, entrapment,

crosslinking, covalent binding, etc. The choice of immobilization depends on the application and type of enzyme. Enzymatic biosensors require specific environments to maintain their stability [12].

2.2 Non-enzymatic Biosensors

Although enzyme-based biosensors can offer high specificity to a particular analyte they are very sensitive to environmental conditions and it has many disadvantages like limited stability, potential interference, nonregenerative, incapability to detect a wide range of compounds, susceptibility to harsh conditions, and moreover, they are relatively very costly. Non-enzymatic biosensors make use of the unique properties of nanomaterials such as high surface area, stability, mechanical strength, and optoelectronic and catalytic properties to obtain more promising sensing. They can be used as transducers to increase signal strength, conjugation platforms for biomolecules, and quantify and identify a particular analyte without using any biological component. Mostly metal nanoparticles like gold, silver, and platinum and several other nanomaterials such as quantum dots, carbon-based nanomaterials, metal oxides, etc are used as non-enzymatic biosensors [12,13]. Recent studies revealed that 2D materials like graphene, transition metal dichalcogenides, black phosphorus, hBN, etc can be used in biosensors owing to their distinctive properties.

3 Major Two-Dimensional Nanomaterials based Biosensors

3.1 Graphene and Graphene Oxide

Graphene is an sp2 hybridized covalently bonded hexagonal structure of a single layer of carbon atoms. In graphene three carbon atoms form a sigma bond with three other carbon atoms and the fourth carbon atom is a pi orbital which is situated perpendicular to the sigma bond and is highly mobile giving graphene exceptional conductivity, carrier mobility, and easy functionalization makes graphene a promising candidate for many potential applications [14,15].

The advanced biosensor application exploits the versatile properties of graphene such as very good chemical stability, electronic properties, strength, and flexibility.

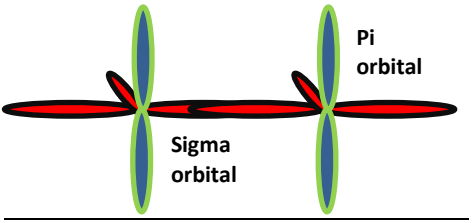

Fig 2. Orbital structure of graphene

3.2 Graphene Oxide

Graphene Oxide (GO) is a derivative of graphene having abundant oxygen-containing functional groups. GO can be synthesized by oxidizing graphite using different methods. Oxidization of graphite causes disruption in the crystalline structure and a reduction in elasticity and strength. However, from the biosensing point of view, the presence of both sp2 and sp3 hybrid structures provides GO with a hydrophilic nature that can increase its biocompatibility which has great importance when used in biological systems [15].

3.3 Transition Metal Dichalcogenides

Beyond graphene, the most prominent and well-known 2D material family is transition metal dichalcogenides (TMD) or TMDCs with MX2 stoichiometry (M- Transition Metal, X-Chalcogen) and they are a sandwiched structure of transition metal and chalcogenides. MoS_2, $MoSe_2$, and WS_2 are examples of 2D layered TMDs, and CoS_2, $CoSe_2$, NiS_2, FeS_2, etc. are cubic pyrite- or orthorhombic marcasite-type TMDs [16]. The fundamental advantage of TMDs is their ability to exhibit a number of properties that graphene does not have or that can only be carried out at an excessively high cost. The intrinsic bandgaps of TMDCs are a fascinating feature that may be modified using many techniques, such as altering the thickness or number of layers, alloying, strain engineering, defect engineering, phase modulation, and surface modification or functionalization [17]. TMDs can exist in different structural phases from the semiconducting 2H phase and semi-metallic 3R phase to the metallic 1T Phase where the 2H phase is the most stable phase. Every single layer of TMDs consists of three layers where X-M-X are bonded together by strong covalent bonds. Generally, single-layer TMDs have a thickness of approximately 0.65nm. TMDs have a unique property of layer-dependent bandgap transition

from indirect to direct when reduced to bulk to monolayers. The intrinsic anisotropic structure, biocompatibility, catalytic property, and semiconducting nature can be exploited in many biomedical applications [18].

3.4 Black phosphorus

Black Phosphorus is a 2D crystalline allotrope of a puckered layer of phosphorus atoms arranged in a honeycomb lattice. Due to the puckered structure, each atom is displaced above or below the plane of the layer creating zig-zag and armchair directions. There are many reports on BP-based nano biosensors. However, BP is comparatively a new material and the biggest challenge with BP is stability, it can degrade quickly in air and water [19].

3.5 MXenes

MXenes are composed of transition metal carbides, nitrides, or carbonitrides and can be synthesized by selective etching of layers of aluminum from MAX phases. MXenes can offer good electrical conductivity, mechanical strength, and biocompatibility [20].

4 Biosensing Methods

4.1 Electrochemical Biosensors

Electrochemical biosensors use the electrochemical signal derived from the reaction between the receptor molecule and the desired analyte molecule to precisely and quantitively analyze the molecule. The produced electrochemical signal can be detected in terms of current, voltage, capacitance, impedance, etc. There are many electrochemical techniques like Cyclic Voltammetry (CV), chronoamperometry, differential pulse voltammetry, square wave voltammetry, etc can be employed for proper analysis of the material. Depending upon the mechanism used electrochemical sensors can be further classified into impedimetric, amperometric, capacitive, or potentiometric. An electrochemical sensing setup is shown in the figure below [11].

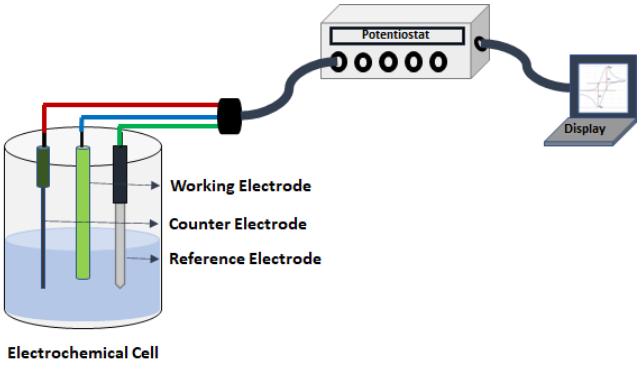

Fig 3. Electrochemical sensing setup

4.2 Impedimetric Biosensors

Impedance is the measure of the ability of an electrical circuit to resist the flow of current. In an impedimetric biosensor, the changes in electrical impedance in response to a particular analyte are used to sense a particular molecule. The impedance of a circuit can be calculated by applying an AC voltage and by measuring the corresponding current. In impedance spectroscopic techniques impedance can be represented as the real and imaginary part of the Nyquist diagram. Further, the solution and electrode properties like charge transfer resistance, double-layer capacitance, solution resistance, Warburg impedance, and constant phase element can be measured by drawing Randle's equivalent circuit of the Nyquist plot. Impedance spectroscopy is a powerful tool to correctly detect and analyze various biological molecules. In a study, Akhilesh Babu Ganganboina et al fabricated an impedimetric sensor for the detection of carcinoembryonic antigen which is a biomarker for colorectal cancer [21].

4.3 Amperometric Biosensors

Amperometric biosensors works by measuring the current that can be produced by oxidation and reduction of target molecules at the working electrode by applying a particular voltage. Then the response can be recorded as a time vs current graph. The amount of current produced will be directly proportional to the concentration of the analyte [22].

4.4 Potentiometric Biosensors

These measures the potential difference between two electrodes in the presence of target molecules. The binding of the analyte to the receptor molecule changes the charge distribution near the electrodes, which can be related to the concentration of specific molecules [23].

Its simplicity, cost-effectiveness, and rapid response make it a powerful tool and technique to detect various biomolecules. Graphene, GO, and rGO can be used as effective electrochemical sensors for detecting various biomolecules. Chenyu Wang et al and co-workers fabricated a label-free graphene-based FET-aptasensor for the detection of lead in blood samples collected from children. The presence of lead in blood is highly toxic, especially for children. The sensor showed a detection limit below 37.5ng/L toward Pb^{2+} [24]. An electrochemical sensor for the detection of dopamine using graphene-WO_3 composite with a detection limit of .306micro molar with a selectivity of 0.392 micron/microM was reported by V.Anbumannan and co-workers using chronoamperometry [25]. Another study reported an rGO-based sensor for the detection of cholesterol[26]. TMDs are the emerging class of 2D material with high biocompatibility. For instance, an electrochemical sensor for the detection of carcinoembryonic antigen (CEA) based on MoS_2 was reported by Enhui Ma et al and co-worker [27]. Jinho Yoon et al and co-workers fabricated a glucose sensor by immobilizing glucose oxidase (GOx) on a gold/MoS2/gold nanofilm showing a detection limit of 10nM with 3.48mm of flexure extension [28].

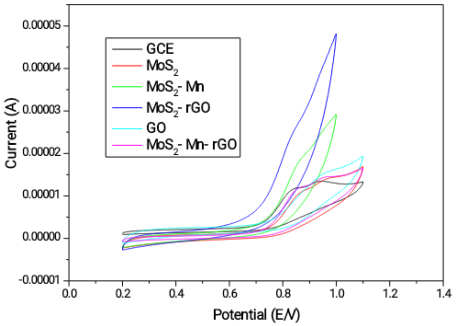

Fig: 4 Comparison of Cyclic Voltammogram response of different electrodes towards 1mM of folic acid

Figure 4 shows the cyclic voltammogram response of different electrodes obtained from our study towards 1 mM of folic acid (FA). In the study, we have doped 2D flower-like MoS_2 with manganese (MoS_2- Mn), reduced graphene oxide (MoS_2- rGO), and both Mn and rGO (MoS_2- Mn- rGO). The level of doping concentration was 1%. Every material was synthesized using the conventional hydrothermal route except graphene oxide (GO), GO was synthesized using a modified Hummer's method. From the figure, we can deduce that the MoS_2- rGO composite electrode has the highest sensitivity and electrocatalytic activity toward FA.

4.5 Optical Biosensors

Optical biosensors use an optical transducer combined with a light source to sense different biological events and convert them into electrical signals by measuring changes in reflection, refraction, absorption, transmission, phase, amplitude, frequency, etc. Optical phenomenons like fluorescence, SPR, Raman scattering, etc can be used as the fundamental mechanisms for fabricating optical biosensors.

4.5.1 Fluorescence-Based Biosensors

It uses the property of fluorescence to selectively detect the particular analyte of interest. Fluorescence is the property that certain materials absorb light of a particular wavelength and emit light at a longer wavelength. Typically a fluorescent biosensor has four components a light source, fluorophore, wavelength filter, and a detector. 2D materials like graphene, MoS_2, and black phosphorous have strong fluorescence properties and there are reports of sensors based on these materials to detect DNA, proteins, glucose, etc using fluorescence [29-31].

4.5.2 SPR-Based Biosensors

Surface plasmons are electromagnetic waves that propagate along the interface between a thin metal film and a dielectric medium. When the angle of incidence and the wavelength of the source of light became matched, the surface plasmon will get excited and resonate at a particular angle called resonance angle. The SPR-based biosensor works on the idea of change in refractive index when a molecule binds to the surface of a metal. When a

sample containing the analyte of interest comes in contact with the receptor molecule that will bind with the receptor molecule. Then the change in angle/intensity of the light will be recorded [32]. 2D materials exhibit strong light-matter interaction and can be used in SPR-based biosensors [33].

4.5.3 SERS-Based Biosensors

It works on the principle of enhancement of the Raman signal of the molecule when a laser beam comes in contacts with the nanostructured metal surface such as silver or gold. This occurs due to the localized surface plasmon resonance effect because of the collective oscillation of electrons in the metal surface when excited by incident light. This enhancement in the Raman signal can produce a unique vibrational fingerprint of a molecule that helps to quantify and identify the molecule [34]. The unique electrical, optical, and structural properties of 2D materials can be exploited in SERS-based biosensors [35].

4.6 Piezoelectric Biosensors

The changes in physical phenomena such as pressure, force, strain, acceleration, etc can be made used in a piezoelectric sensor. Here biomolecules can be attached with a piezoelectric surface and can be used as the transducer element. When the analyte binds to the receptor molecule, it produces mechanical stress that will lead to a change in the surface charge of the material. Mainly, quartz crystals, lithium niobate, lagasite, etc are used the piezoelectric materials [36]. Graphene and MoS_2 are the most common 2D materials used in piezoelectric biosensors.

5 Conclusion

Biosensors based on 2D materials can assure several advantages over conventional sensors such as high sensitivity, selectivity, and specificity. The properties such as high surface area, biocompatibility, and electrical, optical, and mechanical characteristics make 2D materials ideal for many biological applications. However, there are still many challenges that should be addressed to commercialize sensors based on 2D materials especially the scalability problems and integration of these materials with the existing technology. Despite these challenges, the current research progress points towards the vast

scope of 2D materials in biomedical applications. With continued research, researchers can make high-speed, portable, low-cost, ultrasensitive biosensors based on 2D materials.

Acknowledgments

The authors gratefully acknowledge KSCSTE SARD scheme and DST-SERB (CRG/2018/003785) for the funding provided.

References

1. Mehrotra, P. Biosensors and their applications – A review. *J Oral Biol Craniofac Res* **6**, 153–159 (2016).
2. Singh, S. *et al.* Biological Biosensors for Monitoring and Diagnosis. in 317–335 (2020). doi:10.1007/978-981-15-2817-0_14.
3. Baker, G. A. Nanophotonics By Paras N. Prasad (SUNY, Buffalo). John Wiley & Sons, Inc.: Hoboken, NJ. 2004. xvi + 416 pp. $84.95. ISBN 0-471-64988-0. *J Am Chem Soc* **127**, 14118–14119 (2005).
4. Heineman, W. R. & Jensen, W. B. Leland C. Clark Jr. (1918–2005). *Biosens Bioelectron* **21**, 1403–1404 (2006).
5. Guilbault, G. G. & Montalvo, J. G. Urea-specific enzyme electrode. *J Am Chem Soc* **91**, 2164–2165 (1969).
6. Zribi, R. & Neri, G. Mo-Based Layered Nanostructures for the Electrochemical Sensing of Biomolecules. *Sensors* **20**, 5404 (2020).
7. Raja, I. S. *et al.* Development of Two-Dimensional Nanomaterials Based Electrochemical Biosensors on Enhancing the Analysis of Food Toxicants. *Int J Mol Sci* **22**, 3277 (2021).
8. Bolotsky, A. *et al.* Two-Dimensional Materials in Biosensing and Healthcare: From *In Vitro* Diagnostics to Optogenetics and Beyond. *ACS Nano* **13**, 9781–9810 (2019).
9. Malhotra, B. D. & Ali, Md. A. Nanomaterials in Biosensors. in *Nanomaterials for Biosensors* 1–74 (Elsevier, 2018). doi:10.1016/B978-0-323-44923-6.00001-7.
10. Filice, M., Marchal, J. A. & Gamiz, F. Biosensors based on two-dimensional materials. in *2D Materials for Nanophotonics* 245–312 (Elsevier, 2021). doi:10.1016/B978-0-12-818658-9.00004-1.
11. Revathi, C. & Rajendra kumar, R. T. Enzymatic and Nonenzymatic Electrochemical Biosensors. in *Fundamentals and Sensing Applications of 2D Materials* 259–300 (Elsevier, 2019). doi:10.1016/B978-0-08-102577-2.00007-5.
12. Mohammadpour-Haratbar, A., Mohammadpour-Haratbar, S., Zare, Y., Rhee, K. Y. & Park, S.-J. A Review on Non-Enzymatic Electrochemical Biosensors of

Glucose Using Carbon Nanofiber Nanocomposites. *Biosensors (Basel)* **12**, 1004 (2022).
13. Li, X. *et al.* Graphene and related two-dimensional materials: Structure-property relationships for electronics and optoelectronics. *Appl Phys Rev* **4**, 021306 (2017).
14. Yildiz, G., Bolton-Warberg, M. & Awaja, F. Graphene and graphene oxide for bio-sensing: General properties and the effects of graphene ripples. *Acta Biomater* **131**, 62–79 (2021).
15. Manzeli, S., Ovchinnikov, D., Pasquier, D., Yazyev, O. V. & Kis, A. 2D transition metal dichalcogenides. *Nat Rev Mater* **2**, 17033 (2017).
16. Dong, Z. & Chang, L. Recent electroporation-based systems for intracellular molecule delivery. *Nanotechnology and Precision Engineering* **4**, 045001 (2021).
17. Wang, B. *et al.* Bioelectronics-Related 2D Materials Beyond Graphene: Fundamentals, Properties, and Applications. *Adv Funct Mater* **30**, 2003732 (2020).
18. Choi, J. R. *et al.* Black Phosphorus and its Biomedical Applications. *Theranostics* **8**, 1005–1026 (2018).
19. Gogotsi, Y. & Anasori, B. The Rise of MXenes. *ACS Nano* **13**, 8491–8494 (2019).
20. Ganganboina, A. B. & Doong, R.-A. Graphene Quantum Dots Decorated Gold-Polyaniline Nanowire for Impedimetric Detection of Carcinoembryonic Antigen. *Sci Rep* **9**, 7214 (2019).
21. Wang, J. Amperometric biosensors for clinical and therapeutic drug monitoring: a review. *J Pharm Biomed Anal* **19**, 47–53 (1999).
22. Ding, J. & Qin, W. Recent advances in potentiometric biosensors. *TrAC Trends in Analytical Chemistry* **124**, 115803 (2020).
23. 23. Wang, C. *et al.* A label-free and portable graphene FET aptasensor for children blood lead detection. *Sci Rep* **6**, 21711 (2016).
24. Anbumannan, V., Kumar, R. T. R. & Suresh, K. Enhanced electrochemical detection of dopamine by graphene oxide/tungsten trioxide nanocomposite. *Mater Sci Semicond Process* **127**, 105696 (2021).
25. Wu, S. *et al.* Gold nanoparticles/single-stranded DNA-reduced graphene oxide nanocomposites based electrochemical biosensor for highly sensitive detection of cholesterol. *Front Chem Sci Eng* **15**, 1572–1582 (2021).
26. Ma, E. *et al.* Electrochemical immunosensor based on MoS2 NFs/Au@AgPt YNCs as signal amplification label for sensitive detection of CEA. *Biosens Bioelectron* **142**, 111580 (2019).
27. Yoon, J. *et al.* Flexible electrochemical glucose biosensor based on GOx/gold/MoS2/gold nanofilm on the polymer electrode. *Biosens Bioelectron* **140**, 111343 (2019).
28. 28. Salama, A. M., Yasin, G., Zourob, M. & Lu, J. Fluorescent Biosensors for the Detection of Viruses Using Graphene and Two-Dimensional Carbon Nanomaterials. *Biosensors (Basel)* **12**, 460 (2022).

29. 29. Xiang, X. *et al.* MoS2 nanosheet-based fluorescent biosensor for protein detection via terminal protection of small-molecule-linked DNA and exonuclease III-aided DNA recycling amplification. *Biosens Bioelectron* **74**, 227–232 (2015).
30. Yew, Y. T., Sofer, Z., Mayorga-Martinez, C. C. & Pumera, M. Black phosphorus nanoparticles as a novel fluorescent sensing platform for nucleic acid detection. *Mater Chem Front* **1**, 1130–1136 (2017).
31. Shpacovitch, V. & Hergenröder, R. Surface Plasmon Resonance (SPR)-Based Biosensors as Instruments with High Versatility and Sensitivity. *Sensors* **20**, 3010 (2020).
32. Lei, Z. & Guo, B. 2D Material-Based Optical Biosensor: Status and Prospect. *Advanced Science* **9**, 2102924 (2022).
33. Ambartsumyan, O., Gribanyov, D., Kukushkin, V., Kopylov, A. & Zavyalova, E. SERS-Based Biosensors for Virus Determination with Oligonucleotides as Recognition Elements. *Int J Mol Sci* **21**, 3373 (2020).
34. Karthick Kannan, P., Shankar, P., Blackman, C. & Chung, C. Recent Advances in 2D Inorganic Nanomaterials for SERS Sensing. *Advanced Materials* **31**, 1803432 (2019).
35. Pohanka, M. Overview of Piezoelectric Biosensors, Immunosensors and DNA Sensors and Their Applications. *Materials* **11**, 448 (2018).
36. Kim, J. *et al.* 2D Materials for Skin-Mountable Electronic Devices. *Advanced Materials* **33**, 2005858 (2021).

Effect of Annealing temperature on the formation of crystalline Titanium dioxide nanotubes

Alex J Thachil[1], Aijo John K[1*]
[1]*Thin Film Research Lab, Department of Physics, Union Christian College, Aluva-683102*
*aijojohn1@gmail.com

Abstract. Vertically aligned titanium dioxide nanotubes are fabricated by anodization of titanium plates. The anodization is carried out with ammonium fluoride in ethylene glycol as the electrolyte. The surface morphology of the as-formed nanotubes was analyzed by using Scanning Electron Microscope. The as fabricated nanotubes are of amorphous form, it is then converted to crystalline nature by the process of Thermal Annealing. The effect of annealing temperature on the crystalline nature and type of polymorph present is also analysed.

Keywords: TiO_2 nanotubes,Thermal annealing.

1 Introduction

The wide band gap with suitable band edge positions, exceptional biocompatibility, unique ionic and electronic properties, etc., make titanium dioxide one of the most investigated metal oxides. The specific surface area of TiO_2 is significantly enhanced in the nanostructured forms such as, nanotubes, nanoparticles, nanorods, etc., which is crucial in determining its maximum overall performance in respective applications.

Fabrication and applications of TiO_2 nanotubes (TONT) are widely investigated due to their properties such as unique architecture, high surface-to-volume ratios, excellent electron percolation pathways and size dependent properties. These facts make TONT subject of considerable scientific interest as well as potential candidate for a number of practical applications [1]. Outstanding charge transport and carrier life time properties enable TONT for a variety of applications such as sensors [2], dye sensitized solar cells [3], water photoelectrolysis, photocatalytic reduction of carbon dioxide under sunlight [4], and supercapacitors [5]. In addition, nanotube arrays are used in

biomedical applications such as biosensors, molecular filtration and drug delivery.

TONT arrays are reported to be fabricated by a variety of methods such as hydrothermal processes [6], template method [7], sol–gel method [8], etc. However, the most remarkable properties are exhibited by TONTs fabricated by anodization of Titanium in fluoride-based baths [9], due to the possibility for precise tailoring of the morphological parameters.

Titanium dioxide (TiO_2) is a polymorphic compound used in various applications such as photocatalysis, dye sensitized solar cells, and biomedical devices due to its excellent properties where, Anatase, Rutile, and Brookite being its various polymorphs. In this report, we have fabricated titanium dioxide nanotubes by electrochemical anodization and then annealed the obtained amorphous nanotubes to form crystalline nanotubes under different temperature ranges to check the effect of annealing on crystallization.

2 Experimental

Anodization is a very easy and economical method to fabricate self-organized and uniform TiO_2 nanotubes. Uniform arrays of TONT are fabricated by anodization of titanium plates.

The titanium foils are polished to a smooth finish using silicon carbide papers of successively finer roughnesses and degreased by sonicating for 5 minutes in water. They are then dried in air and anodized immediately. The electrolyte for anodization is 0.5 wt% ammonium fluoride and 2 vol % H_2O in ethylene glycol. The electrolysis has been carried out using titanium plate as the anode and cathode. The solution is continuously stirred during the process. Samples are prepared at varying anodization durations. The anodization voltage (50 V) and the electrolyte composition (0.5 wt % NH_4F +2 vol %H_2O in ethylene glycol) are kept constant. The surface morphology has been analysed using Scanning Electron Microscope (SEM).

The amorphous titanium dioxide nanotubes are then thermally annealed for about two hours at different temperatures a) 150^0C b) 450^0C c) 750^0C to study its effect on the formation of crystalline Titanium dioxide nanotubes.

3 Results and Discussions

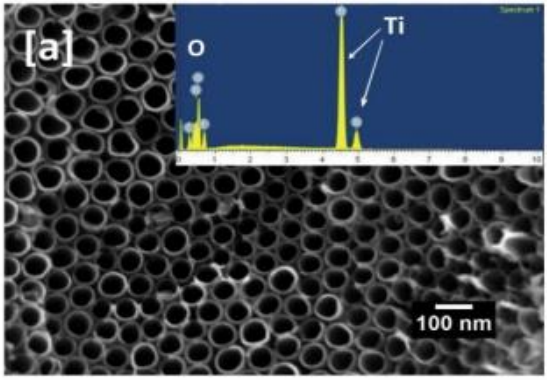

Fig. 1. SEM Image and EDAX (inset) of Titanium Dioxide nanotubes formed during electrochemical anodization

Field Effect Scanning Electron Microscopy (FESEM) is used to study the tubular structure of the TiO_2 nanotubes fabricated by electrochemical anodization in an organic electrolyte containing ethylene glycol and ammonium fluoride. The surface images of the nanotubes show the ordered nature of the TiO2 nanotubes (Figure 1).

The TiO_2 nanotubes formed by the electrochemical anodization method are amorphous in nature. These amorphous nanoporous materials lack mechanical and thermal stability. Reports indicate that electrical, optical and photocatalytic properties of the amorphous materials are also poor compared to that of the crystalline nanoporous materials which exhibit superior properties. Generally, the heat treatment at elevated temperatures is used for the amorphous to crystalline transition. This post deposition thermal annealing, resulting crystal structure, crystal phase and the degree of crystallinity have substantial effect on the electrochemical properties of TiO_2 nanotubes. The detailed XRD analysis shown in Figure 2 reveals the conversion of the amorphous nanotubes into anatase/rutile crystalline phases upon thermal annealing at different temperatures. All the samples are annealed for a duration of 2 hours. The conversion of the amorphous to anatase crystalline structure starts at $150^{O}C$. The percentage of the anatase phase is increased as the

annealing temperature is raised and the rutile phase begins to appear at 450^{O}C. Further annealing at 750^{O}C results in rutile nanotubes with small amounts of anatase crystals.

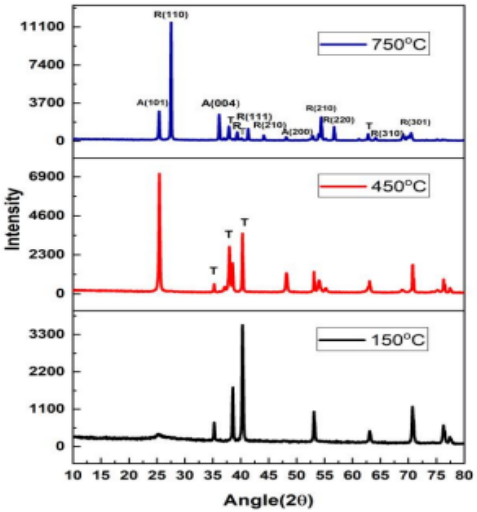

Fig. 2. XRD analysis of TiO_2 nanotubes annealed at various temperatures

Anatase planes are (101), (004), (200), and rutile planes are (110, (111), (210), (211), (220), (310) and (301). The major crystal orientation upto the 450^{O}C is anatase (101) and above 450^{0}C the preferential orientation changes in to rutile (110).

4 Conclusion

The XRD analysis of Annealed samples at lower temperatures reveals the initial signs of conversion of the amorphous titanium dioxide to crystalline form and at a temperature of 450^{0}C and above the TiO_2 nanotubes are well crystallized and the crystallization is predominantly in the anatase phase and at higher temperatures 750^{0}C rutile phase starts to appear and results in a mixture of both anatase and rutile phase. The SEM analysis shows the formation of well aligned Titanium dioxide nanotubes.

Acknowledgments

The First author acknowledges DST-SERB and Dr. Rachel Reena Philip for funding through a Project internship.

References

1. G. K. Mor, O. K. Varghese, M. Paulose, K. Shankar, C. A. Grimes, *Solar Energy Materials & Solar Cells* **90,** 2011–2075 (2006);
2. J. M. Macak, H. Tsuchiya, A. Ghicov, K. Yasuda, R. Hahn, S. Bauer, P. Schmuki; *Current Opinion in Solid State and Materials Science* **11,** 3–18 (2007).
3. O. K. Varghese, D. Gong, M. Paulose, K. G Ong, C. A. Grimes, *Sens Actuators B* **93**, 338-344 (2003).
4. K. Shankar, G. K. Mor, M. Paulose, O. K. Varghese, C. A. Grimes, *J Non-Cryst Solids* **354**, 2767-2771 (2008)
5. O. K. Varghese, M. Paulose, T. J. LaTempa, C. A. Grimes, *Nano Letters* **9**, 731-737 (2009).
6. M. Salari, S. H. Aboutalebi, K. Konstantinov, H. K. Liu, *Phys. Chem. Chem. Phys. **13**, 5038-5041 (2011).*
7. T. Kasuga, M. Hiramatsu, A. Hoson, T. Sekino, K. Niihara, *Langmuir* **14,** 3160-3163 (1998).
8. P. Hoyer, *Langmuir* **12,** 1411-1413 (1996).
9. J. H. Jung, H. Kobayashi, K. J. C. V. Bommel, S. Shinkai, T. Shimizu, *Chem. Mater.* **14**, 1445-1447 (2002).

Physics Department of Union Christian College, established in 1926, has scaled new heights in the last decade. It has now five full-fledged research labs in Thin Films, Nanomaterials, Optics, Optoelectronics and Theoretical Research which have national and international research collaborations. The development has been made possible through the support of various research funding agencies like DST, DAE, UGC, BRNS and KSCSTE.

The Department of Physics organized a two-day workshop *WMCT-23* as part of the SSR policy in a DST project (Ref No: CRG/2020/000448) sanctioned by Govt. of India. This workshop on material characterization techniques provided a broad overview of the experimental and theoretical techniques which are generally used for characterizing materials through introductory lectures with emphasis on instrumentation and data analysis. This book is proceedings of the research papers presented at the workshop.

9 788196 045715